

Lehrstuhl für Leichtbau  
Technische Universität München

# **Modeling of the Structure-Optics-Interaction in Large Astronomical Telescopes**

Michael Müller

Vollständiger Abdruck der von der Fakultät für Maschinenwesen der Technischen Universität München zur Erlangung des akademischen Grades eines

**Doktor-Ingenieurs (Dr.-Ing.)**

genehmigten Dissertation.

Vorsitzender: Univ.-Prof. Dr.-Ing. J. Heinzl

Prüfer der Dissertation: 1. Univ.-Prof. Dr.-Ing. Horst Baier

2. Univ.-Prof. Dr.-Ing. habil. H. Ulbrich

Die Dissertation wurde am 05.10.2004 bei der Technischen Universität München eingereicht und durch die Fakultät für Maschinenwesen am 17.02.2005 angenommen.



# Abstract

## Structure-Optics-Interaction in Large Astronomical Telescopes

Astronomical telescopes evolve to larger and larger systems to increase optical sensitivity and spatial resolution, which are related to the light collecting area and the aperture diameter respectively. However, for ground-based telescopes the resolution is limited to a value achievable with an aperture diameter of 10-20cm due to the atmospheric turbulence interfering the incoming wavefront.

To exceed this seeing limits adaptive optics is urgently required which actively compensates for wavefront errors. Moreover disturbance sources like wind load and seismic excitation cause time-dependent deformations of the telescope structure. A passive structure of this size can no more provide tolerances of the order of  $\lambda/28$ <sup>1</sup> required for optical telescopes with diffraction limited imaging. This accuracy can only be achieved using active control of mirror position and shape. Moreover the large aperture mirrors cannot be manufactured as single solid elements. Hence a high segmentation will be used to compose the primary mirrors of future large telescopes requiring an actively controlled alignment system.

Consequently control is essential in modern telescopes and the structural mechanics, the optics and the control are strongly interacting. For design and development an integrated model representing the major telescope components is essential since this allows to study the complete system and cross coupling effects between components.

The presented work deals with the generation of a dynamic structural model appropriate to be incorporated into an integrated telescope model. This becomes a key-issue as the larger telescope dimensions require stricter relative tolerances and the structure needs to be a sophisticated lightweight design to achieve high natural frequencies. It is a difficult task to accurately represent the dynamics between the large number of inputs and outputs while keeping the system size small to limit the computational effort of a simulation.

For integrated modeling an approach is developed focusing on modularity and flexibility to easily investigate different parameters, configurations and components. A single configuration file is used to compute optical models and dynamically create the

---

<sup>1</sup>The wavefront rms resulting from a deflected mirror shape is twice the surface rms. Thus this condition corresponds to an maximum wavefront rms of  $\lambda/14$ .

complete system. Modeling the European Southern Observatory's Very Large Telescope Interferometer (VLTI) this approach is implemented and the model is applied to exemplary simulations.

# Contents

<b>Nomenclature</b>	<b>vii</b>
<b>1 Introduction and Objectives</b>	<b>1</b>
1.1 Integrated structure-optics-control modeling — state-of-the-art . . .	2
1.2 Objective of this work . . . . .	7
1.3 Outline of the thesis . . . . .	10
<b>2 Major components in telescope systems for integrated modeling</b>	<b>13</b>
2.1 Outline . . . . .	13
2.2 Optics in telescopes and interferometers . . . . .	14
2.2.1 Wavefront errors and Zernike polynomials . . . . .	14
2.2.2 Diffraction effects and image quality . . . . .	17
2.2.3 Stellar interferometers . . . . .	19
2.2.4 Comparison and summary of wavefront errors . . . . .	22
2.3 Mechanical structure of telescopes . . . . .	23
2.4 Control loops . . . . .	25
2.5 Disturbances . . . . .	26
2.5.1 Quasi-static and dynamic disturbances . . . . .	26
2.5.2 Vibration sources for ground based telescopes . . . . .	26
Wind load . . . . .	27
Seismic load . . . . .	30
2.5.3 Turbulence . . . . .	31
Atmospheric Turbulence . . . . .	31
Internal turbulence . . . . .	34
2.5.4 Noise . . . . .	35
<b>3 Model reduction for dynamic structural models</b>	<b>37</b>
3.1 General mathematical description of telescope structures . . . . .	37
3.1.1 Finite element modeling . . . . .	38
3.1.2 Handling disturbance inputs from wind and ground . . . . .	41
3.1.3 Including actuators into a model . . . . .	44
3.1.4 Best-fit outputs for rigid body motions of the mirrors . . . . .	44
3.1.5 Elastic mirror deformation in terms of Zernike modes . . . . .	48

3.2	Criteria for model reduction . . . . .	50
3.2.1	Criteria for general transfer functions . . . . .	50
3.2.2	Criteria for transfer functions of mechanical structures . . . . .	54
3.2.3	Gramians . . . . .	56
3.3	Balanced model reduction . . . . .	58
3.4	Other reduction methods . . . . .	61
3.5	Examples for reduced models created with the Structural Modeling Interface Toolbox (SMI) . . . . .	63
3.5.1	Description of the toolbox . . . . .	63
3.5.2	Examples for reduced models . . . . .	67
	Dynamic model of the Very Large Telescope (VLT) . . . . .	67
	Dynamic model of the Overwhelmingly Large Telescope (OWL) . . . . .	70
<b>4</b>	<b>Solutions for selected issues in telescope structural mechanics</b>	<b>75</b>
4.1	Scattering in material parameters . . . . .	75
4.1.1	Analysis setup . . . . .	77
4.1.2	Creation of random distributions . . . . .	78
4.1.3	Simulation results for the load cases . . . . .	80
	Nominal reflector and worst cases . . . . .	80
	Frequency curves for the statistically varying $V_f$ . . . . .	81
4.1.4	Conclusion . . . . .	83
4.2	Dynamic effects of ground and telescope foundation . . . . .	84
4.2.1	FE-model of a telescope structure including soil . . . . .	86
4.2.2	Results of the modal analysis and harmonic response . . . . .	87
4.2.3	Conclusion . . . . .	95
<b>5</b>	<b>Very Large Telescope Interferometer (VLTI) Integrated Model</b>	<b>97</b>
5.1	Basics features of the VLTI Integrated Model . . . . .	97
5.2	BeamWarrior — The optical modeling tool . . . . .	98
5.3	Architecture and design of the VLTI-Integrated Model . . . . .	101
5.3.1	Computing the dynamic interferometer response . . . . .	101
5.3.2	Model architecture . . . . .	102
	Control loops . . . . .	103
	Modeling of the disturbances . . . . .	104
	Representation of the signals . . . . .	105
5.3.3	Simplified beam combiner models . . . . .	107
5.3.4	The Ruilier approximation . . . . .	107
5.4	Simulation results . . . . .	110
5.4.1	Test of plausibility for a sensitivity matrix . . . . .	111
5.4.2	Contribution of different components to the error due to wind load . . . . .	111
5.4.3	Contribution of different disturbances to the error . . . . .	113
5.4.4	Disturbance rejection of the control loops . . . . .	115

---

5.4.5	Accuracy evaluation of the Ruilier approximation . . . . .	116
<b>6</b>	<b>Conclusion and outlook</b>	<b>123</b>
6.1	Conclusion for this work . . . . .	123
6.2	Outlook towards modeling Extremely Large Telescopes . . . . .	125
	<b>Bibliography</b>	<b>127</b>
	<b>List of figures</b>	<b>131</b>
	<b>List of tables</b>	<b>135</b>
	<b>Appendix</b>	<b>136</b>
A	Relationship between time-series, PSDs and RMS-values . . . . .	136
B	Zernike polynomials used within BeamWarrior . . . . .	138
C	Gramians as the solution of the Lyapunov equation and meaning . . .	139
D	Visibility function and brightness distribution . . . . .	141
E	Rigid body motions . . . . .	141





# Nomenclature

Abbreviation		Meaning
AT		Auxiliary Telescope of VLTI
AURA		Association of Universities for Research in Astronomy
Caltech		California Institute of Technology
CFD		Computational Fluid Dynamics
CFRP		Carbon fibre reinforced plastic
CTE	$1/K$	Thermal expansion coefficient
DDE		Dynamic Data Exchange
DOCS		Disturbance, Optics, Control and Structure (toolbox of MIT)
DOF		Degree of freedom
ELTs		Extremely Large Telescopes
ESO		European Southern Observatory
FE		Finite Elements
FEA		Finite Elements Analysis
FEM		Finite Elements Method
FINCH		Flexible Interferometer Characterization
FWHM		Field Width Half Maximum
HIA		Canadian Herzberg Institute of Astrophysics
HSV		Hankel Singular Value
IMOS		Integrated Modeling of Optical Systems (toolbox of JPL)
ITM		Integrated Telescope Model (toolbox of Ball Aerospace)

Abbreviation		Meaning
JPL		Jet Propulsion Laboratory, Pasadena, USA
JWST		James Webb Space Telescope (former NGST)
LOM		linear optical model
M1,M2,...		Mirrors of a telescope
MIT		Massachusetts Institute of Technology
NEXUS		Normal Incidence Extreme Ultraviolet Spectrograph
NGST		Next Generation Space Telescope (now JWST)
OPD	$m$	Optical path difference
OPL	$m$	Optical path length
OWL		Overwhelmingly Large Telescope (of ESO)
PSD	$\frac{[\text{amplitude}^2]}{\text{Hz}}$	Power spectral density
rms		Root mean square
SID		Siderostat of VLTI
SIM		Space Interferometry Mission
SVD		Singular Value Decomposition
TMT		Thirty Meter Telescope
TPF		Terrestrial Planet Finder
TR		Top ring of the VLT
TRP		Technology Research Programme (of ESA)
TU		Tube of the VLT
UT		Unit Telescope of VLTI
VCM		Variable curvature mirror
VLT		Very Large Telescope
VLTI		Very Large Telescope Interferometer (of ESO)
VLOT		Very Large Optical Telescope (of HIA)

---

Variable	Meaning
$A$	Amplitude of electrical field
$A$	Area

Variable		Meaning
$A$		System matrix of state-space model
${}^M A_{MK}$		Transformation matrix to transform a vector from system K into system M
$B$		Baseline of an interferometer
$B$		Input matrix of state-space model
$C_n, C_T, C_v$		Constant for describing the turbulence
$C$		Output matrix of state-space system
$D$		Feedthrough matrix of state-space system
$D$	$m$	Aperture diameter
$D$		Damping matrix
$D_v$		Structure function for characterizing turbulence
$E$	$N/m^2$	Youngs modulus
$E$		Mapping matrix
$F$	$N$	Force
$F_\lambda$		Power per area
$G(\omega)$		Transfer function
$H_{ij}$		Transfer function matrix
$I$		Identity matrix
$I$		Intensity of an electrical field
$I$		Turbulence intensity
$K$	$N/m$	Stiffness, Stiffness matrix
$L$	$m$	Characteristic length
$M$		Mass matrix
$M_{coh}$		Amplitude modulation function
$P$		Point
$P_B$		Matrix to generate inputs due to base excitation
$P_L$		Matrix to generate inputs due to loading forces
$P_S, P_{S_x}, P_{S_z}$		Matrix to generate outputs (displacement/velocity) from generalized displacements

Variable		Meaning
$\tilde{R}$		Matrix building the cross product
$Re$	–	Reynolds number
$S$		Weighting vector
$S(f)$		Power spectral density
$T$	$K$	Temperature
$T$		Transformation matrix
$U$	$m/s$	Velocity
$V$		Complex visibility function
$V$	$m^3$	Volume
$W$	$m$	Wavefront error
$W_C$		Controllability Gramians
$W_O$		Observability Gramians
$W_u, W_y$		Weighting matrices
$c$	$m/s$	Velocity of light in vacuum
$c_D$	–	Drag coefficient
$c_P$	–	Pressure coefficient
$d$		Distance
$f$	$1/s$	Frequency
$f$	$m$	Focal length
$f$		Vector of generalized forces
$g$	$m/s^2$	Acceleration of earth
$g_i$		Weighting factor
$k$		Wavenumber = $2\pi/\lambda$
$i, j, k, l, m, n$	–	Indices
$m$	$kg$	Mass
$n$	–	Refraction index
$q$	$N/m^2$	Dynamic pressure
$q$		Vector of modal DOFs

Variable		Meaning
$r$	$m$	Radius in polar coordinates
$r_0$		Fried parameter
$u, v, x, y, z$		Cartesian coordinates
$x$		Vector of generalized displacements
$\mathbf{r}$		Spatial coordinate
$\mathbf{k}$		Wave vector (including the direction of the light ray)

## Greeks

$\alpha, \beta$		Angular coordinates
$\gamma$		Eigenvalue
$\zeta$	$rad$	Angle
$\zeta$	$m$	Zernike coefficient
$\zeta, \zeta_i$	–	Modal damping (of mode $i$ )
$\theta$	$rad$	Angle
$\lambda$	$m$	(Optical) wavelength
$\Delta\lambda$	$m$	Bandwidth of a spectral band
$\Lambda_{coh}$		Coherence wavelength = $\lambda_0^2/\Delta\lambda$
$\nu$	$1/s$	Frequency
$\rho$	$kg/m^3$	Density
$\sigma_i$		Hankel singular values
$\tau_0$		Coherence time ( $\tau_0 = r_0/U$ )
$\phi$	$rad$	Angle
$\phi$	–	Eigenvector, matrix of eigenvectors (respectively mode shapes)
$\chi_a^2$	–	Aerodynamic attenuation function
$\psi$		Electric field
$\psi$		Zernike polynomial
$\omega$	$rad/s$	Circular frequency
$\omega_i$	$rad/s$	Eigenfrequencies



# 1 Introduction and Objectives

Since the beginning of modern astronomy 400 year ago with G. Galilei and J. Kepler, astronomical research is having a large impact on our knowledge of physics as well as on the wide and deep understanding of the universe. The demand of observing fainter objects has led to larger aperture diameters to increase the light-collecting area. An advancement in optical sensitivity has not only been achieved by larger telescopes, but also by better observatory sites like in Hawaii and Chile, improving the environmental conditions inside the dome, using new materials, the development of enhanced instruments and applying a superior pointing and tracking.

Alongside sensitivity, angular resolution is most important for telescope performance. Due to the diffraction theory of electromagnetic waves, the limit for angular resolution of a telescope is proportional to the ratio of wavelength versus aperture diameter. However, for ground-based optical telescopes resolution is limited by atmospheric turbulence. Hence moving to better sites on ground or towards space yielded enhancements. In the recent years active and adaptive optics initiated a new generation of optical ground-based telescopes with higher angular resolution. The mirrors of active optics are not simply fixed to the mirror support structure, but mounted on actuators. These allow to reduce significantly quasi-static aberrations of the mirror positions and shapes, which are e.g. induced by gravity effects and thermal expansions. In an adaptive optical system, the dynamically varying wavefront error is measured by a wavefront sensor and fed back with a controller to a deformable mirror to actively compensate inter alia for the atmospheric turbulence.

Several astronomical telescopes for optical or infrared wavelengths with apertures of up to 10m are in science operation or in their commissioning phase at the moment. For better angular resolution stellar interferometers were built. In stellar interferometry, the light of two or more spatially separated telescopes ("subapertures") is combined in order to synthesize the resolution of a single large telescope with an aperture diameter equal to the distance of the subapertures. Dependent on the actual phase difference between the light rays, which is a function of the optical path length, the rays superpose constructively or destructively resulting in high or low light intensity. An important requirement for operating an interferometer is thus to keep defined optical path lengths in both interferometer arms by actively compensating for disturbances.

The increased telescope performance, new astronomical observations and novel scientific results have demonstrated the potential of active and adaptive optics in these

so called VLTs (Very Large Telescopes). Still there is a long list of observation requests like the evolution of galaxies, large-scale structures, formation of stars or the evolution of external planets, which need both a higher spatial resolution and a more powerful light collection.

In order to observe fainter objects and to achieve higher resolution, first studies have started in the United States and Europe for a new class of ELTs (Extremely Large Telescopes) with aperture diameters from 30 to 100m. The complexity and interdependence of the telescope subsystems will rise significantly in these ELTs. Hence new design and simulation approaches will be strongly demanded to successfully realize such a project. ([1, p. 1-4], [2], [3], [4])

## **1.1 Integrated structure-optics-control modeling — state-of-the-art**

Practically all existing ground-based telescopes have been designed by a closed collaboration of specialists within their field as the design of a telescope relies on a variety of different scientific and engineering disciplines.

In the classical approach towards a first telescope design analytical formulas and empirical expressions are used to estimate the telescope performance. Then in the design phase special tools are applied, established in the respective discipline (e.g. finite element software for the structural mechanics, optical design and optimization software, control design and simulation software). To evaluate the telescope design a mathematical model of the physical aspects and characteristics of the telescopes including the optical components, the dynamics of the telescope structure, the sensors and actuators is built, modeling also the different disturbance sources. Applying control-system layout techniques a suitable controller is designed and its parameters are adjusted to optimize the telescope performance.

As Bely explains in [1, p. 62-75, 253-254] this procedure cannot directly be applied to the design of ELTs, since they imply a much stronger inter-relation between different disciplines and a complex system of feedback loops to control the shape and the position of all optical components. A conventional telescope, which is mainly a passive structure with nearly rigid optical mirrors, is described in a good approximation by a mathematical model consisting of analytical formulas and semi-empirical assessments. However, for ELTs with highly segmented, individually steered mirrors and (relatively) large deflections due to wind load, this approach is no more sufficient, as it does not show the interdependence of the different components and allows not to fully evaluate the system. Therefore, the accurate simulation with an integrated model is essential for optical performance estimation and design validation of a future telescope.



An integrated model yields benefits in all design phases of a telescope project. In the *planning phase* it allows to demonstrate feasibility in detail and to evaluate alternatives. In an *early design phase* requirements can be established and validated. This includes the critical features and disturbances, structure-control and loop-to-loop interactions, cross coupling effects and sensitivities. In order to provide accurate component data in the simulation, for critical components demonstrators are built and their relevant parameters are identified. A gradual refinement of the subsystems in the integrated model enables the detailed analysis of the telescope and an accurate performance prediction in the *detailed design phase*. In the *construction phase* the model quality can be further improved due to component tests and data of on-site measurements. In addition to this such a model can also be useful in the *operational phase* for the preparation of astronomical observations or to select optimum observation parameters. It helps to calibrate the telescope and allows to correct for systematic errors in the observation data. ([5, 6])

In the last ten years several institutions have started to develop tools for integrated modeling. These tools were especially applied to space telescopes, since environmental conditions cannot be fully provided in a ground-based test (e.g. absence of gravity and atmosphere). The development, adjustment and application to ground-based ELTs has just started some years ago and at current almost all large telescope or interferometer projects involve integrated modeling.

Different concepts for integrated modeling were developed. In the “bucket-brigade approach” the specialists within their fields of mechanics, optics and control build their mostly independent models specialized for the individual requirements. A model of the complete system is composed of this elements requiring mostly manually adjustments of the individual systems. Changes in components require therefore a large effort to be consistently included.

In contrast to this “bucket-brigade approach” IMOS was developed by JPL (Jet Propulsion Laboratory, Pasadena, USA) as one of the first integrated modeling tools trying to use only one data-base by integrating all different disciplines within one software. IMOS is a Matlab-based toolbox and was applied to several projects like the Hubble Space Telescope, SIM (Space Interferometry Mission) or the NGST (formerly Next Generation Space Telescope, now James Webb Space Telescope (JWST)). ([7, 6, 8, 9, 10])

IMOS includes Matlab-written FE modeling with element types similar to NASTRAN, which allow a static and dynamic structural analysis with mode superposition as well as thermal computations. The optical modeling is either done directly within IMOS or with interfaces to the JPL-written optical software MACOS (Modeling and Analysis of Controlled Optical Systems). In its initial version IMOS was limited in the number of degrees of freedoms for the finite element models. Therefore the concept of integrating all into one tool was given up and now also NASTRAN is used for FE-modeling.

In the early 90's Ball Aerospace, (Boulder, Colorado, USA) launched the Integrated Telescope Model (ITM) program, which was applied to the Very Large Telescope (VLT) of ESO, NGST and TPF (Terrestrial Planet Finder). Most of the model is built within Simulink and only modal data are imported from a finite element analysis. The core of the simulation environment is an optical toolbox realized in Simulink. Both, physical optics with diffraction propagators and geometrical optics with ray tracing or sensitivity matrices are covered. Building the model within Matlab/Simulink tries to make the tool flexible and adaptable. However, the experience of the VLT Integrated Model showed limitations in using the model, since the model proved not to be easy-to-use and was very awkward to handle. ([11])

Unlike trying to use one universal software tool for modeling all different disciplines, e.g. the EURO50 team of the University of Lund/Sweden is developing an integrated model using different packages. The model is Matlab-based using modal results from a finite element analysis (FEA) in ANSYS and optical ray tracing is simulated within Matlab. ([2])

Besides the kind of tools applied, also the degree of coupling this tools is different. An approach using similar tools as for the EURO50 but with a higher degree of coupling and being more comprehensive is developed at present at the Canadian Herzberg Institute of Astrophysics (HIA) for the Very Large Optical Telescope (VLOT), a 20m optical telescope. For ray tracing and the generation of linear optical models (LOMs) the commercially available software ZEMAX is used, which is coupled with Matlab using DDE (Dynamic Data Exchange) technique as part of the Microsoft Windows operating system. The integrated model includes a fully parametric ANSYS model for the structural mechanics and interfaces to PowerFlow Computational Fluid Dynamics (CFD) software to compute the dynamic wind load. 1500 modes are remotely read from ANSYS to build a state-space model with balanced model reduction within Matlab. The complete model incorporates 1800 outputs and 1500 inputs due to the large number of control loops to steer the segments according to the signals of the edge sensors. Different types of disturbances are included like wind, gravity, seismic load, thermal effects, atmospheric turbulence, sensor noise and actuator errors. Only one model base for FE modeling, optics and control is used to allow consistent changes of parameters. Constraining the integrated model to the Microsoft Windows operating system due to DDE is a major drawback, as the largest and most powerful computers usually run a UNIX-type operating system. Using commercially available software restricts the available outputs and can also imply a limitation in flexibility. ([12])

In Northern America the activities of the HIA have merged with the California Institute of Technology (Caltech), and AURA (Association of Universities for Research in Astronomy), which is a consortium of universities and other non-profit organizations, that operates astronomical observatories like, for example, the Gemini Observatories in Hawaii and in Chile. They develop an Integrated Model for the Thirty Meter Telescope (TMT). The main objective of this cooperation is to incorporate and further

develop existing integrated modeling tools. An object-oriented database for optical and structural models will be built with classes for structure, active optics, beams, sensors, etc. The integrated model will be Matlab-based with interfaces to different external software tools. In the initialization phase results from FEA, CFD, a thermal analysis and an atmospheric model will be computed according to the configuration. This data will then be used for the simulation within Matlab/Simulink.([13, 14])

Another very comprehensive tool is DOCS (Disturbance, Optics, Controls and Structures), which is developed at the Space Systems Laboratory at MIT (Massachusetts Institute of Technology) and which was applied to SIM, NGST, NEXUS (Normal Incidence Extreme Ultraviolet Spectrograph), and TPF. DOCS is a Matlab-based framework with interfaces to IMOS (for integrated modeling), NASTRAN (FEM), thermal analysis software and optimization tools. Within DOCS the integrated modeling capabilities of IMOS are significantly extended including optimization, uncertainty analysis, robustness of systems, model reduction, error budgeting and comparison of measurement and simulation. The large effort of developing tools is avoided in DOCS by using commercial available software and providing only interfaces between the different tools. Using Matlab keeps the framework flexible and further expandable.([15, 16, 17, 18])

Due to a lack of comprehensive tools for optical modeling for usage in an integrated model, BeamWarrior was developed in a joint activity by ESO and EADS Astrium, Friedrichshafen, Germany. The BeamWarrior Kernel is a library of platform-independent ANSI C functions for optical modeling which can be accessed either by a custom C application or via the BeamWarrior Optical Modeling Tool. The latter is a general-purpose application designed for flexible generation of linear optical models (i.e. sensitivity matrices). BeamWarrior incorporates geometrical- and wave-optics. For wave-optical methods different algorithms are implemented including a numerical approximation of the Rayleigh-Sommerfeld integral and the powerful Gaussian beam decomposition technique. Besides the creation of dynamic optical models BeamWarrior can also be employed for a large variety of static optical analysis tasks, like a diffraction or polarization analysis as well as for tolerancing problems.

BeamWarrior was applied for optical modeling of the VLT of ESO and an integrated model of the Very Large Telescope Interferometer (VLTI), which is part of this thesis (see chapter 5). In the framework of an ESA Technology Research Programme (TRP), BeamWarrior is used to develop the integrated model FINCH (Flexible Interferometer Characterization) of the spaceborne nulling interferometry mission Darwin. Within the FINCH project also extended astronomical sources are modeled and broadband optics.

Major advantages of BeamWarrior are the powerful and efficient algorithms, which cover most optical phenomena relevant for telescopes and interferometers. Another benefit for ESO/Astrium is the availability of the source code to adjust the tools if

necessary to desired output formats or also to expand the capabilities. The drawback is the effort in developing and validating the self-written software.

Regarding the current integrated modeling approaches, Matlab is obviously always used as the *integration environment* and *control software*, as this is the most comprehensive dynamic simulation package. The levels of integration and of detail represented are different and imply compromises between development effort, flexibility, ease-of-use and technical capability. An example for low degree of integration is the integrated model of the EURO50, whereas the approach for the TMT uses for nearly all kinds of disturbances only one data base.

For a *structural model* commercially available FEA software tools are commonly used to compute modal results. The reasons for this are, on one hand the sophisticated and powerful finite element software packages with preprocessors, which allow to generate models of complex telescope structures, and effective solvers, that are specifically designed for structural mechanics problems. On the other hand, the relevant input from the structure to the optics is the displacement data for the different components. Since the displacements of the individual degrees of freedom (DOFs) are the standard result in an FEA, it is only necessary to supply appropriate matrices, that convert the results for the DOFs into the desired displacements of the optical components and hence, the effort for adjusting the FEA outputs is relatively small. In contrast to the structural models the requirements for the optical simulations are very different.

*Optics tools* range from ray-tracing (IMOS developed by JPL) over commercially available optical design software (ZEMAX) to highly flexible and powerful code specifically designed for usage in an integrated modeling environment (BeamWarrior and MACOS, ray tracing and wave-optics). For optics modeling no dynamics is inside the governing equations, but optics is in general highly nonlinear and the description much dependent on the effects, which are to be investigated, and the model, which is suitable to describe the effects. Especially the ELTs incorporate a large number of segments for the primary as well as (often) for the secondary mirror and consequently a lot of edges and gaps exist which all cause diffraction effects. To provide consistent models for the simulations using one common model for the optics is an advantage, which is at current only covered by BeamWarrior.

Designing an integrated model, the main objectives are first flexibility to adjust the model to different configurations and designs as well as to be able to increase gradually the level of detail. A modular approach is therefore important, which allows on the one hand to keep interfaces while improving or exchanging components and on the other hand to easily include e.g. additional control loops. Secondly the model should deliver all desired results and relevant outputs. This requires powerful tools, which are e.g. for FE-modeling not limited in model size as IMOS and for optical modeling able to reflect the relevant effects, while giving access to desired results. Having these models only in the dedicated software packets is not sufficient, but interfaces and tools must be provided to build accurate structural models of reduced size or

linear optical models, which can be used for an integrated model. These required routines are usually not included in e.g. the FE-software, but must be developed. In addition to that, the simulation must produce reliable results and therefore validation of the tools and verification of the results is essential and should be already done on component level. Hence, using as many proven tools as possible is an advantage. However, where adequate tools are not available, interfaces and software components have to be developed to keep the model flexible and powerful.

## 1.2 Objective of this work

Integrated modeling is essential in the design and development of future large telescope systems. The objectives of this work are first of all to develop a concept to provide a suitable model of the telescope structure to be used in an integrated model. Secondly an efficient approach for integrated modeling of astronomical telescopes will be developed and its application will be tested.

The generation of an accurate and easy-to-handle structural model for the time-dependent simulation of its coupling with optics and control has become especially important since the telescopes are increasing in size. The eigenfrequencies are hence shifted to lower values and therefore the first natural modes reach the relevant frequency range for control loops. Moreover the amplitude of the wind turbulence is increasing with decreasing frequency and thus, wind effects become more serious. While scaling the telescopes to larger sizes, the absolute tolerances are kept on the same levels due to the same permitted wavefront errors, which causes stricter relative tolerances. Telescope dynamics can in general be treated linearly, which simplifies the mathematical description dramatically. A main reason for this is the construction, which avoids microslip and friction, e.g. by applying hydrostatic bearings. However, nonlinear effects can occur e.g. if friction drives are used.

The telescope structures become not only larger, but also much more complex. Thus large FE models are necessary to describe the dynamics accurately and reducing the degrees of freedom becomes more important. Examples are the already built VLT and the concept the Overwhelmingly Large Telescope (OWL), both of ESO. One FE model of the VLT consists of 9485 elements and 38268 DOFs with beam elements and shell elements for the mirror M1. The OWL model was built of simple pipes and point masses only, but had 131076 elements and 213510 DOFs (see figure 1.1 and table 1.1).

Due to mirror segmentation and the possibility to use active optics the number of control loops comprised in telescope systems increases as well as the number of sensors and actuators. Since a dynamic model of the telescope structure must consist of a much larger number of inputs and outputs, the model reduction becomes more difficult. E.g. in the VLT the primary mirror is supported by 150 hydraulic actua-

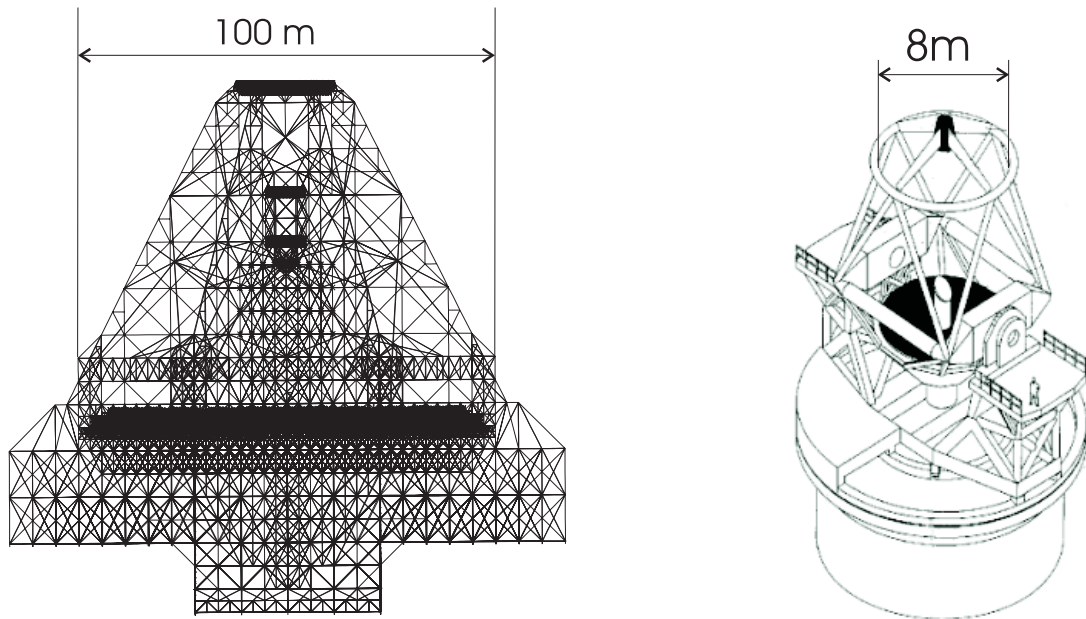


Figure 1.1: Comparison of the telescope structure of OWL and of the VLT

tors, whereas the OWL primary is planned with more than 3250 segments having 3 actuators each.

In some cases, the extreme size of the ELTs requires different concepts. An example are the altitude and azimuth drive systems proposed for the OWL. Instead of hydrostatic bearings as used for the VLT a system of some hundreds of bogies on rails provide the azimuth and altitude rotations required for pointing and tracking. Such a bogie-drive system involves the risk of stick-slip effects due to the velocity dependence of the friction and care must especially be taken with respect to the design of robust controllers. Both the design and the verification of the controller require appropriate structural models to represent the interaction of the friction, the driver forces and the dynamics of the telescope. A large number of inputs and outputs is necessary as the effective driving force of each active bogie depends not only on the control signal, but e.g. also (non-linearly) on the bogie velocity, the normal force on the wheels, the history etc. A design model for a certain control task must not exceed e.g. 15 states, since the model size has a direct influence on the controller size in a robust design. However, a (different) validation model needs a high accuracy to prove stability and performance.

Many different model reduction technics were developed and implemented, but the common routines provided, e.g., within Matlab do not consider the characteristic format of dynamic state-space models of mechanical structures. Moreover they were implemented for systems of medium size (about 100 states), but not for large systems of some thousand states. Besides long computation time the provided routines sometimes do not converge. This work discusses different criteria and techniques for

Table 1.1: Comparison: VLT and OWL

	VLT	OWL
Primary mirror M1	Ø 8.2 m meniscus with 150 actuators	Ø 100 m 3050 hexagonal segments with 3 actuators and 6 sensors each
Secondary mirror M2	monolithic 2 tip/tilt actuators	200 hexagonal segments with 3 actuators each
altitude and azimuth drive	hydrostatic bearings torque motors	2 altitude rails with 150 bogies several tracks on three levels with 250 bogies

model reduction and considers especially the applicability to state-space models of mechanical structures.

Two special aspects for modeling telescope structures are treated in more detail: considering scattering material parameters in a simulation and including the interaction between soil and telescope structure for modeling the dynamics of the telescope structure.

For integrated modeling within Matlab/Simulink a concept is developed for the VLTI, but can similarly be applied to other telescope systems. One major characteristic is the modular approach aiming on maximum flexibility and allowing strongly varying configurations. For the VLTI three different types of telescopes with completely different structures and optical descriptions can be used, and between two and eight telescopes are used simultaneously. Therefore the model is based on a single configuration file and creates the complete systems applying individual modules covering the miscellaneous telescopes, diverse control loops with exchangeable types and parameters of controllers and, of course, the different environmental conditions being investigated.

To provide broad applicability BeamWarrior is used for the modeling of the optical subsystems. BeamWarrior yields consistence of the optical models using only one optical description for the computation of static electric fields in the interferometer's exit pupils and the generation of linear optical models (LOMs). Moreover both geometrical optics can be simulated performing ray tracing and also physical optics is covered, which becomes even more important for ELTs due to the high degree of segmentation and consequently the large numbers of edges and gaps causing interference effects.

The integrated model allows a precise modeling of the physical effects in optics since , e.g., for polychromatic effects a spectral band is split into an user-defined number of sub-bands. LOMs for sensors and actuators can be generated in an arbitrary location

in the optical path. Furthermore a variety of optical results is possible, like the Point Spread Function (PSF) in the image plane or the wavefront error expressed in Zernike polynomials in the exit pupil, but also the full electric field on a pixel grid in the exit pupil of an interferometer arm with amplitude and phase.

A strong coupling between the ANSYS FE-model and the integrated model was assessed to be inconvenient as this restricts significantly the flexibility of the structural model. To allow a structural modification and optimization dynamic models are condensed only for certain reference configurations using the Structural Modeling Interface toolbox (SMI), which was developed within the scope of this thesis. The supporting routines provide an easy definition of inputs and outputs, and an allow to control model quality interactively at least for the most important transfer functions. Using only defined telescope configurations for the structure seems to be a major constraint, but all possible configurations and parameter combinations can never be fully investigated and evaluated and therefore it is always an engineering task to identify the most critical and characteristic configurations for a detailed study. The benefit is keeping the system reasonable simple and flexible.

An additional feature in the integrated model of the VLTI is the possibility to include instruments performing an interferometric beam combination. Two different beam combination algorithms are implemented — one which is very exact and the second one which is an approximation reducing the the computational effort significantly. This fast algorithm provides the possibility to include extended sources and polychromatic light into a simplified beam combiner model.

### 1.3 Outline of the thesis

To understand the coupling and inter-connections between the different disciplines and subsystems within an astronomical telescope a short overview over major components is given in chapter 2. Fundamental principles for describing the telescope optics are explained focusing on the effects of disturbances onto image quality. After characterizing the requirements and concepts for telescope structures and control loops, the environmental disturbances for ground-based telescopes are explained. Besides the physical effects possibilities of including this disturbances into an integrated model are shown.

Chapter 3 deals with a core topic of this thesis, the generation of an appropriate dynamic model of the telescope structure for use in an integrated modeling environment. A standardized state-space format is given including a general descriptions of inputs and outputs relevant for a telescope. A formulation of the required outputs especially for LOMs is given, which are the rigid body motions and elastic deformations of the mirrors in terms of Zernike mode shapes or other polynomials. Different criteria for evaluating the quality of a reduced model are discussed. The balanced



model reduction techniques are explained to be most appropriate allowing especially for state-space models of mechanical structures a fast computation of the approximated Gramians. In comparison to a balanced condensation the main characteristics of other methods are shortly described. To complete this chapter examples of applying model reduction technics to telescope structures are shown, applying the Structural Modeling Interface toolbox, which was developed within the scope of this thesis.

Two special aspects in modeling telescope structures are addressed in chapter 4. This is firstly scattering material parameters, a problem which is analyzed considering as example the reflector Lothar designed for the Planck project. Secondly a concept is shown to investigate the effects of the foundation and soil-structure interaction onto the dynamic performance of the telescope structure.

An efficient approach for integrated modeling of a telescope system is presented in chapter 5. After explaining the principles of the concept, the model architecture and capability are described in detail. The major VLTI components, control loops and disturbances are included into the model. Some examples for simulations with the VLTI Integrated Model are given and the results are discussed.

Finally, chapter 6 provides a concluding summary and open questions for integrated modeling of future telescope systems.



## 2 Major components in telescope systems for integrated modeling

### 2.1 Outline

The major task of a telescope is collecting light from a stellar object and redirecting it towards an optical instrument. A telescope model assembled of the main components is schematically drawn in figure 2.1. Certainly the optics are the central component providing an optical instrument at the telescope exit the required photons to measure intensity distributions or the spectral content. To allow the optical systems to operate properly they are mounted on the mechanical structure which gives the systems the required stiffness to keep shape and relative positions to each others. Observing a stellar object the telescope structure must incorporate systems for pointing toward the object and for tracking to compensate for the rotation of the earth. Tasks like pointing and tracking can only be solved by control loops consisting of sensors and actuators which are connected with a controller.

In real live the systems are always disturbed. This starts with the incoming wavefront, continues with external loads deflecting the structure and ends with all components, which have (small) variabilities in their geometry, material properties and output signals. For the incoming wavefront disturbing effects include atmospheric turbulence distorting the phase, the refraction of the atmosphere or stray light. Loads on the mechanical structure on ground based telescopes are, e.g., wind loads, seismic loads,

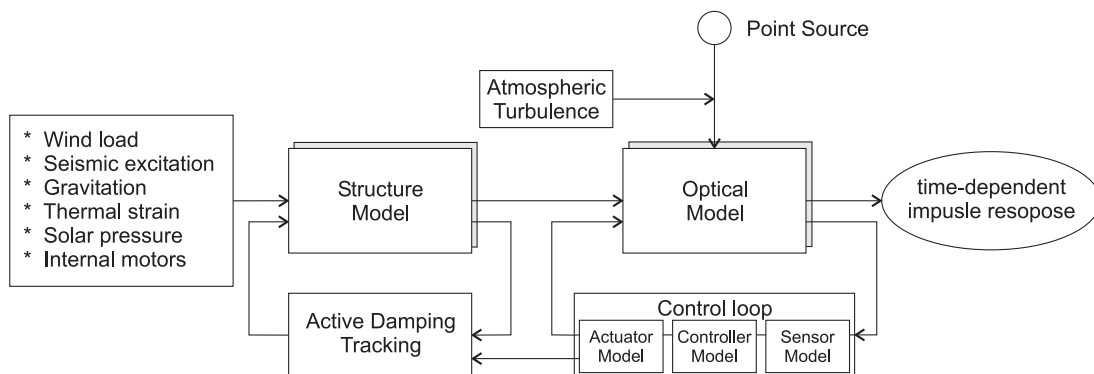


Figure 2.1: Scheme of a telescope system with major components required in an integrated model.

gravity and thermal strain. Control loops, which are required for tracking and compensating for errors, suffer not only from finite bandwidth of controllers, but also from sensor and actuator noise as well as the limited actuator dynamics. In space applications disturbances are different. Due to the absence of an atmosphere there is neither wind load nor the fluctuation in the incoming wavefront. Instead of this, the guidance and navigation system, gyroscopes and on-board coolers can cause disturbances. Moreover solar pressure and gravitational gradients potentially interfere with the system.

In the following sections the physical background for understanding the different components will be given while focusing on ground-based telescopes. Relevant concepts for modeling and evaluation will be derived.

## **2.2 Optics in telescopes and interferometers**

Depending on the relevant phenomena, optics is described with the different physical models of geometrical optics, wave-optics and quantum optics. In telescope optics most effects can be described with geometrical optics, where a light ray is propagating along a straight path until it is absorbed, reflected or refracted due to a change in the material properties respectively the refraction index. Geometrical optics often uses the wavefront and the optical path length (OPL) to describe the light propagation.

### **2.2.1 Wavefront errors and Zernike polynomials**

The wavefront is a surface of constant phase or constant optical path length <sup>1</sup> in a propagating electromagnetic wave. The geometrical optical wavefront is orthogonal to the rays. For a source located at very far distances like a star, the wavefront received at the telescope is a plane. Near the focus of a perfect optical system, the wavefront becomes a portion of a sphere centered at the focus. (see figure 2.2).

If the wavefront is not spherical after exiting the optical system, the rays will not converge to the same position in the image and the image will not be perfect. Propagating a grid of rays through the telescope, the actual wavefront can be computed by evaluating the optical path lengths. The deviation of the wavefront from a plane or a sphere is called the wavefront error. The magnitude of the error is usually measured as root mean square (rms) of the entire wavefront and traditionally a system with an rms of the exit beam (expressed in fraction of the wavelength) smaller than  $\lambda/14$  is said to be nearly perfect.

---

<sup>1</sup>optical path length = the geometric path of the light ray scaled by the refraction index:  $OPL = \int n ds$  with  $n =$  refraction index

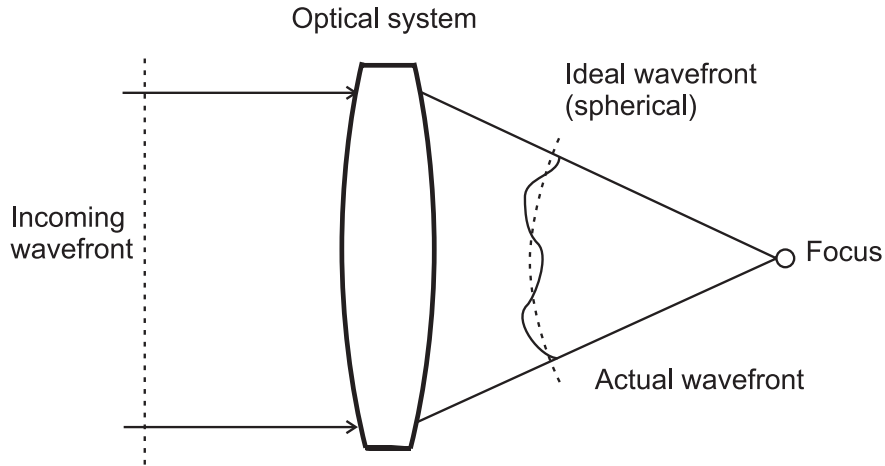


Figure 2.2: Focussing of a plane wavefront by an optical system. Close to the focus the wavefront error is the deviation of the actual wavefront from a sphere.

The wavefront error is often expressed in terms of Zernike modes introduced in 1934 by F. Zernike [19], who slightly modified them from Jacobi polynomials for use in optics. They are a set of orthogonal polynomials defined on a circular disc with unit radius:

$$W(r, \phi) = \sum_m \zeta_m \psi_m(r, \phi) \quad (2.1)$$

The wavefront error  $W(r, \phi)$  at the polar coordinates  $(r, \phi)$  is composed of the Zernike coefficients  $\zeta_m$  and the Zernike polynomials  $\psi_m(r, \phi)$  [20, 1]. A general formula for the polynomials can be found in [4, p. 279]. Due to the orthogonality of the polynomials, the coefficients are given by

$$\zeta_m = \frac{1}{\pi g_m^2} \int \int_{aperture} W(r, \phi) \psi_m(r, \phi) r dr d\phi \quad (2.2)$$

with the rms value  $g_m$  of the individual polynomial  $\psi_m$

$$g_m = \sqrt{\frac{1}{\pi} \int \int_{aperture} \psi_m(r, \phi) \psi_m(r, \phi) r dr d\phi}$$

Different normalizations for the Zernike polynomials are common, e.g. the wavefront error in meters or an rms-value for each one over the circle to  $g_m = 1$ . Figure 2.3 shows the first eight Zernike polynomials with formula. The major advantage of using Zernike polynomials is on the one hand the physical meaning, since each polynomial corresponds to a classical aberration like astigmatism, coma or spherical aberration<sup>2</sup>, and on the other hand the orthogonality, which allows to compute the total error by adding the errors of the individual polynomials:  $rms = \sqrt{\sum rms_m^2} = \sqrt{\sum (g_m \zeta_m)^2}$  with the weighting  $g_m$ , which equals the rms of the polynomial  $\psi_m(r, \phi)$ .

<sup>2</sup>This is valid at least for the lower order aberrations.

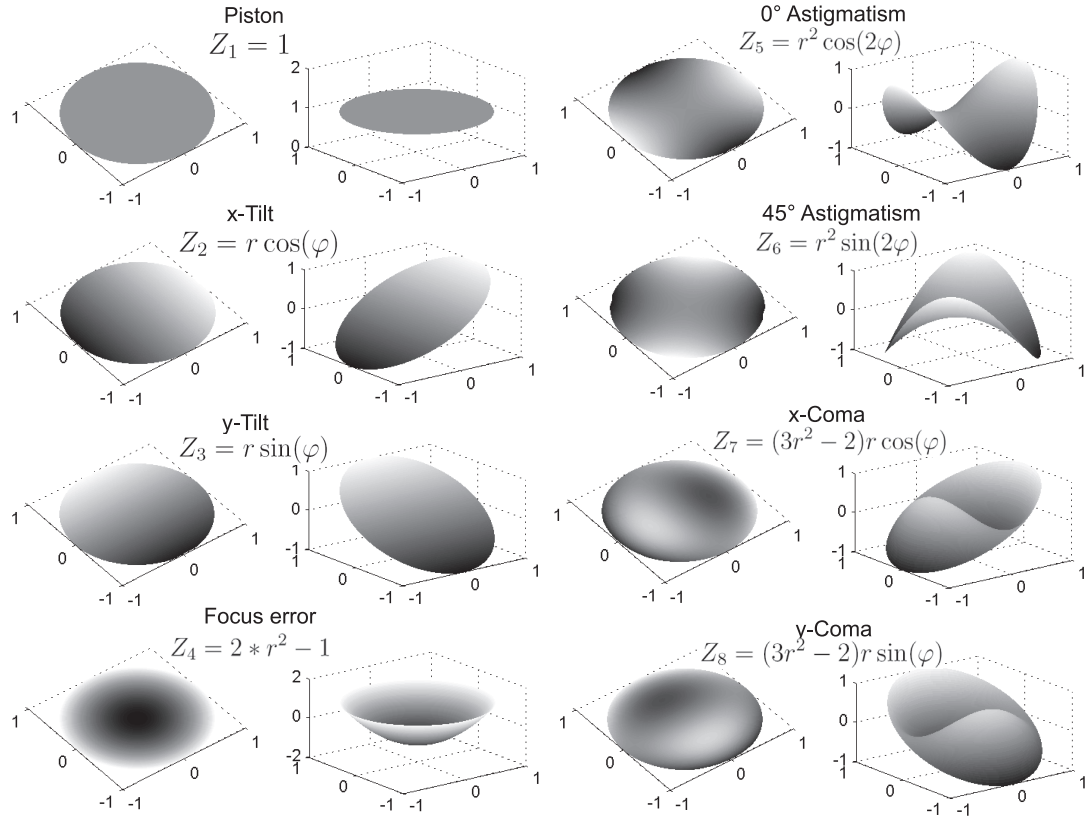


Figure 2.3: The Zernike polynomials are used to express wavefront error. This figure shows the polynomials  $\psi_1 - \psi_8$  with formula and the name describing the optical meaning.

For a set of  $n_j$  spatially uniformly distributed points<sup>3</sup>  $(r_j, \phi_j)$  ( $j = 1..n_j$ ) the Zernike coefficients  $\{\zeta\} = \{\zeta_m\}$  corresponding to  $n_i$  polynomials  $\psi_i$  ( $i = 1..n_i$ ) can be computed in a least square sense from the equation in matrix form using the pseudo-inverse  $\psi^+ = (\psi^T \psi)^{-1} \psi^T$  to minimize the error  $\Delta = \sum_j (\{W_j\} - \sum_i ([\psi_{ji}] \{\zeta_i\}))^2$ ;  $(\{W\} = \{W_j\} = \{W(r_j, \phi_j)\}; \psi = [\psi_{ji}] = [\psi_i(r_j, \phi_j)], (n_j > n_i))$ :

$$\{W_j\} \stackrel{!}{=} \sum_i [\psi_{ji}] \{\zeta_i\} \quad \rightarrow \quad \{\zeta\} = [(\psi^T \psi)^{-1} \psi^T] \{W\} = \psi^+ \{W\} \quad (2.3)$$

The low order Zernike polynomials describe aberrations of small spatial frequencies and are effective to describe wavefront errors of low and medium spatial frequency. They are also used for atmospheric wavefront distortion and mirror deformations. For very high spatial frequency errors caused by turbulent air, dust or micro-roughness on mirror surfaces, the Zernike polynomial representation is impractical. Instead of this statistical errors are added onto the wavefront.

<sup>3</sup>The condition of uniformly distributed points implies, that each point represents the same mirror area and thus is equally important.

### 2.2.2 Diffraction effects and image quality

A limitation of the geometrical optical interpretation are diffraction effects, where the wave nature of light becomes relevant. Most of the telescope optics can be handled with geometrical optics, but diffraction optics is essential for the theoretical limitations of resolution and the tolerancing of optical errors.

To understand the effects of diffraction, the wave effects of incident rays will be analyzed in more detail. The electric field  $\psi(\mathbf{r}, t)$  can be written for one polarization of a locally homogeneous plane wave as the real part of the complex amplitude

$$\psi(\mathbf{r}, t) = A(\mathbf{r})e^{i(\omega t - \mathbf{k}\mathbf{r})} = A(\mathbf{r})e^{i(-\mathbf{k}\mathbf{r})}e^{i\omega t} \quad (2.4)$$

Here is  $\mathbf{k} = 2\pi/\lambda \mathbf{i}$  the wave vector with the the unit vector  $\mathbf{i}$  denoting the direction of the light ray,  $\lambda = \lambda_0/n = c/(n\nu)$  the wavelength,  $n$  the index of refraction,  $nz$  the optical path,  $\omega = 2\pi\nu$  the angular frequency and  $A(\mathbf{r})$  a spatial complex function for the amplitude. Setting the temporal term and the phase contained in  $A(\mathbf{r})$  to 0, the phase  $\phi(\mathbf{r}) = \arg(e^{i(-\mathbf{k}\mathbf{r})})$  is the optical path  $z$  divided by the wave number:  $\phi = z/k = 2\pi z/\lambda$ .

Figure 2.4 shows a plane wavefront arriving at an aperture of diameter  $D$ . The light propagates through an optical system symbolized by a lens, and the light intensity is measured in the focal plane. To compute the amplitude of the electrical field in a point of the focal plane, the contributions of the individual points of the wavefront can be coherently added, while each point in the wavefront can be treated as a point source. The focal point has equal optical path length to all points on the plane wavefront perpendicular to the optical axis. A point  $P(X, 0)$  in the focal plane will have a constant optical path to a wavefront tilted by an angle  $\theta = X/f$  (with focal length

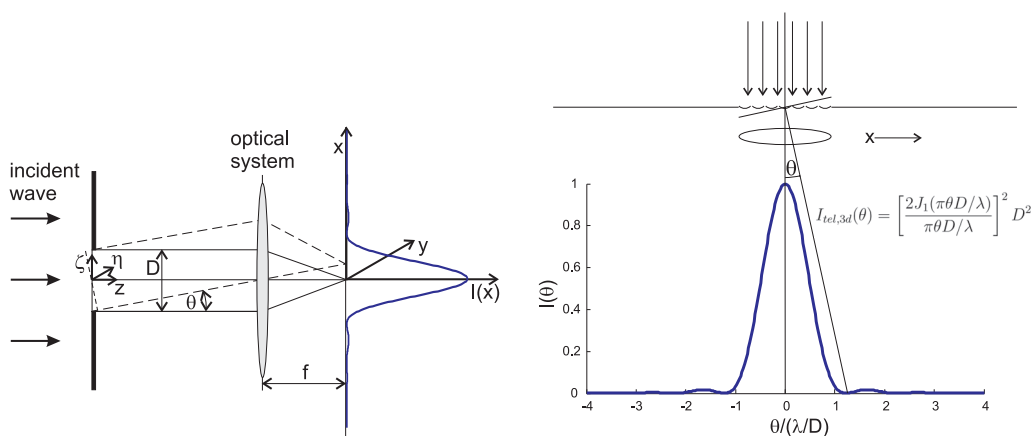


Figure 2.4: A plane wave arrives at an aperture with diameter  $D$ , passes an ideal optical system and creates an image in the focal plane. Due to diffraction the image of the point source is not a point, but an intensity distribution as shown in the plot.

$f$ ). Therefore, considering only the 2-dimensional case (i.e. neglecting the dimension  $\eta$  respectively  $y$ ) the phase arriving at the focal plane is (neglecting a constant term) dependent on  $\theta$  and the position in the aperture plane  $\zeta$ :

$$\phi = 2\pi\zeta \sin(\theta)/\lambda \simeq 2\pi\zeta\theta/\lambda \quad (2.5)$$

Summing now the electric fields of the individual wavelets results in the electric amplitude  $A_{tel}(\theta)$ :

$$\begin{aligned} A_{tel}(\theta) &= \sum(\text{wavelets}) = \int_{\text{aperture}} e^{i\phi(\zeta)} d\zeta \\ &= \int_{-D/2}^{D/2} e^{i2\pi\zeta\theta/\lambda} d\zeta = \frac{\sin(\pi\theta D/\lambda)}{\pi\theta D/\lambda} D \end{aligned} \quad (2.6)$$

The measured intensity is the squared magnitude of the amplitude:

$$I_{tel}(\theta) = |A_{tel}|^2 = \left[ \frac{\sin(\pi\theta D/\lambda)}{\pi\theta D/\lambda} \right]^2 D^2 \quad (2.7)$$

Including the second dimension, the equation (2.6) reads according to figure 2.4

$$A_{tel} = \int \int_{\text{aperture}} e^{ik(\alpha\zeta + \beta\eta)} d\zeta d\eta \quad (2.8)$$

with  $\alpha \simeq x/f \simeq \sin(\theta)$ ,  $\beta \simeq y/f$ .

For a circular aperture this gives the well-known "Airy function" named after George Airy who first derived this formula.

$$I_{tel,3d}(\theta) = \left[ \frac{2J_1(\pi\theta D/\lambda)}{\pi\theta D/\lambda} \right]^2 D^2 \quad \text{"Airy function"} \quad (2.9)$$

$J_1(X)$  is here the Bessel function of the first order. The first zero-intensity  $I_{tel,3d}(\theta_{tel}) = 0$  is reached at  $\theta_{tel} = 1.22\lambda/D$ , which is also approximately the full width half maximum (FWHM), a measure for the spatial resolution.

The intensity distribution in the image of a point source is called the "point spread function" (PSF) and is a characteristic for the optical system. If a constant phase  $\phi_0$  is added to the incoming wavefront the exit amplitude  $A_{tel}$  will additionally have a constant factor  $e^{i\phi_0}$  while  $I_{tel}$  is unchanged. An off-axis source (by the angle  $\theta_0$ ) creates a tilted incoming wavefront and results in a shift of the output intensity distribution by  $\theta_0 f$ . Thus the piston (i.e. the first Zernike mode shape) does not change the image at all for a single aperture telescope and a tip/tilt error (the second and third Zernike mode shape) only moves the image without changing the shape. Higher order aberration degrade the image quality.

Equation (2.8) is mathematically the 2-dimensional Fourier transformation of an aperture function with value 1 inside the aperture and 0 outside. This can be generalized



defining a complex pupil function  $\underline{P}(r, \varphi) = P(r, \varphi)e^{ikW(r, \varphi)}$  in the polar coordinates  $(r, \varphi)$ , where  $k = 2\pi/\lambda$  is the wave number for the wavelength  $\lambda$ ,  $W(r, \varphi)$  is the wavefront error and  $P(r, \varphi)$  is the transmittance of the aperture, which is 1 for completely unobscured regions and 0 for fully obscured points. The obstruction and wavefront errors caused by a real optical system are dependent on the pupil geometry and obstructions (e.g. the secondary mirror M2) as well as the geometrical aberrations of mirror shapes and diffraction effects due to defects in optics surfaces or dust. It can be shown (see [21]), that the PSF of a point source is the two-dimensional Fourier transformation of this complex pupil function and hence, the optical system is fully described by the PSF. The image of a source with an arbitrary spatial brightness distribution can be computed by the convolution of the (arbitrary) intensity distribution with the PSF of the system. Wavefront errors of the incoming light can be handled by adding these additional errors to the complex pupil function, i.e. by multiplying  $P(r, \varphi)e^{ikW(r, \varphi)}$  with, for example, the atmospheric error  $e^{ikW_{atm}(r, \varphi)}$ . This results in a convolution in the image plane.

To evaluate an optical system the previous results allow to consider point sources only without losing generality. Errors can be tolerated by the PSF, since considering small optical aberrations the PSF will be dominated by diffraction effects and not remarkable change. With increasing aberrations the PSF will change its shape and the intensity will be spread onto a wider area. The ratio between the amplitude of the actual PSF to the one of an ideal image is called the Strehl ratio and is a measure for image quality,

$$\text{Strehl ratio} = 1 - \left(\frac{2\pi}{\lambda}\right)^2 (\Delta\phi)^2, \quad (2.10)$$

where  $\Delta\phi$  is the rms wavefront error in fractions of wavelength (for Strehl ratios  $> 0.5$ ). A diffraction limited optical systems where the diffraction effects are dominant and geometric errors can be neglected, requires a Strehl ratio larger than 0.8. This equals an rms wavefront error less than  $\lambda/14$ .

### 2.2.3 Stellar interferometers

In stellar interferometers the light collected by two or more spatially separated telescopes is combined. Figure 2.5 shows the intensity distribution for a source perpendicular to the plane of the both subapertures with diameter  $D$  and distance  $B$ . Analogously to equation (2.6) the contributions of the individual wavelets can be added respectively integrated:

$$\begin{aligned} A_{int}(\theta) &= \int_{aperture_1} e^{ik\theta\zeta} d\zeta + \int_{aperture_2} e^{ik\theta\zeta} d\zeta \\ &= [e^{ik\theta B/2} + e^{-ik\theta B/2}] \int_{-\frac{D}{2}}^{\frac{D}{2}} e^{ik\theta\zeta} d\zeta \\ &= 2 \cos(k\theta B/2) A_{tel}(\theta) \end{aligned} \quad (2.11)$$

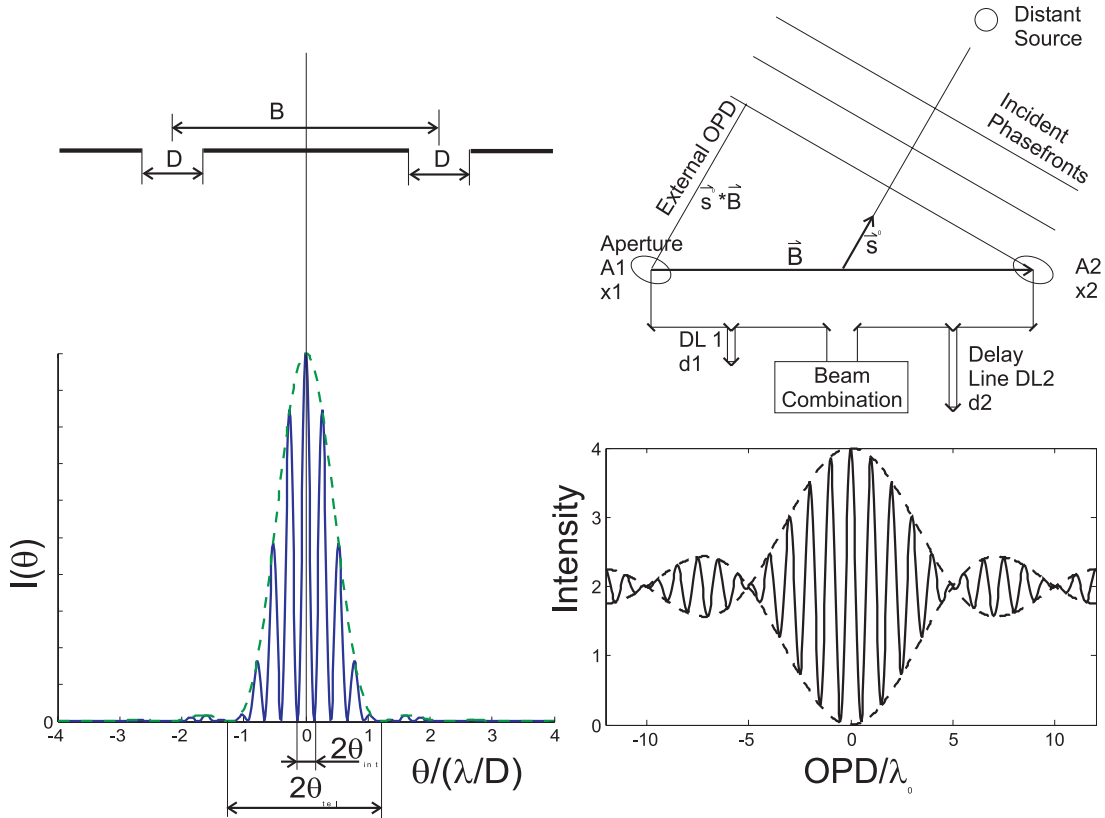


Figure 2.5: Simple model of an interferometer with baseline  $B$  and subaperture diameter  $D$ . The left graphic shows the intensity distribution, that is generated by the two subapertures in the focal plane for monochromatic light. The right graphic shows the dependence of the intensity at a beam combiner from the OPD for finite spatial bandwidth with a typical fringe pattern.

$$I_{int}(\theta) = 2I_{tel}(\theta)[1 + \cos(2\pi\theta B/\lambda)] \quad (2.12)$$

Figure 2.5 left displays the result for monochromatic light with an envelope function which equals the intensity pattern of a single aperture and the faster oscillating harmonic term  $1 + \cos(2\pi\theta B/\lambda)$ . The first zero  $I_{int}(\theta_{int}) = 0$  is reached for  $\theta_{int} = \lambda/(2B)$ , which is also the FWHM.

Hence a stellar interferometer allows a resolution which would correspond to an aperture diameter of the baseline length. This allows, e.g., a very precise localization of unresolved point sources on the sky.

A more realistic configuration for a stellar interferometer is shown in figure 2.5 on the right. The two apertures are separated by a baseline vector  $\vec{B}$  and pointing towards a point source located in  $s$  (with direction  $s^0 = s/|s|$ ). After arriving at the aperture the light has to pass through the telescope, the relay optics and the adjustable delay lines to be combined with the light of the other interferometer arm. In the beam combiner the total optical path difference OPD between both arms is composed of

the external component  $OPD_{ext} = \mathbf{s}^0 \circ \mathbf{B}$  and the internal  $OPD_{int} = d_1 - d_2$ . The arriving electric fields will have the phases:

$$\phi_1 \sim e^{ik(d_1 + \mathbf{s}^0 \circ \mathbf{B})} e^{i\omega t}, \quad \phi_2 \sim e^{ikd_2} e^{i\omega t} \quad (2.13)$$

With similar conditions in both arms the net field resulting from a superposition is given by:

$$\phi_{net} = \phi_1 + \phi_2 \sim e^{-i\omega t} \left( e^{ik(d_1 + \mathbf{s}^0 \circ \mathbf{B})} + e^{ikd_2} \right) \quad (2.14)$$

and hence, the time-averaged power is proportional to:

$$P \propto \phi_{net}^* \phi_{net} = 2(1 + \cos k(\mathbf{s}^0 \circ \mathbf{B} + d_1 - d_2)) \quad (2.15)$$

Neglecting loss inside the telescopes with aperture  $A$  each and including  $F$ , the incident power per area, gives:

$$P = 2AF(1 + \cos kOPD_{tot}), \quad (2.16)$$

where  $OPD_{tot} = OPD_{ext} + OPD_{int} = \mathbf{s}^0 \circ \mathbf{B} + d_1 - d_2$ . Thus, the resulting power  $P$  for the monochromatic case is a harmonic function of the total OPD called interference fringes.

Considering a certain bandwidth  $\Delta\lambda$  passed through the optics, the total power is the integral over the spectrum:

$$P = \int_{\lambda_0 - \frac{\Delta\lambda}{2}}^{\lambda_0 + \frac{\Delta\lambda}{2}} 2AF\lambda(\lambda)\eta(\lambda) \left[ 1 + \cos\left(\frac{2\pi}{\lambda_0} OPD_{tot}\right) \right] d\lambda, \quad (2.17)$$

where  $\lambda_0$  is the center wavelength of the band,  $\eta$  the finite efficiency in throughput and  $k = 2\pi/\lambda_0$  the wave number. For a small band the efficiency and the spectral intensity  $F_\lambda$  (in units of power per area per wavelength) can be assumed to be constant  $\eta(\lambda) \approx \eta_0$ ,  $F_\lambda(\lambda) \approx F_{\lambda_0}$ .

$$\begin{aligned} P(OPD_{tot}) &= 2AF_{\lambda_0}\eta_0 \int_{\lambda_0 - \frac{\Delta\lambda}{2}}^{\lambda_0 + \frac{\Delta\lambda}{2}} \left[ 1 + \cos\left(\frac{2\pi}{\lambda_0} OPD_{tot}\right) \right] d\lambda \\ &= 2AF_{\lambda_0}\eta_0\Delta\lambda \left[ 1 + \frac{\sin \pi OPD_{tot}/\Lambda_{coh}}{\pi OPD_{tot}/\Lambda_{coh}} \cos k_0 OPD_{tot} \right] \\ &= 2AF_{\lambda_0}\eta_0\Delta\lambda \left[ 1 + M_{coh}(\Lambda_{coh}, OPD_{tot}) \cos k_0 OPD_{tot} \right] \end{aligned} \quad (2.18)$$

with  $\Lambda_{coh} = \lambda_0^2/\Delta\lambda$ . Thus, the collected power is a function again oscillating with a term  $\cos k_0 OPD_{tot}$  as in the monochromatic case, but modulated in the amplitude by the modulation function  $M_{coh}(\Lambda_{coh}, OPD_{tot})$  with characteristic coherence length  $\Lambda_{coh}$ . A narrow band corresponds to a larger  $\Lambda_{coh}$  resulting in a wider modulation function. The maximum amplitude is reached for  $OPD_{tot} = 0$ , so the external OPD must be compensated by the internal due to driving the delay lines suitable. A typical fringe pattern with maximum contrast for  $OPD = 0$  is shown in figure 2.5.

The real OPD includes also phase delay in the incoming wavefront due to atmospheric turbulence and piston terms caused by vibrations of optical components like M1 or M2 due to wind load. To achieve the largest amplitude, these errors must be taken into account for adjusting the delay lines, what is done in stellar interferometers with a fringe tracking sensor and controller.

According to the von Cittert-Zernike theorem an arbitrary intensity distribution on the sky can be reconstructed from the measurements over all possible baseline vectors ([4]). Required is therefore the measurement of the complex visibility function  $V(k, \mathbf{B})$ , which is characteristic for the brightness distribution on sky (see also appendix D):

$$V(k, \mathbf{B}) = \int A(\Delta \mathbf{s}) F(\Delta \mathbf{s}) e^{ik(\mathbf{s} \cdot \mathbf{B})} d\Omega, \quad (2.19)$$

with the wave number  $k$ , the baseline vector  $\mathbf{B}$ , the aperture area  $A$ , the incident power per area  $F$  and the position on the sky  $\mathbf{s}$ .

To determine the visibility, the output power is measured, while the delay-line varies  $\delta$  according to a certain OPD modulation scheme. To operate the stellar interferometer the major requirement is to adjust the OPD compensating for all internal and external OPDs caused by the geometry of observation or disturbances. The higher order wavefront errors have also negative effects, as they reduce the contrast in the output fringes.

The essential advantage of an interferometer is the high resolution, which is achieved by synthesizing a large telescope of diameter of the baseline distance by smaller aperture diameters. This allows a precise astronomie measuring the position of a star or the stellar diameter.

### **2.2.4 Comparison and summary of wavefront errors**

Concluding the effects of wavefront errors onto the image, single aperture telescopes have to be considered separated from stellar interferometers. In single aperture optics piston terms in the wavefront have no effect onto the image and the tilt terms cause only an image motion. The higher order errors generate image blur. Especially a changing of the wavefront curvature (called defocus) cause a variation in the intensity, called scintillations. For interferometer the compensation of piston differences between the individual subapertures is essential, as the maximum contrast is reached for  $OPD_{tot} = 0$  and the fringes disappear for large  $OPDs$ . Uncompensated residual  $OPDs$  cause a shift of the fringe packets. The tilt terms and higher order aberrations result in a loss of efficiency, which results in lower fringe intensity at the instrument.

A method of “cleaning” a wavefront removing high-order wavefront errors before beam combination is modal filtering, where the light is coupled into an optical single

mode fiber. Exiting the fiber the light is in phase with a certain amplitude. However, wavefront errors cause loss in the efficiency of coupling the electric field into the fiber.

## 2.3 Mechanical structure of telescopes

The major task of the mechanical structure of telescopes is to support mirrors respectively optical instruments and to keep the optics on fixed positions within close tolerances. To satisfy the requirements of diffraction limited optics, these tolerances would be of the order of  $\lambda/28$  since  $OPD \approx 2 * \Delta z_{mirror}$  for a mirror displacement in the optical axis of  $\Delta z_{mirror}$ . Moreover the structure must incorporate mechanisms to provide pointing and tracking.

In former times the constructions had to keep the rms wavefront errors caused by changing gravitational effects due to changing mass and stiffness distributions while tracking below  $\lambda/14$  to allow diffraction limited imaging. Hence telescope tubes of parallelogram-type were built, which keep even for varying gravity load the tilt of the secondary mirror M2 small. In our days active optics compensate for such perturbations of low frequency and therefore the main goal for the mechanical structure is achieving high stiffness and high natural frequencies, which implies a low mass construction, while parallelogram type structures are still used to keep the actuator stroke small. A high natural frequency is not only desired because of the relation to good stiffness, but also due to the achievable bandwidth for tracking, which is limited with a few of the first relevant frequencies of the structure. An important constraint is, of course, the optical path, which has to be as less as possible covered with respect to the obstructed area as well as to the obstructed shape, which can cause diffraction effects in the image.

Achieving high natural frequencies, i.e., a high stiffness at low mass, is relatively easy for small systems, but difficult for large systems due to scaling laws. Table 2.1 shows the scaling of mass, stiffness, eigenfrequency and significant loads dependent on the size.

The scaling laws show that a large specific stiffness  $E/\rho$  is desirable, which is only depending on the material. To exceed the ratio of  $E$  to  $\rho$  of steel requires usually very expensive materials like CFRP or Beryllium, which are therefore limited to space applications or active secondary mirrors, where minimum mass is a main goal. Moreover a high Youngs modulus  $E$  is of advantage as it increases (linearly) the stiffness, reduces the deflection due to an external force like the wind load and helps to keep the total material volume smaller. Besides the specific stiffness and Youngs modulus the scaling laws are governed by the characteristic telescope dimension  $L$ . Though stiffness is rising with size, larger structures suffer from faster increasing loads like wind load or self weight and at the same time decreasing eigenfrequencies. That is the reason why gravity effects become more important. In addition to this the wind

quantity	symbol	formula	scaling low
mass	$m$	$\rho * V$	$\rho L^3$
stiffness	$K$	Force / Displacement	$EL$
eigenfrequency	$f = \frac{\omega}{2\pi}$	$f \propto \sqrt{K/m}$	$\frac{\sqrt{E/\rho}}{L}$
gravity deflection (self load)	$\Delta_g$	$gm/K$	$\frac{L^2}{E/\rho}$
wind deflection	$\Delta_w$	$F_w/K = c_D \frac{\rho}{2} U^2 A/K$	$\frac{L}{E}$

Table 2.1: Scaling lows for structures. (Typical dimension  $L$ , density  $\rho$ , Youngs modulus  $E$ , velocity  $U$ )

load is even increasing with falling frequency and therefore the dynamic effects due to wind excitation are more critical for larger telescopes.

Thus more attention must be paid on the design of the telescope structure for larger systems and as the structural dynamics of the telescope is shifted to lower frequencies, including this dynamic effects into an optical simulation becomes essential.

The common construction for large telescopes is a truss structure since frameworks provide a high stiffness especially for local forces while the area of attack for the wind load is relatively small. The mathematical description of mechanical structures is explained in chapter 3.1.

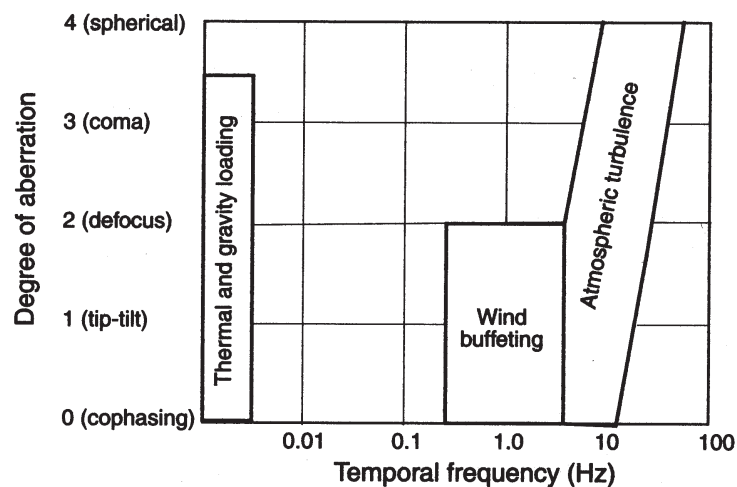


Figure 2.6: Frequency dependence and order of wavefront errors caused by different disturbances. (according to [1, p. 312])

## 2.4 Control loops

In telescopes control loops have an essential role to operate the systems, which all must satisfy general requirements like stability, robustness, disturbance rejection and efficiency within the desired bandwidth. There are several control tasks such as pointing and tracking, air conditioning or thermal control. These examples are all not directly dealing with image quality and are hence out of the scope here. The systems controlling optical quality are active and adaptive optics. The active optics compensate for quasi-static and low frequency errors (up to the order of some Hz), which are caused by gravitational or thermal effects. Usually the main optics like the primary mirror M1 or the secondary M2 are used for active optics. Since adaptive optics compensates for wavefront errors with higher frequency, light and relatively flexible mirrors (with respect to rigid mirrors of the main optics) are required (deformable mirrors), which are usually smaller in size. Figure 2.6 shows the effects of the different environmental disturbances with temporal frequency and the spatial degree of aberration. The highest frequency terms with also the highest spatial degree of aberration are caused by the atmospheric turbulence. Wind buffeting is smaller in frequency and causes mainly wavefront errors of the lowest orders. Thermal effects and gravitational load change very slowly.

Different control concepts exist, which can be divided into feedforward control, local feedback control and global feedback control. For feedforward control a disturbance is measured and if the behavior of the system is known, the disturbance effects can be fully compensated without measuring the output error. The major advantage of feedforward is the high bandwidth and a possible simple controller whereas modeling errors are not measured and can result in an offset. Examples for the application of feedforward control could be active optics compensating for gravitational loads while tracking (quasi-static), since the structural stiffness does not change much. The high bandwidth could be used for compensating for wind load by measuring the wind velocity upstream to predict the expected effects and steer against them before arriving.

In local feedback loops the error is measured within one component and directly compensated. Advantages are a high bandwidth while avoiding a steady state error by using an integral term in the controller. An example could be the control of mirror segments due to the signals of the edge sensors, which give very high accuracy. One drawback is that small errors within one component can add up over all components to a larger global error and often sensors suffer from drift for long measurement periods.

This is avoided in a global feedback loop, where a wavefront sensor measures the error of the complete wavefront. However these controllers are often complex systems and, as the reference signal is usually a faint star, the bandwidth of the sensors is limited.

A combination of the different control concepts allows often to benefit from all advantages while compensating the drawbacks with the other systems. Different wavefront sensors are used, one for active optics acting on the main optics and a different one for adaptive optics acting on a deformable mirror.

## **2.5 Disturbances**

The main disturbance for ground based telescopes is the atmospheric turbulence distorting the incident wavefront. Suffering from the turbulence the angular resolution of a ground based telescope in the visible is equivalent to an aperture diameter of 10-20cm. Only the application of adaptive optics allows better image quality. [20, 1]

### **2.5.1 Quasi-static and dynamic disturbances**

The atmospheric turbulence directly spoils the incident wavefront, whereas many other disturbance sources act on the telescope structure or the mirror structure irritating the image indirectly. The main sources on ground are gravity effects, thermal loads, wind load and seismic excitation (depending on the site).

Thermal load due to temperature variations or thermal gradients within the structure and gravity effects, which are caused by changing distributions of weight and stiffness while tracking, are quasi-static loads, which are mainly the concern of the telescope design with construction and material selection, but also compensated by active optics. The loads caused by wind and seismic activity are of higher frequency and hence exciting the structure dynamically.

In space applications different disturbances like gravity gradients, solar pressure and excitations inside the spacecraft become important, while not suffering from atmosphere decreasing the seeing and generating wind loads. In the following the dynamic disturbances for ground based telescopes will be explained.

### **2.5.2 Vibration sources for ground based telescopes**

The main dynamic disturbances acting on telescope structures are wind forces and base excitation. Moreover internal disturbance sources exist like motors, hydraulic systems, etc. Special care must be put on avoiding internal vibration sources e.g. by mounting motors on large mass concrete blocks, which are supported by soft springs to isolate the telescope from the vibration forces. For the telescope design the expected loads are divided into survival loads and operational loads for both the wind velocity and seismic excitation.



The survival loads are relevant for the telescope strength and instrument robustness, whereas the telescope performance must not degrade under the required level for operational loads. Table 2.2 shows exemplarily the requirements of ESO for the VLT on Paranal.

### Wind load

Wind load is caused by the inertia and friction of the flow creating both static and dynamic forces  $F$  on the structure. The static forces can be described with the formula

$$F = \frac{\rho}{2} U^2 A c_D, \quad (2.20)$$

with the force  $F$ , density  $\rho$ , wind speed  $U$ , the dynamic pressure  $q = \frac{\rho}{2} U^2$ , characteristic cross section area  $A$  and the drag coefficient  $c_D$ .  $c_D$ , the fluid mechanic dimensionless characteristic for drag, is a function of the geometry and the Reynolds number  $Re$ <sup>4</sup>

The dynamic forces can be caused by both wind gustiness, i.e. variations of the wind velocity  $U$ , and by vortex shedding. Vortex shedding is caused by the flow of the air around individual members with periodic separation of vortices (Von Karman vortices) resulting in alternating forces perpendicular to the wind direction. The resulting forces can be of the order of the static wind loads and excite vibrations of the structure.

The wind gustiness due to turbulence generates a varying load in the wind direction. Different analytical and empirical models exist for describing the power spectrum of the turbulent wind velocity. One commonly used is the Von Karman spectrum:

$$S_u(f) = \frac{4I^2UL}{U(1 + 70.8(fL/U)^2)^{5/6}} \left[ \frac{(m/s)^2}{Hz} \right], \quad (2.21)$$

where  $S_u(f)$  is the PSD of the wind speed,  $U$  the mean wind velocity,  $f$  the frequency and  $L$  the outer scale, which is a characteristic length for the turbulence and which

<sup>4</sup> $Re = UL/\nu$  describes the relation between the influence of inertia compared to the influence of friction inside the flow (with velocity  $U$ , characteristic length  $L$  and kinematic viscosity  $\nu$ ).

Survival wind speed	50 m/s
Survival earthquake	8.5 Richter
Maximum operational wind	20 m/s
Maximum operational wind gust	30 m/s
Maximum operational earthquake	7.75 Richter

Table 2.2: Design specification for the VLT of ESO on Paranal [22]

is typically 80m in open air and smaller inside a dome. (E.g. for an analysis of wind effects for the VLT  $L=20\text{m}$  was chosen for the top unit with top ring (TR) and the tube (TU) and  $L=3.2\text{m}$  was chosen for the mirror M1.) The turbulence intensity  $I = \sigma_u/U$  is a measure for the variation of the wind speed (e.g.  $I = 16\%$  for the VLT study).

The resulting power spectrum for the wind force  $F$  is similar to  $S_u(f)$ :

$$S_F(f) = 4 \left( \frac{\bar{F}}{U} \right)^2 S_u(f) \chi_a^2(f); \quad \chi_a(f) = \frac{1}{1 + \left( 2f \frac{\sqrt{A}}{U} \right)^{4/3}}, \quad (2.22)$$

with the static force  $\bar{F}$ , the characteristic area facing the wind  $A$  and the aerodynamic attenuation factor  $\chi_a^2(f)$ , which reduces the effective wind load due to a partially decorrelation over the telescope area. For larger telescopes  $\chi_a^2(f)$  can significantly reduce the effective force. Figure 2.7 shows the aerodynamic attenuation factor. On the left graphic the rising attenuation for increasing frequency can be seen. The corner frequency is depending on the area  $A$ . The right plot shows the attenuation with increasing area  $A$  while keeping the frequency and the velocity constant.

In figure 2.8 two examples for the PSDs of wind according to the Von Karman spectrum are given which correspond to the values chosen for a VLT model. For larger  $L/U$  ( $L = 20\text{m}$ ,  $U = 10\text{m/s}$ , which corresponds to TU and TR)  $S_u(f)$  has higher values for small frequencies, but the corner frequency, where the PSD starts to fall, is reached at a lower frequency. The second graph with  $L = 3.2$  and  $U = 10\text{m/s}$

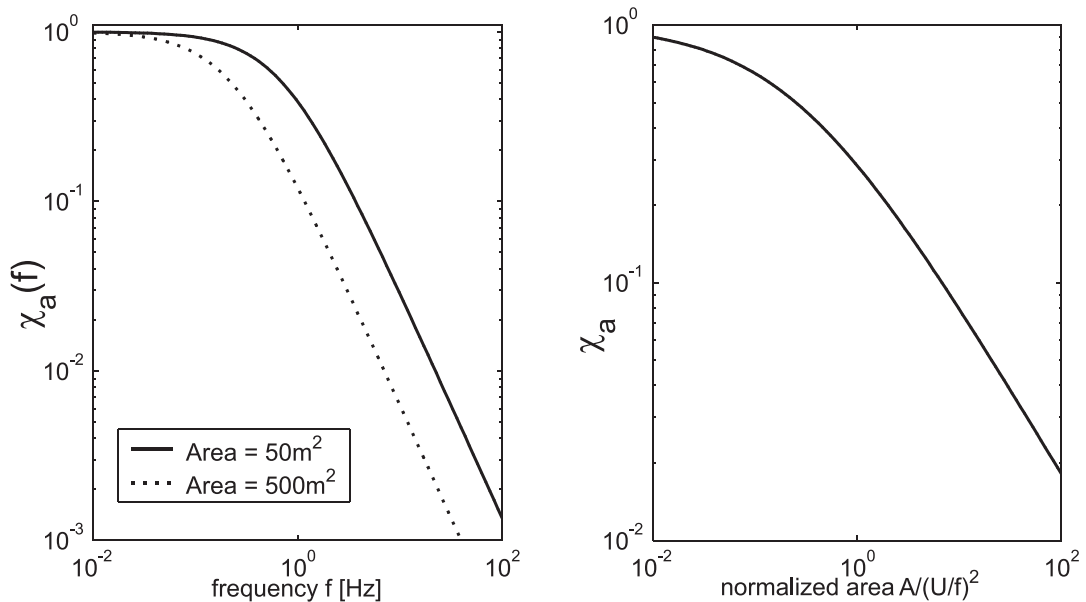


Figure 2.7: The aerodynamic attenuation factor is a function of the frequency, the effective area and the wind velocity. The left plot shows the frequency dependence, the right plot the attenuation for large effective areas.

represents the conditions at mirror  $M1$ . Due to the minor  $L$  the initial power is smaller until the other graph is intersected at about 0.2Hz and is then higher, since the corner frequency is shifted to the right. Including the attenuation factor due to an effective area of  $A = 100m^2$  shows the significant reduction for higher frequencies.

For a simulation of the dynamic effects of the wind load, the approach and the effort is much depending on the level of detail and the effects to be studied. If, e.g., only the global effects like the total moment causing a tilt on the tube and on mirror  $M2$  is under research, a rougher computation of the dynamic wind forces is sufficient. However, if for example the effect of wind gusts moving over the individual segments of  $M1$  is simulated, the spatial and temporal distribution of forces should be modelled in more detail what will probably require a computational fluid dynamics (CFD) analysis or wind tests.

For a rougher computation the static wind load can be computed according to a civil engineer norm, e.g. the German DIN 1055-4. A wind profile over the telescope height over ground is calculated. The structure is split into different components and for each component the aerodynamic drag coefficient is determined from a table. Including an attenuation factor for mutual obstruction, the static forces can be computed for all sections. To analyze the total effect of wind load, the coherence of the different sections should be considered. A common formula for the coherence over the distance is  $\langle u(r), u(r + \Delta r) \rangle = \exp(-Cf \frac{\Delta r}{U})$  with a constant  $C$  between 4 and 8 for typical outdoor conditions 30m above ground [23].

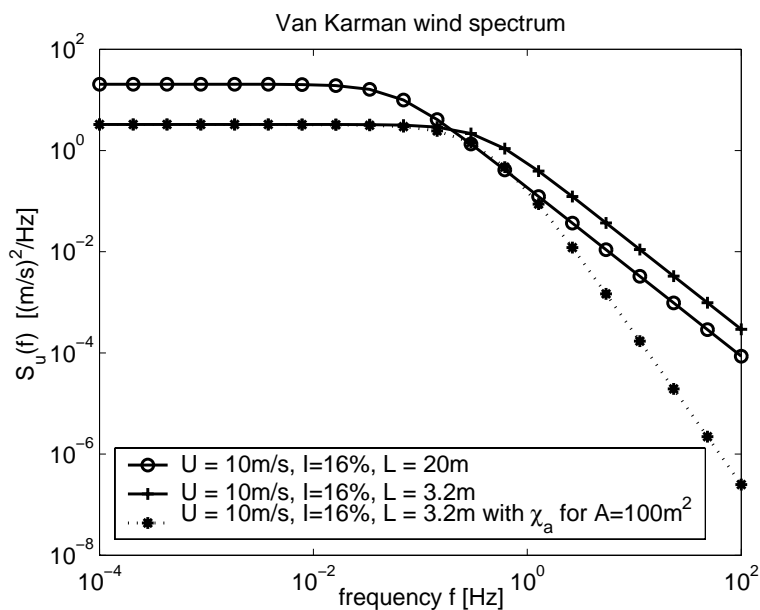


Figure 2.8: PSD of the wind velocity for the Von Karman turbulence model. For high frequencies the PSD decreases  $\propto f^{-5/3}$

Figure 2.9 shows the transfer functions and resulting PSDs for the mirror motion in  $y$ -direction and the OPL variation due do wind load on mirror M1 of the UT of VLT. As can be seen in the transfer functions (left) a mechanical structure behaves like a low pass filter with falling amplitude for higher frequencies. This and the typical wind force profile with decreasing amplitude for higher frequencies are the reasons why the telescope stiffness and first modes have the largest contribution to the total wavefront error due to wind load. This has to be considered for the condensation of a dynamic telescope model.

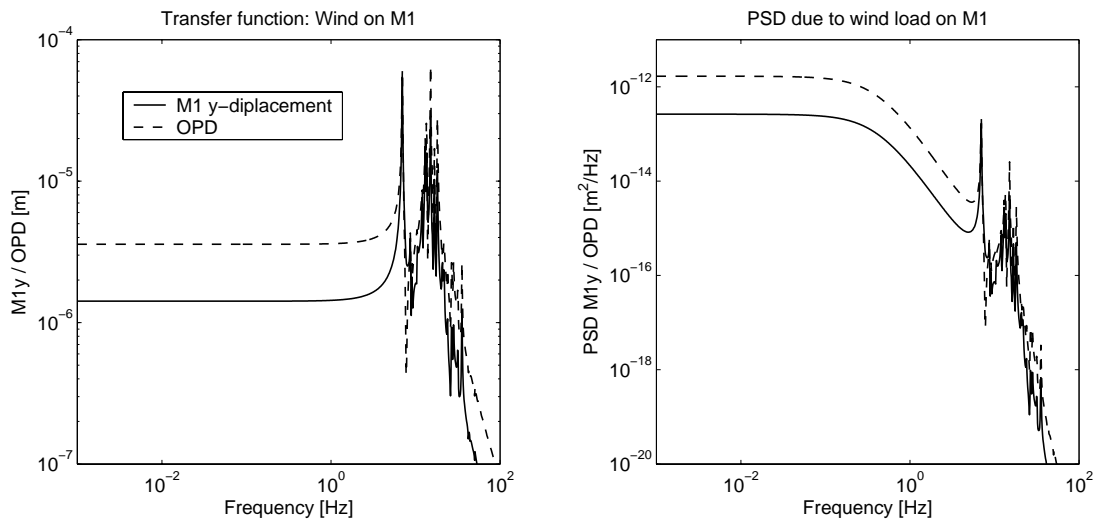


Figure 2.9: Wind load (in  $y$ -direction) onto mirror M1 of the UT of VLT: The left plot shows the transfer function for the mirror displacement in  $y$ -direction and the OPL. The right plot shows the resulting PSDs assuming an respective wind PSD profile for wind velocity  $U = 10m/s$ .

### Seismic load

Seismic load is an excitation of the telescope structure due to acceleration of the foundation, which can have different sources like the natural seismic noise and seismic events with larger amplitude. They can also be caused by a driving car close to the observatory or even by walking persons or wind load exciting the enclosure.

Many of the best observation sites are located on seismic active regions like Paranal or Hawaii. The magnitude of the different excitation sources must be investigated and the effects evaluated.

An example for a typical seismic event of Paranal, which type is expected to occur three times per night, is shown in figure 2.10. Unlike the wind load the ground acceleration is decreasing with falling frequency. A large amplitude can be found from 5 to 100 Hz with about the same order of magnitude. This is critical, since the first telescope modes are laying inside this region with high excitation amplitude.

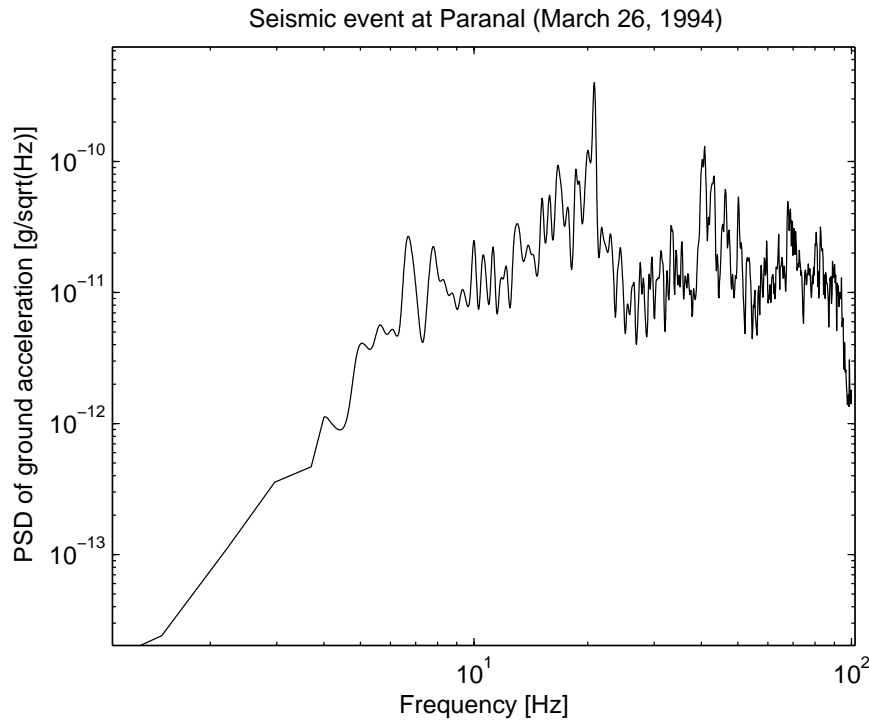


Figure 2.10: Typical seismic event at Paranal. This type of event occurs three times per night in mean.

### 2.5.3 Turbulence

#### Atmospheric Turbulence

The atmosphere is never fully calm as wind and convection induces turbulence. The Reynolds number  $Re = UL/\nu$  (fluid velocity  $U$ , characteristic length  $L$  and kinematic viscosity  $\nu$ ) describes whether the flow is laminar or turbulent. Since  $L$  is between several meters and kilometers for the atmosphere and  $\nu = 1.5 \cdot 10^{-5} \text{m}^2/\text{s}$  of air,  $Re$  exceeds the critical value already for velocities of a few  $\text{m/s}$  ( $Re > 10^5$ ) and therefore the flow is nearly always turbulent.

The turbulence causes a mixing of layers of different height with varying temperature, pressure and density. The index of refraction  $n$  is a function of the density and therefore of the pressure and temperature, where effects due to the temperature variations are dominant. If an air parcel moves to a different height without exchanging energy with the environment, the density, temperature and pressure changes adiabatically. The difference of the refraction indices of the new air parcel and the environment are dependent of the temperature gradient and there is only no difference for layers having the adiabatic lapse rate as temperature gradient ( $\partial T/\partial H = \gamma_a = -9.8 \text{K}/\text{km}$ ). For inclining height the density and also the refraction index decrease. That is the reason why the effects due to atmosphere higher than 20km can be neglected.

The turbulence is initiated from shear between two layers due to wind or buoyancy causing large eddies of the size of the outer scale  $L_0 \approx 1..100m$ . These large eddies generate smaller ones nearly without dissipation, but only by redistribution of energy. This process continues in the so called “inertial subrange” until in smallest eddies the shear rate becomes large and the dissipation of kinetic energy into heat becomes the dominant effect. This dissipation subrange is of the order of the inner scale  $l_0 \approx 10^{-3}m$ . Thus the energy flow rate  $\epsilon_0$ , describing the transfer of energy through a structure of a size  $l$ , is constant:  $\epsilon_0 = E(L)/t(L) = E(l)/t(l) = (mU^2/2)/(l/U) = const$ . Consequently turbulence intensity is a function of  $\epsilon_0$  and the spatial frequency  $\kappa$  describing the eddy size.

This turbulence model is called the Kolmogorov model and the velocity distribution is characterized by the constant  $C_v^2$  which defines the structure function:

$$D_v(R_1, R_2) = \langle |v(R_1) - v(R_2)|^2 \rangle = C_v^2 |R_1 - R_2|^{2/3} \quad (2.23)$$

It can be shown that the variations of temperature and refraction index are also described by a structure function like equation (2.23) only with the constants  $C_T$  respectively  $C_n$ , which depend on  $C_v$ . The phase shift produced by the varying refraction index  $n$  is

$$\phi(x) = k \int_0^\infty n(x, z) dz \quad (2.24)$$

This integral over the refraction index is characterized by the Fried parameter  $r_0$  taking into account the zenith angle  $\gamma$ :

$$r_0 = [0.423k^2(\sec \gamma) \int C_n^2(h) dh]^{-3/5} \quad (2.25)$$

The Phase-Coherence function  $B(r)$  can be expressed with  $r_0$ :

$$B(r) = \langle \exp(i[\phi(x) - \phi(x+r)]) \rangle = \exp\left(-3.44 \left(\frac{r}{r_0}\right)^{5/3}\right) \quad (2.26)$$

The Fried parameter characterizes seeing and has a physical meaning: “ $r_0$  is the diameter of the area in the incoming wavefront where the rms of the phase fluctuation is 1 radian (i.e., within which the beam is essentially in phase).” ([1, p.448]) For a diffraction limited image,  $r_0$  must be about 1.6 times the aperture diameter. After removing the wavefront tilt, the observation would be without any significant effects due to atmospheric turbulence. For large telescopes with aperture diameters  $D \gg r_0$  the FWHM of the image is given for the wavelength  $\lambda$  by [1]

$$FWHM = 0.98 \frac{\lambda}{r_0} \quad (2.27)$$

According to equation (2.25)  $r_0$  is a function of the wavelength (respectively of  $k = 2\pi/\lambda$ ):  $r_0 \propto \lambda^{6/5}$ , what has to be considered for the seeing, i.e., the seeing is

decreasing slowly with increasing wavelength ( $\frac{\lambda}{r_0} \propto \lambda^{-1/5}$ ). For usual wind velocities  $U$  of some meters per second the turbulent atmosphere can be considered as frozen and a coherence time  $\tau_0$  can be defined as the time required to move a coherent ray bundle over a certain point:

$$\tau_0 = \frac{r_0}{U} \quad (2.28)$$

Due to averaging over the area for larger apertures at certain  $r_0$  the tilt decreases while the rms increases. It is possible to express the wavefront error caused by atmospheric turbulence in terms of Zernike polynomials. However, an explicit form for the power spectral density of the individual polynomials cannot be given, but they can be given in an integral form, which has to be evaluated numerically. The Kolmogorov power spectrum of the phase fluctuations can be calculated to

$$\Phi(k) = 0.023r_0^{-5/3}k^{11/3} \quad (2.29)$$

The variance of the phase is the integral over  $\Phi(k)$ , which is not finite due to the piston term. Assuming a von Karman spectrum with finite outer scale gives also a finite variance.

A possible concept for computing the required wavefront errors in terms of Zernike coefficients for an array of apertures like for an stellar interferometer consists of several steps:

- Generate a large phase screen due to the Kolmogorov spectrum according to equation (2.29).
- This phase screen is assumed to be frozen and is moved with the wind velocity  $U$  over the site. Therefore the required phase screen must have the size of the site plus a length  $l = Ut$ , where  $t$  is the time, which will be simulated. For each time the section of the phase screen covering the respective aperture is extracted.
- From the time history of individual phase screens the Zernike coefficients can be calculated.

This approach includes also correlation effects due to the separation of the individual apertures by the baselines.

Due the baseline distance between the telescopes this requires a very large phase screen reducing the possible spatial resolution. That is the reason why in a modified concept analytical formulas are used for the piston and tip/tilt term considering the correlation effects due to the baseline vector, whereas the time-histories for the higher order aberrations are generated without correlation effects.

A formula for the piston effects for frequency  $f$  is

$$S_{OPD}(f) = \begin{cases} C f_{Kol}^{-\frac{2}{3}} \left(\frac{f}{f_{Kol}}\right)^{-\frac{2}{3}}; & f < f_{Kol} \\ C f^{-\frac{2}{3}}; & f \geq f_{Kol} \end{cases} \quad f_{Kol} = \left( \frac{6.88}{C} \left( \frac{\lambda}{2\pi} \right)^2 \left( \frac{B}{r_0} \right)^{-\frac{3}{5}} \frac{5}{18} \right)^{-\frac{3}{5}} \quad (2.30)$$

with the constant  $C = 21.38e-3\lambda^2 T_0^{-5/3}$ , the Kolmogorov cut-off frequency  $f_{Kol}$ , the baseline  $B$ , the atmospheric coherence time  $t_0 = 0.314*r_0/U$  at reference wavelength  $\lambda$  and wind velocity  $U$ . The coherence time  $T_0$  is a different definition related to  $t_0$  as  $t_0 = T_0/2.58$ . To include the averaging effects of the aperture diameter  $D$  a second cut-off frequency  $f_c$  is computed and  $S_{OPD}$  adjusted to  $S_{OPD}^D$  for frequencies  $f > f_c$ :

$$f_c = \frac{3f_{Kol}B}{2D}; \quad S_{OPD}^D(f > f_c) = S_{OPD} \frac{f^{-3}}{f_c^{-3}}; \quad f > f_c \quad (2.31)$$

[24, 25]

For the tilt without including correlation effects due to the baseline the power spectral density can be given as:

$$S_{Tilt}(f) = C f^{-2/3}; \quad C = \frac{4 \cdot 0.804}{0.423 \cdot 4\pi^2} \lambda^2 r_0^{-5/3} (\bar{U}_{-13})^{-1/3} \quad (2.32)$$

with the averaged velocity  $\bar{U}_{-13} = [\langle C_N^2 \cdot v^{-1/3} \rangle / \langle C_N^2 \rangle]^{-3}$  in [m/s] (typical value  $\bar{U}_{-13} = 4.4m/s$ ).

Again including averaging effect of the aperture gives a cut-off frequency  $f_c$  and a modified spectrum  $S_{Tilt}^a$ :

$$S_{Tilt}^a(f > f_c) = C f_c^3 f^{-11/3}; \quad f_c = \frac{0.011}{0.804} D^{-3} \bar{U}_{83}^{8/3} (\bar{U}_{-13})^{1/3}; \quad (2.33)$$

with the averaged velocity  $\bar{U}_{83} = [\langle C_N^2 \cdot v^{8/3} \rangle / \langle C_N^2 \rangle]^{-8/3}$  in [m/s] (typical value  $\bar{U}_{83} = 8.0m/s$ ).

[26, 20, 1, 3, 27]

### Internal turbulence

In stellar interferometers the rays have to be directed from the telescope primary mirrors to the beam combiner. Depending on the conditions inside, e.g., the delay line tunnel, internal turbulence can give significant contributions to the wavefront error. For the OPD control this has to be considered, but is no serious problem, if the OPD sensor is located at the beam combiner, i.e., it directly measures the errors. The wavefront sensor is usually located inside the telescope and therefore higher order errors like tilt cannot be corrected and degrade thus directly the efficiency.

To include this disturbance into simulations, measured or computed PSDs can be applied. The effects of internal turbulence can be avoided by vacuum tunnels or by advanced air conditioning inside the tunnel.



### 2.5.4 Noise

Each sensor and actuator suffers more or less from noise in signals. The relevancy can be much different and depends on the respective component. In a simulation the noise (white or colored) can be including by adding random signals to the sensor signals or actuator output.



# 3 Model reduction for dynamic structural models

This chapter focuses onto the modeling of a telescope structure for use in an integrated model. After the governing equations for structural dynamics are shortly repeated, formulations for applying input loads and provide outputs are given. System size and accuracy is crucial for a time-dependent simulation and hence model reduction is dealt with. Especially balanced model reduction is explained in detail, while other methods are shortly described. Finally examples of reduced models for usage in integrated modeling are given applying the toolbox SMI, which was developed at the Institute of Lightweight Structure for model reduction of mechanical structures.

## 3.1 General mathematical description of telescope structures

For the mathematical description of telescope structures some limiting properties are assumed, which are generally in a good approximation satisfied by telescope structures:

**Linearity** The assumption of linearity means both linearity of the material, i.e. a material with linear elastic constitutive equations, and the geometric linearity. Geometric linearity implies only small deformations of the structure and e.g. no stability problems, where the deformed structured has an impact on the stiffness distribution. Consequently the mass and stiffness matrices do not change with the load.

**Time-invariance** The mathematical model describes only one configuration of the telescope. Changes in mass and stiffness distribution due to e.g. tracking are not covered within one model. A possible solution is the analysis of typical and worst case configurations to estimate the characteristics of intermediate configurations.

**Viscous damping** In telescope structures the modal damping values are in general small ( $\zeta < 5\%$ , conservative assumption for modeling  $\zeta = 0.75..1\%$ ) and hence

the exact mechanism and distribution of damping is not important, but can be approximated by a viscous (=velocity proportional) symmetric damping.

**Passivity** The system matrices must be not-negative definite. Therefore no self-excited vibration is allowed like flutter effects, and the corresponding undamped system is a conservative system. Neglecting gyroscopic effects is possible since the rotation for tracking is very slow for telescope systems.

The equation of motion can be set up in different ways, e.g. for simplified structures with the method of Ritz or Galerkin (see [28]). For typical telescopes the mechanical structure is modeled with finite elements (FE) and the software generates remotely the equation of motion.

### 3.1.1 Finite element modeling

Finite element modeling is the most powerful tool to analyze the mechanical properties of telescope systems. Depending on the level of accuracy and the subject of research very rough models with point masses, bars and beams or detailed models with shell and volume elements can be built, which allow a better geometric approximation and more realistic distributions of stresses over the structure. The structure of the resulting equations is not changing with the level of detail, only the number of degrees of freedom (DOFs) is varying.

For a static analysis the resulting linear equation system reads:

$$\mathbf{K}\mathbf{x} = \mathbf{f} \tag{3.1}$$

with the stiffness matrix  $\mathbf{K}$ , the vector of generalized displacements  $\mathbf{x}$  and the external generalized forces  $\mathbf{f}$ . For large telescope structures the detailed FE models have typically some hundred thousands of DOFs. In the FE software algorithms are included which are specially optimized for solving this equation system. Directly exporting the stiffness matrix to solve it for an external simulation does not make sense in general. The static load should be split into a set of basic cases to be solved within the FE software. Only the relevant results (e.g. displacements of the mirrors) should be exported and superposing these the general outputs in the simulation should be computed.

For dynamic simulations the equation of motion for an elastic mechanical structure fulfilling the assumptions above in an absolute coordinate system reads:

$$\mathbf{M}\ddot{\mathbf{x}} + \mathbf{D}\dot{\mathbf{x}} + \mathbf{K}\mathbf{x} = \mathbf{f}, \text{ with} \tag{3.2}$$

- $\mathbf{x}$  vector of generalized displacements in an absolute coordinate system
- $\mathbf{f}$  vector of generalized forces
- $\mathbf{M}$  symmetric mass matrix
- $\mathbf{D}$  symmetric damping matrix
- $\mathbf{K}$  symmetric stiffness matrix.

The mass, damping and stiffness matrices are all semi-positive definite symmetric matrices and if the structure is fully supported, the stiffness matrix is positive definite.

This system of linear differential equations can be solved in different ways. The most general approach is the direct integration in the time domain, as this allows also geometric or other non-linearities (the matrices are changing depending on the displacement). However, the solution requires high computational effort and represents only one time-history for the input load.

For linear systems with constant matrices the harmonic response gives a result with more general meaning. By assuming both the inputs force  $\mathbf{f} = \Re(\mathbf{f}_0 e^{j\omega t})$  and the response  $\mathbf{x} = \Re(\mathbf{x}_0 e^{j\omega t})$  as a sinusoidal function with the (complex) amplitudes  $\mathbf{f}_0$  respectively  $\mathbf{x}_0$ , equation (3.2) can be evaluated as a simple linear equation system with a complex dynamic stiffness matrix  $\tilde{\mathbf{K}} = -\mathbf{M}\omega^2 + j\omega\mathbf{D} + \mathbf{K}$  for each frequency point.

A more efficient method is the transformation of equation (3.2) into the modal space and the modal superposition for the frequency response and time response: The natural frequencies  $\omega_i$ , the modal damping  $\zeta_i$  and the mode shapes of the free vibration  $\{\phi_i\}$  are computed from the homogeneous equation  $[\mathbf{M}]\{\ddot{\mathbf{x}}\} + [\mathbf{D}]\{\dot{\mathbf{x}}\} + [\mathbf{K}]\{\mathbf{x}\} = \mathbf{0}$  assuming  $\mathbf{x} = \Re(\mathbf{x}_0 e^{j\omega t})$ . Expressing the displacement  $\mathbf{x}$  in terms of the mode shapes  $\{\phi_i\}$  as  $\{\mathbf{x}\} = [\phi]\{\mathbf{q}\}$  results in the transformed equations:

$$\{\ddot{\mathbf{q}}\} + [diag(2\zeta_i\omega_i)]\{\dot{\mathbf{q}}\} + [diag(\omega_i^2)]\{\mathbf{q}\} = [\phi]^T\{\mathbf{f}\} \quad (3.3)$$

with the normalization  $[\phi]^T[\mathbf{M}][\phi] = [\mathbf{I}]$  and  $[\phi]^T[\mathbf{K}][\phi] = [diag(\omega_i^2)]$ ,  $[\phi]^T[\mathbf{D}][\phi] = [diag(2\zeta_i\omega_i)]$ .<sup>1</sup>

In general a much smaller number  $m$  of modes yields a very good approximation of the dynamics of the complete structure with many more DOFs  $n$ .

For time-dependent simulation it is a standard to describe the dynamics of a system in state space format with the state equation  $\dot{\mathbf{z}} = \mathbf{A}\mathbf{z} + \mathbf{B}\mathbf{u}$  and the output equation  $\mathbf{y} = \mathbf{C}\mathbf{z} + \mathbf{D}\mathbf{u}$ . A state space realization with a force distribution  $\{\mathbf{f}(t)\} = [\mathbf{P}_L]\{\mathbf{u}(t)\}$

<sup>1</sup>The structure of the damping matrix  $\mathbf{D}$  requires some constraints to allow the diagonalization with  $[\phi]^T[\mathbf{D}][\phi]$ . For lightly damped structures this is not relevant. A possible realization of  $\mathbf{D}$  is e.g.  $\mathbf{D} = \alpha\mathbf{M} + \beta\mathbf{K}$  with the modal damping for mode  $i$   $\zeta_i = \frac{\alpha}{2\omega_i} + \frac{\beta\omega_i}{2}$

and relevant outputs (e.g. sensor outputs) as a linear combination of the nodal displacements  $\{\mathbf{y}(t)\} = [\mathbf{P}_{S_x}]^T \{\mathbf{x}(t)\} + [\mathbf{P}_{S_x}]^T \{\dot{\mathbf{x}}(t)\}$  for the modal equation of motion (3.3) is:

$$\frac{d}{dt} \begin{Bmatrix} \mathbf{q} \\ \dot{\mathbf{q}} \end{Bmatrix} = \begin{bmatrix} [\mathbf{0}] & [\mathbf{I}] \\ -[\text{diag}(\omega_i^2)] & -[\text{diag}(2\zeta_i\omega_i)] \end{bmatrix} \begin{Bmatrix} \mathbf{q} \\ \dot{\mathbf{q}} \end{Bmatrix} + \begin{bmatrix} [\mathbf{0}] \\ [\phi]^T [\mathbf{P}_L] \end{bmatrix} \{\mathbf{u}\}; \quad (3.4)$$

$$\mathbf{y} = [[\mathbf{P}_{S_x}^T][\phi], [\mathbf{P}_{S_x}^T][\phi]] \begin{Bmatrix} \mathbf{q} \\ \dot{\mathbf{q}} \end{Bmatrix} + [\mathbf{0}] \quad \begin{array}{l} \text{(if } y = \text{displacement} \\ \text{of all DOFs} \\ \text{then } [\mathbf{P}_{S_x}]^T = [\mathbf{I}]) \end{array} \quad (3.5)$$

Instead of this realization the following one is recommended, as the  $\mathbf{A}$ -matrix consists of Jordan blocks resulting in a band structure and it is avoided to have numbers of order 1 and of order  $\omega^2$  inside this matrix:

$$\frac{d}{dt} \begin{Bmatrix} \vdots \\ \omega_i q_i \\ \dot{q}_i \\ \vdots \end{Bmatrix} = \begin{bmatrix} \cdots & [\mathbf{0}] \\ & [\mathbf{A}_i] & \cdots \\ [\mathbf{0}] & & \cdots \end{bmatrix} \begin{Bmatrix} \vdots \\ \omega_i q_i \\ \dot{q}_i \\ \vdots \end{Bmatrix} + \begin{bmatrix} \vdots \\ \mathbf{B}_i \\ \vdots \end{bmatrix} \{\mathbf{u}\}, \quad (3.6)$$

$$\{\mathbf{y}\} = \begin{bmatrix} \cdots & \mathbf{C}_i & \cdots \end{bmatrix} \begin{Bmatrix} \vdots \\ \omega_i q_i \\ \dot{q}_i \\ \vdots \end{Bmatrix} + [\mathbf{D}] \{\mathbf{u}\}$$

with:

$$\mathbf{A}_i = \begin{bmatrix} 0 & \omega_i \\ -\omega_i & -2\zeta_i\omega_i \end{bmatrix}; \quad \mathbf{B}_i = \begin{bmatrix} [\mathbf{0}] \\ [\phi_i]^T [\mathbf{P}_L] \end{bmatrix}; \quad \mathbf{C}_i = \begin{bmatrix} [\mathbf{P}_{S_x}]^T [\phi_i] / \omega_i & \mathbf{P}_{S_x} [\phi_i] \end{bmatrix}$$

$$\begin{array}{l}
 \left. \begin{array}{l} \{\mathbf{q}\} \\ \{\dot{\mathbf{q}}\} \end{array} \right\} \text{ respectively } \left. \begin{array}{l} \vdots \\ \left\{ \begin{array}{l} \omega_i q_i \\ \dot{q}_i \end{array} \right\} \\ \vdots \end{array} \right\} \quad 2m \times 1 \quad \text{state vector for } 2m \text{ states and } m \text{ modes} \\
 \mathbf{y} \quad k \times 1 \quad \text{output vector with } k \text{ outputs} \\
 \mathbf{u} \quad l \times 1 \quad \text{input vector with } l \text{ inputs} \\
 \mathbf{A} \quad 2m \times 2m \quad \text{system matrix} \\
 \mathbf{B} \quad 2m \times l \quad \text{control matrix} \\
 \mathbf{C} \quad k \times 2m \quad \text{observation matrix} \\
 \mathbf{D} \quad k \times l \quad \text{feedthrough matrix} \\
 \phi \quad n \times m \quad \text{matrix of } m \text{ mode shapes for } n \text{ DOFs} \\
 \mathbf{P}_L \quad n \times l \quad P - \text{matrix for load sets} \\
 \mathbf{P}_S \quad n \times k \quad P - \text{matrix for relevant output DOFs}
 \end{array}$$

### 3.1.2 Handling disturbance inputs from wind and ground

Different kinds of disturbances and loads can excite vibrations on a telescope structure like wind load, seismic excitation or actuator forces. In general the loads can be split into the two groups displacements (respectively velocities or accelerations) and forces.

The forces like wind loads can directly be applied to the state-space equation (3.4). However, for the displacement input the equation system (3.2) must be restructured.

In the equation of motion (3.2) the DOFs are partitioned into two groups  $\{\mathbf{x}\} = \{\{\mathbf{x}_1\}^T, \{\mathbf{x}_2\}^T\}^T$ , with  $\{\mathbf{x}_1\}$  being the DOFs with unknown displacement and  $\{\mathbf{x}_2\}$  being those with known displacement. Thus equation (3.2) becomes to:

$$\begin{bmatrix} [\mathbf{M}_{11}] & [\mathbf{M}_{12}] \\ [\mathbf{M}_{21}] & [\mathbf{M}_{22}] \end{bmatrix} \begin{Bmatrix} \ddot{\mathbf{x}}_1 \\ \ddot{\mathbf{x}}_2 \end{Bmatrix} + \begin{bmatrix} [\mathbf{D}_{11}] & [\mathbf{D}_{12}] \\ [\mathbf{D}_{21}] & [\mathbf{D}_{22}] \end{bmatrix} \begin{Bmatrix} \dot{\mathbf{x}}_1 \\ \dot{\mathbf{x}}_2 \end{Bmatrix} + \begin{bmatrix} [\mathbf{K}_{11}] & [\mathbf{K}_{12}] \\ [\mathbf{K}_{21}] & [\mathbf{K}_{22}] \end{bmatrix} \begin{Bmatrix} \mathbf{x}_1 \\ \mathbf{x}_2 \end{Bmatrix} = \begin{Bmatrix} \mathbf{f}_1 \\ \mathbf{f}_2 \end{Bmatrix} \quad (3.7)$$

In equation (3.7) the displacements, velocities and accelerations corresponding to  $\{\mathbf{x}_2\}$  are known. So the first row of the equation is:

$$\begin{bmatrix} [\mathbf{M}_{11}] & [\mathbf{M}_{12}] \end{bmatrix} \begin{Bmatrix} \{\ddot{\mathbf{x}}_1\} \\ \{\ddot{\mathbf{x}}_2\} \end{Bmatrix} + \begin{bmatrix} [\mathbf{D}_{11}] & [\mathbf{D}_{12}] \end{bmatrix} \begin{Bmatrix} \{\dot{\mathbf{x}}_1\} \\ \{\dot{\mathbf{x}}_2\} \end{Bmatrix} + \begin{bmatrix} [\mathbf{K}_{11}] & [\mathbf{K}_{12}] \end{bmatrix} \begin{Bmatrix} \{\mathbf{x}_1\} \\ \{\mathbf{x}_2\} \end{Bmatrix} = \{\mathbf{f}_1\} \quad (3.8)$$

$$[\mathbf{M}_{11}]\{\ddot{\mathbf{x}}_1\} + [\mathbf{D}_{11}]\{\dot{\mathbf{x}}_1\} + [\mathbf{K}_{11}]\{\mathbf{x}_1\} = \{\mathbf{f}_1\} - [\mathbf{M}_{12}]\{\ddot{\mathbf{x}}_2\} - [\mathbf{D}_{12}]\{\dot{\mathbf{x}}_2\} - [\mathbf{K}_{12}]\{\mathbf{x}_2\} \quad (3.9)$$

The left side of this equation can simply be treated in modal coordinates with the same modal data as the fully supported structure ( $\ddot{\mathbf{x}}_2 = \dot{\mathbf{x}}_2 = \mathbf{x}_2 = \mathbf{0}$ ). The inputs  $x_2$ ,  $\dot{x}_2$  and  $\ddot{x}_2$  are all depending on each other by derivatives respectively integrals. Therefore only the acceleration is used as input and the velocity and displacement is calculated with two extra states within the state space system.

Equation (3.9) is very general, as it allows an arbitrary distribution of forces and displacements on all DOFs of the structure. However, the matrices  $\mathbf{M}_{12}$ ,  $\mathbf{D}_{12}$  and  $\mathbf{K}_{12}$  must be exported from the FE model.

In the special case of base-excitation due to seismic motion all ground fixed DOFs approximately have the same displacements while the rotations are zero. The absolute displacement of all nodes can be split into the displacement of the base and an (elastic) relative displacement. <sup>2</sup>:

$$\{\mathbf{x}\}_{abs} = \{\mathbf{x}\}_{rel} + \{\mathbf{x}\}_b \quad (3.10)$$

$$\{\mathbf{x}_b\} = \begin{bmatrix} \{\mathbf{x}_b\}_1^T, \{\mathbf{x}_b\}_2^T, \{\mathbf{x}_b\}_3^T, \dots \end{bmatrix}^T = \mathbf{E}_{cb}\{\mathbf{x}_b\}_1 \quad (3.11)$$

$$\{\mathbf{x}_b\}_i = \begin{bmatrix} x_{bx}, x_{by}, x_{bz}, 0, 0, 0 \end{bmatrix}^T \quad (3.12)$$

Since the rigid body motion of an unsupported structure causes no direct elastic forces and damping ( $[\mathbf{K}]\{\mathbf{x}\}_r = [\mathbf{D}]\{\dot{\mathbf{x}}\}_r = \mathbf{0}$ ) using  $\mathbf{x}_1 = \mathbf{x}_{rel1} + \mathbf{x}_{b1}$  and  $\mathbf{x}_2 = \mathbf{x}_{b2}$  the equation of motion (3.7) can be written as:

$$[\mathbf{M}_{11}, \mathbf{M}_{12}] \begin{Bmatrix} \{\ddot{\mathbf{x}}_{rel1}\} \\ \mathbf{0} \end{Bmatrix} + \begin{Bmatrix} \{\ddot{\mathbf{x}}_{b1}\} \\ \{\ddot{\mathbf{x}}_{b2}\} \end{Bmatrix} + [\mathbf{D}_{11}] \{\dot{\mathbf{x}}_{rel1}\} + [\mathbf{K}_{11}] \{\mathbf{x}_{rel1}\} = \{\mathbf{f}_1\} \quad (3.13)$$

$$[\mathbf{M}_{11}] \{\ddot{\mathbf{x}}_{rel1}\} + [\mathbf{D}_{11}] \{\dot{\mathbf{x}}_{rel1}\} + [\mathbf{K}_{11}] \{\mathbf{x}_{rel1}\} = \{\mathbf{f}_1\} - \begin{bmatrix} [\mathbf{M}_{11}] & [\mathbf{M}_{12}] \end{bmatrix} [\mathbf{E}_{xb}] \{\ddot{\mathbf{x}}_b\}_1 \quad (3.14)$$

<sup>2</sup>The same is valid for rotations, but coupling terms have to be taken into account and therefore this will not be used here.



$$\{\mathbf{x}\}_{abs} = \{\mathbf{x}\}_{rel} + \{\mathbf{x}\}_b \quad (3.15)$$

The state-space form of the system including rigid body modes  $r$  and flexible modes  $f$ , force and base acceleration ( $u_f$  respectively  $u_b$ ) as well as displacement and velocity output reads:

$$\frac{d}{dt} \begin{Bmatrix} \mathbf{q}_r \\ \dot{\mathbf{q}}_r \\ \Omega_{if}\mathbf{q}_f \\ \dot{\mathbf{q}}_f \\ \mathbf{v}_b \\ \dot{\mathbf{v}}_b \end{Bmatrix} = \begin{bmatrix} [\mathbf{0}] & [\mathbf{I}] & [\mathbf{0}] & [\mathbf{0}] & [\mathbf{0}] & [\mathbf{0}] \\ [\mathbf{0}] & [\mathbf{0}] & [\mathbf{0}] & [\mathbf{0}] & [\mathbf{0}] & [\mathbf{0}] \\ [\mathbf{0}] & [\mathbf{0}] & [\mathbf{0}] & [\Omega_{if}] & [\mathbf{0}] & [\mathbf{0}] \\ [\mathbf{0}] & [\mathbf{0}] & [-\Omega_{if}] & [-\Omega_{if}\zeta_{if}] & [\mathbf{0}] & [\mathbf{0}] \\ [\mathbf{0}] & [\mathbf{0}] & [\mathbf{0}] & [\mathbf{0}] & [\mathbf{0}] & [\mathbf{I}] \\ [\mathbf{0}] & [\mathbf{0}] & [\mathbf{0}] & [\mathbf{0}] & [\mathbf{0}] & [\mathbf{0}] \end{bmatrix} \begin{Bmatrix} \mathbf{q}_r \\ \dot{\mathbf{q}}_r \\ \Omega_{if}\mathbf{q}_f \\ \dot{\mathbf{q}}_f \\ \mathbf{v}_b \\ \dot{\mathbf{v}}_b \end{Bmatrix} + \begin{bmatrix} [\mathbf{0}] & [\mathbf{0}] \\ [\phi_r]^T[\mathbf{P}_L] & [\phi_r]^T[\tilde{\mathbf{P}}_B] \\ [\mathbf{0}] & [\mathbf{0}] \\ [\phi_f]^T[\mathbf{P}_L] & [\phi_f]^T[\tilde{\mathbf{P}}_B] \\ [\mathbf{0}] & [\mathbf{0}] \\ [\mathbf{0}] & [\mathbf{I}] \end{bmatrix} \begin{Bmatrix} \mathbf{u}_f \\ \mathbf{u}_b \end{Bmatrix} \quad (3.16)$$

$$\mathbf{y} = \begin{bmatrix} [\phi_r]^T[\mathbf{P}_{S_x}] \\ [\phi_r]^T[\mathbf{P}_{S_{\dot{x}}}] \\ [1/\omega_{if}][\phi_f]^T[\mathbf{P}_{S_x}] \\ [\phi_f]^T[\mathbf{P}_{S_{\dot{x}}}] \\ [\mathbf{E}_{xb}]^T[\mathbf{P}_{S_x}] \\ [\mathbf{E}_{xb}]^T[\mathbf{P}_{S_{\dot{x}}}] \end{bmatrix}^T \begin{Bmatrix} \mathbf{q}_r \\ \dot{\mathbf{q}}_r \\ \omega_{if}\mathbf{q}_f \\ \dot{\mathbf{q}}_f \\ \mathbf{v}_b \\ \dot{\mathbf{v}}_b \end{Bmatrix} + [\mathbf{0}, \mathbf{0}] \begin{Bmatrix} \mathbf{u}_f \\ \mathbf{u}_b \end{Bmatrix}; \quad (3.17)$$

with  $\Omega_{if} = \text{diag}(\omega_{if})$ ,  $\Omega_{if}\zeta_{if} = \text{diag}(\omega_{if}\zeta_{if})$  and  $\tilde{\mathbf{P}}_B = [\mathbf{M}_{11}\mathbf{M}_{12}]\mathbf{E}_{xb}$ .

Only one input is necessary for each set of base excitation. This is transformed by a matrix  $\mathbf{E}_{xb}$  to all DOFs of the FE model. Analogously to equation (3.6) the system can also be built of blocks for each mode improving the band structure of the system matrix.

### 3.1.3 Including actuators into a model

Actuators inside systems always create a pair of forces acting in opposite directions. Dependent on the control algorithm and the actuator type, it can be decided between a force and a displacement control. If the force is controlled, the open loop actuator force must be independent of the displacements inside the structure. Considering an actuator, which is connected with two points to the structure, one connection has to be open for the open loop model. If the displacement is controlled, the open loop force applied to the actuator is depending on the displacements of the structure, since compressing the actuator causes a force proportional to the actuator stiffness. Therefore, the open loop model needs the full connection of the actuator to include its stiffness.

An example for the later are piezo-electric ceramic patches glued onto a mirror for shape control. If the controller sends a certain voltage command to the patch, strains and stresses inside the piezo are created in the very same way as due to thermal expansions. The actuator force, which is really transmitted from the patch to the mirror, is depending on both the applied voltage and the strain:  $F_{Piezoactuator} = c_1 U + c_2 \varepsilon$ . (see also [29])

An example for a force control are the bogie drives of OWL. The altitude bogies move on rails which are fixed to the elastic structure. In the model the lateral and normal stiffness terms of the bogies are included, while the direction along the rails is free. Hence, the flexibilities of rails, the support structure and the actuators are included and realistic displacements of the wheels can be computed, which in turn are required for the friction models. Closing the control loop removes the rigid body mode for the altitude rotation calculated in the modal analysis.

### 3.1.4 Best-fit outputs for rigid body motions of the mirrors

A required output of the mechanical model is the displacement and deformation of each mirror to be used as input of an optical model. Depending on the model the mirrors are assumed to be rigid in the optical model (i.e. they keep their geometrical shape and only rigid body motions are possible) or also elastic deformations of the mirrors are included. In the simplified assumption of rigid mirrors, the mechanical model must deliver the translations and rotations of the whole reflector. If the reflector is modeled as an elastic body within the FE-model, the rigid body motions can be computed only in a best-fit sense. Allowing also deformations of the geometric shape of the mirrors, it makes sense to compute the elastic deformations in terms of Zernike polynomials relative to the new rotated and translated vertex position.

Applying a linear optical model, this can be represented for six rigid body motions per mirror and  $m$  Zernike polynomials by the equation:

$$\delta OM = \mathbf{M}_{opt} * \mathbf{p}; \quad N \text{ optical surfaces (mirrors)} \quad (3.18)$$

with  $\mathbf{p} = [\delta x_1, \delta y_1, \delta z_1, \delta \theta_{x1}, \delta \theta_{y1}, \delta \theta_{z1}, \delta a_{1,1}, \dots, \delta a_{m,1}, \dots, \delta x_N, \dots, \delta a_{m,N}]^T$

$\delta OM$	resulting small variation of an optical quantity
$\mathbf{M}_{opt}$	linear optical sensitivity matrix
$\mathbf{p}$	3 displacements, 3 rotations and $m$ coefficients for the Zernike polynomials $Z_1 \dots Z_m$ for each of the $N$ optical surfaces
$x, y, z, \theta_x, \theta_y, \theta_z$	6 DOFs of a rigid body mirror
$a_{i,k}$	Zernike coefficient belonging to Zernike polynomial $i$ and optical surface $k$
<i>indices</i> 1.. $N$	number of the mirror
<i>indices</i> 1.. $m$	number of the Zernike polynomial

The output equation of the statespace model  $\dot{\mathbf{z}} = \mathbf{A}\mathbf{z} + \mathbf{B}\mathbf{u}$ ,  $\mathbf{y} = \mathbf{C}\mathbf{z} + \mathbf{D}\mathbf{u}$  yields the vector  $\mathbf{p}$ . This is not directly possible, if the mirror is an elastic component within the structural model. Therefore  $\mathbf{C}$  and  $\mathbf{D}$  must be created accordingly.

To build the state space model, a matrix  $\mathbf{P}_{optics}$  must be defined, which builds outputs from the generalized positions  $\mathbf{z}$  of the nodes [1.. $n$ ] with the DOFs  $x_i, y_i, z_i, \theta_{xi}, \theta_{yi}, \theta_{zi}$  of the FE-structure:

$$\mathbf{p} = \mathbf{y} = [\mathbf{P}_{optics}]^T \mathbf{z} \quad \text{with } \mathbf{z} = \left\{ x_1, y_1, \dots, x_i, \dots, \theta_{zn} \right\}^T \quad (3.19)$$

In this section only a matrix  $\mathbf{P}_{rigid}$  is derived, which delivers the best-fit rigid body motion of the mirror. The figure 3.1 shows a rigid mirror in the initial position and after a displacement and rotation. There are two coordinate systems. The inertial fixed one is called I-system and has the point O as point of origin, the body fixed one is called M-system, is fixed to the mirror, has the vertex V of the mirror as its origin and is (here in the figure) initially aligned to the I-system<sup>3</sup>. As an example, a point P on the mirror surface is regarded. After displacement all points of the mirror are signed with a ' (e.g.:  $P \rightarrow P'$ ).

The position of the point P on the undeformed structure is:

$$\mathbf{r}_{OP} = \mathbf{r}_{OV} + \mathbf{r}_{VP} \quad (3.20)$$

After the translation of the vertex V by  $\mathbf{r}_{VV'}$  and rotation by  $\theta$  the position of P is ( $P \rightarrow P'$ ):

$$\mathbf{r}_{OP'} = \mathbf{r}_{OV} + \mathbf{r}_{VV'} + \mathbf{r}_{V'P'} \quad (3.21)$$

<sup>3</sup>In general the mirror co-ordinate system is not aligned with the global co-ordinate system. In figure 3.1 the I-system and the M-system are only aligned for simplicity.

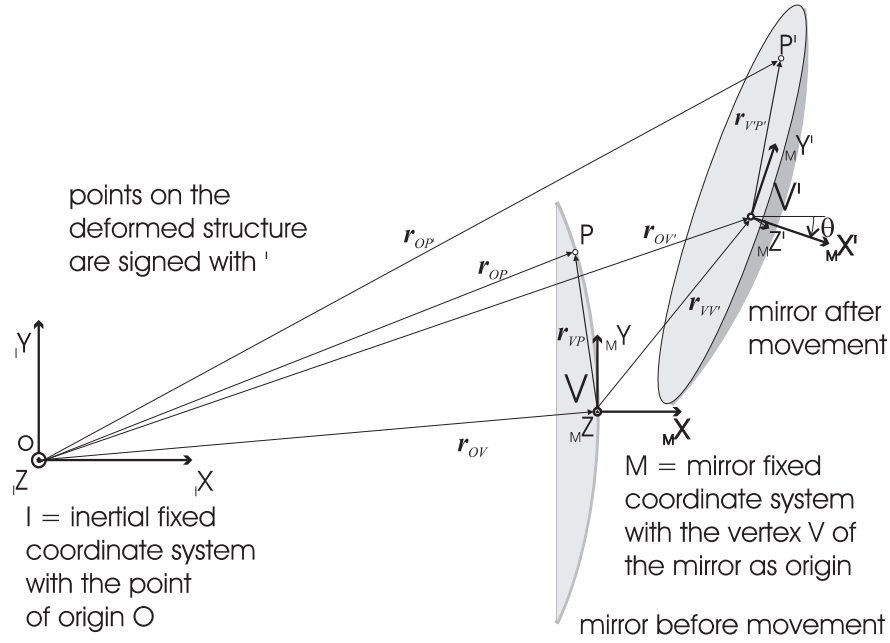


Figure 3.1: Coordinate systems and notations

For small angles  $\theta$  the displacement of point P is (see also Appendix E)

$${}_I \mathbf{r}_{PP'} = {}_I \mathbf{r}_{VV'} - {}_I \mathbf{r}_{VP} \times \theta \quad (3.22)$$

In the vector equation (3.22) the two vectors  ${}_I \mathbf{r}_{VV'}$  and  $\theta$  are unknowns, whereas the translation  ${}_I \mathbf{r}_{PP'}$  of the point P (nodal displacement as result of the FE-model) and the vector  ${}_I \mathbf{r}_{VP}$  (geometry only) are known. This yields three equations for each point  $P_i$  (three cartesian co-ordinates) and 6 unknowns altogether. However, the points  $P_i$  on the mirror are not independent, because of the fixed geometry of the mirror. That is the reason, why a first point gives three equations, the second one two only (the distance to the first point is fixed: one constraint equation), the third one only one further equation (fixed distance to two points: two constraints) and each further point no further equation (fixed distance to three points and herewith to all other points: three constraints). The equation system can therefore be solved with three points, which are not collinear (three points define a plane in the 3-d space).

In practical the motion of the points is not only due to the rigid body motion of the mirror, but also caused by an elastic deformation. Therefore the equation system can no more be solved exactly for three points and so more than three points on the mirror should be used and an averaged value should be computed for the displacement.

To handle more than one point parallel, equation (3.22) is transformed into a matrix notation for point  $P_i$ :

$$\{I\mathbf{r}_{PP'}\}_i = \left[ \mathbf{I} \mid [-\tilde{\mathbf{R}}]_i \right] \begin{Bmatrix} \{I\mathbf{r}_{VV'}\} \\ \{\theta\} \end{Bmatrix} \quad (3.23)$$

with the matrix  $[\tilde{\mathbf{R}}]_i$  being an operator building the cross product:

$$[\tilde{\mathbf{R}}]_i = \begin{bmatrix} 0 & -Iz_{VP,i} & Iy_{VP,i} \\ Iz_{VP,i} & 0 & -Ix_{VP,i} \\ -Iy_{VP,i} & Ix_{VP,i} & 0 \end{bmatrix} \quad (3.24)$$

For  $N$  points  $P_1, \dots, P_N$  this gives the equation system:

$$\underbrace{\begin{Bmatrix} \{I\mathbf{r}_{PP'}\}_1 \\ \vdots \\ \{I\mathbf{r}_{PP'}\}_N \end{Bmatrix}}_{3N \times 1} = \underbrace{\begin{bmatrix} \mathbf{I} & [-\tilde{\mathbf{R}}]_1 \\ \vdots & \vdots \\ \mathbf{I} & [-\tilde{\mathbf{R}}]_N \end{bmatrix}}_{3N \times 6} \underbrace{\begin{Bmatrix} \{I\mathbf{r}_{VV'}\} \\ \{\theta\} \end{Bmatrix}}_{6 \times 1} \quad (3.25)$$

which is an overdetermined linear equation system (for  $N > 2$ ) of form  $\{\mathbf{b}\}_{3N \times 1} = [\mathbf{A}]_{3N \times 6} \{\mathbf{x}\}_{6 \times 1}$ . The solution with the least mean square error can be derived by:

$$\begin{aligned} [\mathbf{A}\mathbf{x} - \mathbf{b}]^T [\mathbf{A}\mathbf{x} - \mathbf{b}] &= \min! \\ \Rightarrow \mathbf{x} &= (\mathbf{A}^T \mathbf{A})^{-1} \mathbf{A}^T \mathbf{b} = \mathbf{A}^+ \mathbf{b} \end{aligned}$$

with  $\mathbf{A}^+$  being the pseudoinverse of  $\mathbf{A}$ .

However, this procedure is only valid, if all equations in the system have the same relevancy, i.e. each point represents a structural part of an equal size. Otherwise each row  $i$  in the equation system (3.25) should be multiplied by a weighting factor  $S_i$  ( $S_i = \sqrt{A_i}$ : square root of mirror surface represented by the node  $i$ ):

$$S_i \{I\mathbf{r}_{PP'}\}_i = S_i \left[ \mathbf{I} \mid [-\tilde{\mathbf{R}}]_i \right] \begin{Bmatrix} \{I\mathbf{r}_{VV'}\} \\ \{\theta\} \end{Bmatrix} \quad (3.26)$$

and with the vector

$$\mathbf{S} = \underbrace{\{S_1, S_1, S_1, S_2, S_2, \dots, S_i, \dots, S_M, S_M, S_M\}}_3^T:$$

$$\underbrace{\begin{Bmatrix} \{I\mathbf{r}_{vv'}\} \\ \{\theta\} \end{Bmatrix}}_{6 \times 1} = \underbrace{\begin{bmatrix} \mathbf{I} & [-\tilde{\mathbf{R}}]_1 \\ \vdots & \vdots \\ \mathbf{I} & [-\tilde{\mathbf{R}}]_M \end{bmatrix}}_{3M \times 6}^+ \underbrace{\begin{Bmatrix} \{I\mathbf{r}_{PP'}\}_1 \\ \vdots \\ \{I\mathbf{r}_{PP'}\}_M \end{Bmatrix}}_{3M \times 1} \stackrel{!}{=} [\mathbf{P}_{rigid}]^T \{\mathbf{z}\} \quad (3.27)$$

The vector  $\{I\mathbf{r}_{PP'}\}_i$  can be derived from the state vector  $\{\mathbf{z}\}$  of the state-space model. Therefore, a mapping matrix  $E$  needs to be created to deliver the states of the required DOF in the right order:

$$\{I\mathbf{r}_{PP'}\}_i = [\mathbf{E}]\{\mathbf{z}\} \quad (3.28)$$

Finally the total matrix  $\mathbf{P}_{\text{rigid}}$  from equation (3.19) is built by the equation

$$[\mathbf{P}_{\text{rigid}}] = \left[ \left[ \begin{array}{cc} \mathbf{I} & [-\tilde{\mathbf{R}}]_1 \\ \vdots & \vdots \\ \mathbf{I} & [-\tilde{\mathbf{R}}]_M \end{array} \right] \right]^+ \text{diag}(\mathbf{S}) [\mathbf{E}]^T \quad (3.29)$$

### 3.1.5 Elastic mirror deformation in terms of Zernike modes

If the optical model also includes elastic mirror deformations, a matrix  $P_{Zernike}$  is built, which expresses the elastic deformations normal to the nominal shape in Zernike polynomials. These polynomials are defined on a unit circle centered on the mirror vertex. Both the mirror vertex  $\mathbf{r}_{OV}$  with a mirror coordinate system  $M$  (see figure 3.1) and the aperture radius for the normalization of coordinates must be known. The location of the FE-nodes in the M-system can be calculated with the appropriate coordinate transformation from the nodal positions in the global coordinate system:

$${}_M\mathbf{r}_{VP} = {}_M\mathbf{A}_{MI}({}_I\mathbf{r}_{OP} - {}_I\mathbf{r}_{OV}) \quad (3.30)$$

Using these relative coordinates allows to compute a Zernike matrix  $\psi(i, k)$  for all polynomials  $k$  ( $k = 1..m$ ) in the FE-nodes located in points  $P_i(x_i, y_i)$  ( $i = 1..n$ )

$$\psi(i, k) = \psi_k({}_Mx_i, {}_My_i) \quad (3.31)$$

The pseudoinverse of the matrix  $\psi(i, k)$  is required for the least square coefficients <sup>4</sup>

$$\psi^+(i, k) = [\psi^T(i, k)\psi(i, k)]^{-1}\psi^T(i, k) \quad (3.32)$$

For the computation of the deformation perpendicular to the mirror surface using the mirror normal vector in the vertex  ${}_M\mathbf{n}_V^0 = {}_M[0, 0, 1]^T$  is sufficient for slightly bended surfaces. Mirrors with larger curvature require for each surface FE node an individual normal vector  $\mathbf{n}_i^0$  (normalized to unit length).

While the simulation, in each time step the residual deformation vector  $\mathbf{d}_i$  for each point  $P_i$  due to elastic deformations must be computed by subtracting the rigid body

<sup>4</sup>If necessary a weighting according to the square root of the represented mirror area (analog to (3.28)) can be included. Instead of  $\mathbf{A} \rightsquigarrow \mathbf{A}^+$  the weighting vector  $\mathbf{S}$  is used:

$$\mathbf{A} \rightsquigarrow [[\text{diag}(\mathbf{S})\mathbf{A}]^+ \text{diag}(\mathbf{S})]$$

displacements from the total displacements. In mirror coordinates  $M$  according to equation (3.22) (assuming no changes in  ${}_M\mathbf{A}_{MI}$  due to small angles  $\theta$ ) this vector  $\mathbf{d}_i$  reads:

$${}_M\mathbf{d}_i = {}_M\mathbf{A}_{MI}({}_I\mathbf{r}_{PP'} - ({}_I\mathbf{r}_{VV'} - {}_I\mathbf{r}_{VP} \times \theta)) \quad (3.33)$$

The normal distance  $d_{\perp,i}$  results to  $d_{\perp,i} = {}_M\mathbf{d}_i^T {}_M\mathbf{n}_i^0$  respectively  $d_{\perp,i} = {}_M\mathbf{d}_i^T {}_M\mathbf{n}_i^0$  with normalized normal vectors  ${}_M\mathbf{n}_i^0$  and positive values for deformation in the direction of the normal vector. The best-fit Zernike coefficients  $\zeta = \{\zeta_k\}$  can be calculated with the pseudo inverse  $\psi^+(i, k)$  from the normal distances for each point to  $\zeta = \psi^+(i, k)\mathbf{d}_{\perp,i}$ .

This procedure results in the following equations for  $\zeta$  of one mirror:

$$\begin{aligned} \zeta &= [\psi^+(i, k)]\{\mathbf{d}_{\perp,i}\} \\ &= [\psi^+(i, k)][blkdiag(\{{}_M\mathbf{n}_i^0\}^T)]\{{}_M\mathbf{d}_i\} \\ &= [\psi^+(i, k)][blkdiag(\{{}_M\mathbf{n}_i^0\}^T {}_M\mathbf{A}_{MI})] \left\{ \begin{array}{c} \vdots \\ \{{}_I\mathbf{r}_{P_i P'_i}\} - ({}_I\mathbf{r}_{VV'} - {}_I\mathbf{r}_{VP_i} \times \theta) \\ \vdots \end{array} \right\} \\ &= \underbrace{[\psi^+(i, k)]}_{[m \times n]} \underbrace{blkdiag(\{{}_M\mathbf{n}_i^0\}^T {}_M\mathbf{A}_{MI})}_{[n \times 3n]} \underbrace{\left( \mathbf{E} - \begin{bmatrix} [\mathbf{I}] & [-\tilde{\mathbf{R}}]_1 \\ \vdots & \vdots \\ [\mathbf{I}] & [-\tilde{\mathbf{R}}]_M \end{bmatrix} \mathbf{P}_{rigid}^T \right)}_{[3n \times n \text{ DOFs}]} \underbrace{\{\mathbf{z}\}}_{[n \text{ DOFs} \times 1]} \\ &\stackrel{!}{=} [\mathbf{P}_{Zernike}]^T \{\mathbf{z}\} \end{aligned} \quad (3.34)$$

$blkdiag(\{{}_M\mathbf{n}_i^0\}^T)$  means here the blockdiagonal matrix with the transposed normal vectors  $\{{}_M\mathbf{n}_i^0\}^T$  as matrix blocks.

Thus the required matrix  $\mathbf{P}_{Zernike}$  is finally

$$[\mathbf{P}_{Zernike}]^T = [\psi^+(i, k)blkdiag(\{{}_M\mathbf{n}_i^0\}^T {}_M\mathbf{A}_{MI})] \left( \mathbf{E} - \begin{bmatrix} [\mathbf{I}] & [-\tilde{\mathbf{R}}]_1 \\ \vdots & \vdots \\ [\mathbf{I}] & [-\tilde{\mathbf{R}}]_M \end{bmatrix} \mathbf{P}_{rigid}^T \right) \quad (3.35)$$

## 3.2 Criteria for model reduction

Building a dynamic ss-model of a structure, the first model is usually modal-based. This is in fact an implicit model reduction since only a limited number of modes is computed within the FE-software and this number is much smaller than the number of DOFs. Usually all modes are used from the first eigenfrequency up to a frequency, which should be 50% higher than the highest frequency, where the dynamic behavior should be represented well ([30]).

This criterion is only a rule of thumb and results for time-dependent simulations of large telescope system in much to large — and consequently to slow— models. Therefore higher effort has to be put on the reduction of system size and the basic question is, which modes and states should be kept.

### 3.2.1 Criteria for general transfer functions and linear time invariant systems

The simplest linear time invariant (LTI) systems are those with only a single input and a single output. These SISO systems are fully and unique described by their transfer function. For MIMO systems with multiple inputs and multiple outputs a transfer function matrix contains the complete system dynamics.

Thus the best reduced model  $\mathbf{G}_r(\omega)$  keeps the difference to the transfer function matrix of the full model  $\mathbf{G}(\omega)$  as small as possible:

$$\min_{\mathbf{G}_r(\omega)} \|\mathbf{G}(\omega) - \mathbf{G}_r(\omega)\|_p \quad (3.36)$$

The mathematical measure for the quantity of a scalar or a matrix signal like the difference of two transfer functions is a norm. Examples for norms of scalar functions are

$$\begin{aligned} \|x\|_1 &= \int_{-\infty}^{\infty} |x(t)| dt \\ \|x\|_2 &= \left( \int_{-\infty}^{\infty} |x(t)|^2 dt \right)^{1/2} \\ \|x\|_{\infty} &= \sup_{t \in \mathbb{R}} |x(t)| \end{aligned} \quad (3.37)$$

$\|x\|_1$  is called the action,  $\|x\|_2$  is the energy and  $\|x\|_{\infty}$  the amplitude of the signal  $x(t)$ .



Analogously is the generalization towards vector signals:

$$\begin{aligned}\|\mathbf{x}\|_1 &= \sum_i \int_{-\infty}^{\infty} |\mathbf{x}(t)| dt \\ \|\mathbf{x}\|_2 &= \left( \int_{-\infty}^{\infty} \mathbf{x}^H(t) \mathbf{x}(t) dt \right)^{1/2} \\ \|\mathbf{x}\|_{\infty} &= \max_i \sup_{t \in \mathbb{R}} |\mathbf{x}(t)|\end{aligned}\quad (3.38)$$

For quadratic matrices the same norms are defined:

$$\|\mathbf{A}\|_p = \sup_{\mathbf{x} \neq 0} \frac{\|\mathbf{Ax}\|_p}{\|\mathbf{x}\|_p} \quad (3.39)$$

Equivalent is a formulation of the norms in the frequency domain since the Parseval formula gives a relationship between frequency domain and time domain due to the conservation of energy:  $\int_{-\infty}^{\infty} x^T(t)x(t) dt = \frac{1}{2\pi} \int_{-\infty}^{\infty} X(\omega)^H X(\omega) d\omega$  with the Fourier transformed  $X(\omega) = \mathcal{F}(x(t))$

Unlike the transfer function matrix the ss-realization of a system is not unique. By applying the Laplace transform the transfer function can be computed from the state-space representation:

$$\mathbf{G}(s) = \mathbf{C}(\mathbf{A} - \mathbf{I}s)^{-1}\mathbf{B} + \mathbf{D} \quad (3.40)$$

The transformation of the states  $x$  with a non-singular transformation matrix  $T$  does not change the system and keeps the transfer function:

$$\begin{aligned}\mathbf{x} &= \mathbf{T}\tilde{\mathbf{x}} \\ \dot{\tilde{\mathbf{x}}} &= \mathbf{T}^{-1}\mathbf{A}\mathbf{T}\tilde{\mathbf{x}} + \mathbf{T}^{-1}\mathbf{B}\mathbf{u} = \tilde{\mathbf{A}}\tilde{\mathbf{x}} + \tilde{\mathbf{B}}\mathbf{u} \\ \mathbf{y} &= \mathbf{C}\mathbf{T}\tilde{\mathbf{x}} + \mathbf{D}\mathbf{u} = \tilde{\mathbf{C}}\tilde{\mathbf{x}} + \mathbf{D}\mathbf{u}\end{aligned}\quad (3.41)$$

$$\begin{aligned}\tilde{\mathbf{G}}(s) &= \tilde{\mathbf{C}}(\tilde{\mathbf{A}} - \mathbf{I}s)^{-1}\tilde{\mathbf{B}} + \mathbf{D} = \mathbf{C}\mathbf{T}(\mathbf{T}^{-1}\mathbf{A}\mathbf{T} - \mathbf{I}s)^{-1}\mathbf{T}\mathbf{B} + \mathbf{D} \\ &= \mathbf{C}(\mathbf{A} - \mathbf{I}s)^{-1}\mathbf{B} + \mathbf{D} = \mathbf{G}(s)\end{aligned}\quad (3.42)$$

The reduction of a state-space system means decreasing the number of states and is equivalent with reducing the number of poles of a transfer function. Partitioning

the states into two groups  $\left\{ \mathbf{x} \right\} = \left\{ \begin{array}{c} \mathbf{x}_{(1:r)} \\ \mathbf{x}_{(r+1:n)} \end{array} \right\} = \left\{ \begin{array}{c} \mathbf{x}_r \\ \mathbf{x}_t \end{array} \right\}$  with  $r + t = n$  and

$r$  respectively  $t$  representing the indices  $(1 : r)$  respectively  $(r + 1 : n)$  gives the following system:

$$\begin{aligned} \begin{Bmatrix} \dot{\mathbf{x}}_r \\ \dot{\mathbf{x}}_t \end{Bmatrix} &= \begin{bmatrix} \mathbf{A}_r & \mathbf{A}_{rt} \\ \mathbf{A}_{tr} & \mathbf{A}_t \end{bmatrix} \begin{Bmatrix} \mathbf{x}_r \\ \mathbf{x}_t \end{Bmatrix} + \begin{bmatrix} \mathbf{B}_r \\ \mathbf{B}_t \end{bmatrix} \{ \mathbf{u} \} \\ \{ \mathbf{y} \} &= \begin{bmatrix} \mathbf{C}_r & \mathbf{C}_t \end{bmatrix} \begin{Bmatrix} \mathbf{x}_r \\ \mathbf{x}_t \end{Bmatrix} + \begin{bmatrix} \mathbf{D} \end{bmatrix} \{ \mathbf{u} \} \end{aligned}$$

Reducing the system by the states  $\mathbf{x}_t$  is possible in two ways, either neglecting the effects completely or considering only the static influence. If effects of  $\mathbf{x}_t$  are complete neglected, i.e. the states and derivatives of the states are assumed to be nearly zero ( $\dot{\mathbf{x}}_t \approx \mathbf{x}_t \approx 0$ ), the states can be simple canceled:

$$\begin{aligned} \mathbf{x}_t \approx \dot{\mathbf{x}}_t \approx 0 : \Rightarrow \\ \begin{Bmatrix} \dot{\mathbf{x}}_r \\ \mathbf{y} \end{Bmatrix} &= \begin{bmatrix} \mathbf{A}_r \\ \mathbf{C}_r \end{bmatrix} \begin{Bmatrix} \mathbf{x}_r \end{Bmatrix} + \begin{bmatrix} \mathbf{B}_r \\ \mathbf{D} \end{bmatrix} \begin{Bmatrix} \mathbf{u} \end{Bmatrix} \end{aligned} \quad (3.43)$$

To take the static impact of  $\mathbf{x}_t$  into account  $\dot{\mathbf{x}}_t$  is set to zero and  $\mathbf{x}_t$  is eliminated:

$$\begin{aligned} \dot{\mathbf{x}}_t \approx 0, \mathbf{x}_t \neq 0 : \Rightarrow \\ \mathbf{A}_{tr}\mathbf{x}_r + \mathbf{A}_t\mathbf{x}_t + \mathbf{B}_t\mathbf{u} = 0, \Rightarrow \mathbf{x}_t = -\mathbf{A}_t^{-1}\mathbf{A}_{tr}\mathbf{x}_r - \mathbf{A}_t^{-1}\mathbf{B}_t\mathbf{u} \Rightarrow \\ \begin{Bmatrix} \dot{\mathbf{x}}_r \\ \mathbf{y} \end{Bmatrix} &= \begin{bmatrix} \mathbf{A}_r - \mathbf{A}_{rt}\mathbf{A}_t^{-1}\mathbf{A}_{tr} \\ \mathbf{C}_r - \mathbf{C}_t\mathbf{A}_t^{-1}\mathbf{A}_{tr} \end{bmatrix} \begin{Bmatrix} \mathbf{x}_r \end{Bmatrix} + \begin{bmatrix} \mathbf{B}_r - \mathbf{A}_{rt}\mathbf{A}_t^{-1}\mathbf{B}_t \\ \mathbf{D} - \mathbf{C}_t\mathbf{A}_t^{-1}\mathbf{B}_t \end{bmatrix} \begin{Bmatrix} \mathbf{u} \end{Bmatrix} \end{aligned} \quad (3.44)$$

Figure 3.2 shows as example the reduction of the fourth order transfer function

$$H(s) = \frac{s^3 + 11s^2 + 36s + 26}{s^4 + 14.6s^3 + 74.96s^2 + 153.7s + 99.65}. \quad (3.45)$$

This transfer function can be well approximated by a first order system and both methods perform very well. The second reduction keeps the static gain (see left plot), but increases the error significantly in the high frequency range for both the amplitude and the phase. This can cause serious problems for the stability of a control system.

The influence of the inputs onto the system states and the influence of the individual states onto the outputs is described with the controllability and observability. In the state-space format the only states that have a contribution to the output  $\mathbf{y}$  due to the inputs  $\mathbf{u}$  are the ones that are controllable and observable. According to the controllability and observability the states can be divided into the four groups with

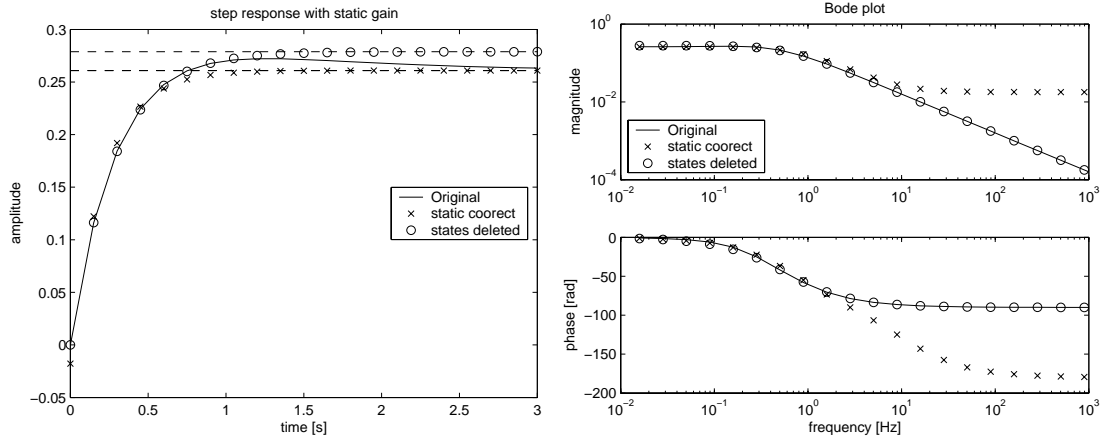


Figure 3.2: Model reduction of a simple system with originally 4 states to a 1 state system. The two reduction methods keeping static gain and simple deleting a state are compared. Deleting a state results in better results in the high frequency range, whereas the other methods keeps exactly the system characteristics in the low frequency range respectively the long time-range.

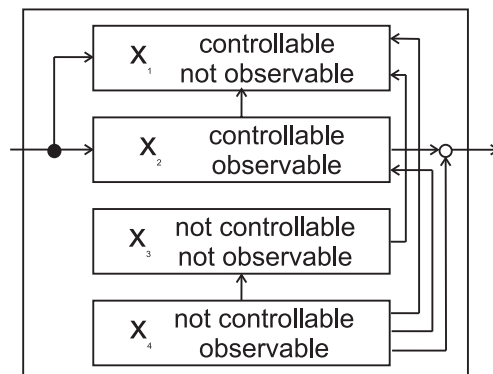


Figure 3.3: Grouping of the states into four blocks according to their controllability and observability. The transfer function, which gives the relation from the inputs to the outputs, is only influenced by the block of fully controllable and observable states.

$\tilde{\mathbf{x}} = T^{-1}\mathbf{x} = (\mathbf{x}_1^T, \mathbf{x}_2^T, \mathbf{x}_3^T, \mathbf{x}_4^T)^T$  as shown in figure 3.3. The structure of the resulting state-space model can be seen in the figure and reads:

$$\frac{d}{dt} \begin{Bmatrix} \tilde{\mathbf{x}}_1 \\ \tilde{\mathbf{x}}_2 \\ \tilde{\mathbf{x}}_3 \\ \tilde{\mathbf{x}}_4 \end{Bmatrix} = \begin{bmatrix} \tilde{\mathbf{A}}_{11} & \tilde{\mathbf{A}}_{12} & \tilde{\mathbf{A}}_{13} & \tilde{\mathbf{A}}_{14} \\ \mathbf{0} & \tilde{\mathbf{A}}_{22} & \mathbf{0} & \tilde{\mathbf{A}}_{24} \\ \mathbf{0} & \mathbf{0} & \tilde{\mathbf{A}}_{33} & \tilde{\mathbf{A}}_{34} \\ \mathbf{0} & \mathbf{0} & \mathbf{0} & \tilde{\mathbf{A}}_{44} \end{bmatrix} \begin{Bmatrix} \tilde{\mathbf{x}}_1 \\ \tilde{\mathbf{x}}_2 \\ \tilde{\mathbf{x}}_3 \\ \tilde{\mathbf{x}}_4 \end{Bmatrix} + \begin{bmatrix} \tilde{\mathbf{B}}_1 \\ \tilde{\mathbf{B}}_2 \\ \mathbf{0} \\ \mathbf{0} \end{bmatrix} \{ \mathbf{u}(t) \}$$

$$\{ \mathbf{y}(t) \} = \begin{bmatrix} \mathbf{0} & \tilde{\mathbf{C}}_2 & \mathbf{0} & \tilde{\mathbf{C}}_4 \end{bmatrix} \begin{Bmatrix} \tilde{\mathbf{x}}_1 \\ \tilde{\mathbf{x}}_2 \\ \tilde{\mathbf{x}}_3 \\ \tilde{\mathbf{x}}_4 \end{Bmatrix}$$
(3.46)

### 3.2.2 Criteria for transfer functions of mechanical structures

Up to now general transfer functions were considered which represent for SISO systems the complex amplitude function (amplitude and phase) giving the system response to an harmonic excitation with unit amplitude depending on the frequency  $\omega = 2\pi f$ . The (MIMO) transfer function matrix can be interpreted similar, but instead of a harmonic input a white noise input with unit amplitude must be assumed. This section focuses on the aspects of mechanical structures.

For a harmonic excitation also a harmonic response can be expected and therefore the modal equation of motion  $\{\ddot{\mathbf{q}}\} + [diag(2\zeta_i\omega_i)]\{\dot{\mathbf{q}}\} + [diag(\omega_i^2)]\{\mathbf{q}\} = [\phi]^T\{f\}$  with  $m$  modes can be solved:

$$\mathbf{Q}_i(\omega) = \sum_{k=1}^m \frac{\phi_{jk}\mathbf{F}_j(\omega)}{-\omega^2 + i2\zeta_k\omega_k\omega + \omega_k^2} \quad (3.47)$$

Including  $\mathbf{x} = [\phi]\{\mathbf{q}\}$  the transfer function matrix  $\mathbf{H}_{ij}(\omega) = \frac{\mathbf{X}_i(\omega)}{\mathbf{F}_j(\omega)}$  is given as the superposition of the individual modes:

$$\mathbf{H}_{ij}(\omega) = \frac{\mathbf{X}_i(\omega)}{\mathbf{F}_j(\omega)} = \sum_{k=1}^m \frac{\phi_{ik}\phi_{jk}}{-\omega^2 + i2\zeta_k\omega_k\omega + \omega_k^2} \quad (3.48)$$

Considering certain load sets with distributed loads but the same time-history within a single load set, these can be expressed by defining  $\mathbf{f}(t) = [\mathbf{P}_L]\{\mathbf{u}(t)\}$  with the matrix  $[\mathbf{P}_L]$  defining in each column the distribution of a load set (with fixed amplitude and phase differences between the different DOFs) and the vector  $\{\mathbf{u}(t)\}$  describing the time-history. An analog formula can be used to describe relevant outputs as linear combinations of the displacements like e.g. a quantity measured by a sensor:  $\{\mathbf{y}\} = [\mathbf{P}_S]^T\{\mathbf{x}\}$ , where each column of  $[\mathbf{P}_S]$  represents the linear combination used for one output. So the complete transfer function matrix reads:

$$\mathbf{G}_{gh}(\omega) = \frac{\mathbf{Y}_g(\omega)}{\mathbf{U}_h(\omega)} = \sum_{k=1}^m \frac{\mathbf{P}_{S,ig}\phi_{ik}\phi_{jk}\mathbf{P}_{L,jh}}{-\omega^2 + i2\zeta_k\omega_k\omega + \omega_k^2} \quad (3.49)$$

or with matrix notation:

$$[\mathbf{G}(\omega)] = [\mathbf{P}_S]^T[\phi][diag([-\omega^2 + i2\zeta_k\omega_k\omega + \omega_k^2]^{-1})][\phi]^T[\mathbf{P}_L] \quad (3.50)$$

Directly with equation (3.49) can be seen, that the modes  $k$  with larger numerator  $N = \mathbf{P}_S^T\phi_{ik}\phi_{jk}^T\mathbf{P}_L$  are more important than modes with smaller  $N$ . For modes with the same  $N$  the one with higher eigenfrequency distributes less to the amplitude of the transfer function.

The modes with  $\|\mathbf{P}_S^T\phi_{ik}\| = 0$  or  $\|\phi_{jk}^T\mathbf{P}_L\| = 0$  (and accordingly the respective states in the state space system) have no effect onto the system outputs as they are not

observable respectively controllable. An example could be a rotational mode of an axially symmetric mirror rotating along the optical axis, which does not influence an image.

In the frequency range far below the eigenfrequency a single mode acts only statically with its static flexibility. In a high frequency range the amplitude of a single mode falls with  $1/\omega^2$ . The real dynamic is in the range of the resonance, where the amplitude rises to  $1/(2 * \zeta_i)$  times the static flexibility (for small damping values  $\zeta$ ).

Besides the frequency range different criteria exist allowing to evaluate whether the number of modes is sufficient or whether an essential part of the global structural characteristics is not represented. These quantities have a physical meaning and should be matched by a reduced model.

For the frequency  $\omega = 0$  the transfer function represents the static flexibility, which is the inverse of the stiffness matrix  $K$ :

$$[\mathbf{H}_{ij}(\omega = 0)] = [\mathbf{K}]^{-1} \approx \sum_{k=1}^m \frac{\phi_{ik}\phi_{jk}}{\omega_k^2} \quad (3.51)$$

Therefore the magnitude of  $\frac{\phi_{ik}\phi_{jk}}{\omega_k^2}$  indicates the relevance of mode  $k$  for the transfer function  $H_{ij}$ . This is not only true for low frequencies, but also the peak amplitude in the resonance is approximately  $\frac{\phi_{ik}\phi_{jk}}{2\zeta_i\omega_k^2}$  and thus proportional to the static flexibility. Computing the flexibility in a static analysis allows to compensate for the lack of flexibility due to modal reduction by adding the fraction distributed to deleted modes (see also [31]):

$$[\mathbf{H}_{ij}(\omega)] = \sum_{k=1}^m \frac{\phi_{ik}\phi_{jk}}{-\omega^2 + i2\zeta_k\omega_k\omega + \omega_k^2} + \underbrace{\left([\mathbf{K}]^{-1} - \sum_{k=1}^m \frac{\phi_{ik}\phi_{jk}}{\omega_k^2}\right)}_{\text{Flexibility of the modes } (m+1:\infty)} \quad (3.52)$$

This results in a feedthrough component in the state-space model and is equivalent to the model reduction matching static gain. The drawback is the large error in amplitude and phase for higher frequencies and the danger of causing instability in closed loop systems.

For very high frequencies the distribution of mass dominates the behavior of the structure. This gives  $\phi^T\phi$  as characteristic:

$$-\omega^2[\mathbf{H}_{ij}(\omega \rightarrow \infty)] = [\mathbf{M}]^{-1} = \sum_{k=1}^m \phi_{ik}\phi_{jk} \quad (3.53)$$

In fact this characteristic is much less important than the flexibility, since a mechanical structure behaves like a low pass filter for displacements due to forces.

The effective modal mass is another characteristic, that is often provided as a result by the modal analysis within the FE software. Exciting the whole structure to oscillate

as rigid body with frequency  $1 \text{ rad/s}$  and amplitude  $1 \text{ m}$  is caused by a force  $f$  equal to the mass distributed to a generalized DOF:  $\{\mathbf{f}\} = [\mathbf{M}]\{\mathbf{x}_r\}[\frac{1}{s^2}]$ . The fraction of the total mass represented by each of the modes (i.e. the transformation of this force  $\mathbf{f}$  into the modal coordinates) can be calculated with  $\mathbf{M}_{modal} = |[\phi]^T[\mathbf{M}]\{\mathbf{x}_r\}|$  with a vector  $\{\mathbf{x}_r\}$  describing a rigid body displacement or rotation of the structure and the resulting modal mass vector  $\mathbf{M}_{modal}$ . The full modal model gives the total unsupported mass of the structure as the sum of all effective masses. This criterion is important to evaluate, if an important fraction of modes is still missing in the extracted set.

### 3.2.3 Gramians

As mentioned before, the controllability and observability are important to evaluate the relevancy of a mode respectively a state. Different methods to check the controllability and observability exist in control engineering, e.g. the Kalman criterion:

A system  $(\mathbf{A}, \mathbf{B}, \mathbf{C}, \mathbf{D})$  is fully controllable if (and only if) the  $N \times sN$  matrix  $\mathcal{C} = \begin{bmatrix} \mathbf{B} & \mathbf{A}\mathbf{B} & \mathbf{A}^2\mathbf{B} & \dots & \mathbf{A}^{N-1}\mathbf{B} \end{bmatrix}$  has full rank  $N$  and fully observable if (and only if)  $\mathcal{O}^T = \begin{bmatrix} \mathbf{C}^T & [\mathbf{C}\mathbf{A}]^T & [\mathbf{C}\mathbf{A}^2]^T & \dots & [\mathbf{C}\mathbf{A}^{N-1}]^T \end{bmatrix}$  has rank  $N$ .

The main drawback of these criteria is the large effort for the computation of the matrices  $\mathcal{C}$  and  $\mathcal{O}$ . Moreover, they allow only to state, whether the system is fully controllable/observable or not, but no quantitative measure for the individual states.

If a system consists of only controllable and observable states, it is called a minimal realization. However, MIMO systems usually have only very few states, which are not controllable or not observable, but some are very well controllable and observable and some only very weakly. Thus it is necessary to evaluate this property.

A quantitative measure are the controllability and observability Gramians, which are defined as:

$$\text{Controllability Gramian: } \mathbf{W}_C = \int_0^\infty \exp(\mathbf{A}t)\mathbf{B}\mathbf{B}^H \exp(\mathbf{A}^Ht) dt \quad (3.54)$$

$$\text{Observability Gramian: } \mathbf{W}_O = \int_0^\infty \exp(\mathbf{A}^Ht)\mathbf{C}^H\mathbf{C} \exp(\mathbf{A}t) dt \quad (3.55)$$

They are also the solution to the Lyapunov equations (see appendix C), which can be solved numerically much more efficient:

$$\mathbf{A}\mathbf{W}_C + \mathbf{W}_C\mathbf{A}^H + \mathbf{B}\mathbf{B}^H = 0 \quad \mathbf{A}^H\mathbf{W}_O + \mathbf{W}_O\mathbf{A} + \mathbf{C}^H\mathbf{C} = 0 \quad (3.56)$$

The Gramians  $\mathbf{W}_C$  and  $\mathbf{W}_O$  are positive definite if (and only if)  $(\mathbf{A}, \mathbf{B})$  respectively  $(\mathbf{A}, \mathbf{C})$  are completely controllable respectively observable.

The controllability Gramian has also a certain physical meaning. The general response of a state-space system to an input  $\mathbf{u}(t)$  can be expressed for the state  $\mathbf{x}(t)$  as

$$\mathbf{x}(t) = e^{\mathbf{A}t} \mathbf{x}_0 + \int_0^t e^{\mathbf{A}(t-\tau)} \mathbf{B} \mathbf{u}(\tau) d\tau \quad (3.57)$$

respectively with  $\mathbf{y} = \mathbf{C}\mathbf{x} + \mathbf{D}\mathbf{u}$  for the output  $\mathbf{y}(t)$

$$\mathbf{y}(t) = \mathbf{C}e^{\mathbf{A}t} \mathbf{x}_0 + \int_0^t e^{\mathbf{A}(t-\tau)} \mathbf{B} \mathbf{u}(\tau) d\tau + \mathbf{D}\mathbf{u}(t) \quad (3.58)$$

If a state-space system with initial states  $\mathbf{x}(t=0) = \mathbf{x}_0$  is brought to the states  $\mathbf{x}(t=T_e) = \mathbf{x}_e$ , the optimal solution with the least input energy  $J(\mathbf{u}) = \int_0^{T_e} \mathbf{u}^H \mathbf{u} dt = \min$  is

$$\mathbf{u}_{opt[0,T_e]}(t) = -\mathbf{B}^H e^{\mathbf{A}^H(T_e-t)} \mathbf{W}_s^{-1} (e^{\mathbf{A}T_e} \mathbf{x}_0 - \mathbf{x}_e) \quad (3.59)$$

with  $\mathbf{W}_s = \int_0^{T_e} e^{\mathbf{A}t} \mathbf{B} \mathbf{B}^H e^{\mathbf{A}^H t} dt$ .  $\mathbf{x}_e$  can be reached from  $\mathbf{x}_0$  in an arbitrary short time. However, the smaller the time  $T_e$ , the larger is  $\mathbf{u}$  since the elements of  $\mathbf{W}_s$  decrease and  $\mathbf{W}_s^{-1}$  vice versa. The controllability Gramian  $\mathbf{W}_C$  is equal to  $\mathbf{W}_s$  for an infinite time  $T_e \rightarrow \infty$ .

An analog interpretation is possible for the observability Gramian which represents the output energy stored in the system at time  $t=0$  in the initial states  $\mathbf{x}(t=0) = \mathbf{x}_0$  (for a system with  $\mathbf{u}(t \geq 0) = 0$ ) according to (3.58):

$$\int_0^\infty \mathbf{y}^H(t) \mathbf{y}(t) dt = \int_0^\infty \mathbf{x}_0^H e^{\mathbf{A}^H t} \mathbf{C}^H \mathbf{C} e^{\mathbf{A}t} \mathbf{x}_0 dt = \mathbf{x}_0^H \mathbf{W}_O \mathbf{x}_0 \quad (3.60)$$

The Gramians are strongly dependent on the chosen state coordinates. In the transformed coordinates  $\tilde{\mathbf{x}} = \mathbf{T}\mathbf{x}$  according to (3.41) they read

$$\tilde{\mathbf{W}}_C = \mathbf{T} \mathbf{W}_C \mathbf{T}^H; \quad \tilde{\mathbf{W}}_O = \mathbf{T}^{-H} \mathbf{W}_O \mathbf{T}^{-1}, \quad (3.61)$$

whereas the product  $\tilde{\mathbf{W}}_C \tilde{\mathbf{W}}_O = \mathbf{T} \mathbf{W}_C \mathbf{W}_O \mathbf{T}^{-1}$  keeps the eigenvalues after a transformation.

Therefore Hankel singular values are defined, which are independent of the system realization and exist for stable systems  $G(s)$  without integrators (i.e.  $\Re(\lambda_i(\mathbf{A})) < 0 \forall i$ ):

$$\sigma_i(G(s)) := (\lambda_i(\mathbf{W}_C \mathbf{W}_O))^{1/2}; \quad \sigma_i \geq \sigma_{i+1} \quad (3.62)$$

The Hankel singular values are a characteristic of a system and allow to define the Hankel-norm:

$$\|\mathbf{G}(s)\|_H := \bar{\sigma}(\mathbf{G}(s)) = \lambda_{max}^{1/2}(\mathbf{W}_C \mathbf{W}_O) \quad (3.63)$$

The physical interpretation of the Hankel norm is the maximum energy efficiency from an input to the output: If  $\mathbf{u}(t \geq 0) = 0$  then  $\|\mathbf{G}_x\|_H = \sup \frac{\|\mathbf{y}\|_{2(0,\infty)}}{\|\mathbf{u}\|_{2(-\infty,0)}}$ , which is the Euclidean norm from past inputs to future outputs.

### 3.3 Balanced model reduction

A system is called balanced, if controllability and observability Gramians are equal and diagonal:  $\mathbf{W}_C = \mathbf{W}_O = \Gamma = \text{diag}(\gamma_i)$ ;  $\gamma_i > 0$ . The balanced realization was defined by Moore [32] and had a large impact onto the progression of model reduction.

A comprehensive paper about balanced model reduction is [33], which considers also stability aspects and algorithms. [34] applied balanced model reduction especially to mechanical structures and gives approximations for the Gramians. Error bounds and the relation between the Hankel-norm, the  $H_\infty$ -norm and the  $H_2$ -norm are the concern of [35].

For the balancing transformation  $\mathbf{T}$ , which transforms  $\mathbf{A}$ ,  $\mathbf{B}$ ,  $\mathbf{C}$  to  $\mathbf{A}_b = \mathbf{T}^{-1}\mathbf{A}\mathbf{T}$ ,  $\mathbf{B}_b = \mathbf{T}^{-1}\mathbf{B}$ ,  $\mathbf{C}_b = \mathbf{C}\mathbf{T}$  first of all the Gramians  $\mathbf{W}_C$  and  $\mathbf{W}_O$  must be decomposed with Cholesky or singular value decomposition (SVD) to  $\mathbf{W}_C = \mathbf{R}\mathbf{R}^T$  and  $\mathbf{W}_O = \mathbf{S}^T\mathbf{S}$ . With the resulting matrices from the SVD of the product  $\mathbf{S}\mathbf{R} = \mathbf{V}\mathbf{T}\mathbf{U}^T$  the transformation matrix can be computed:  $\mathbf{T} = \mathbf{R}\mathbf{U}\mathbf{T}^{-1/2}$ .

For a balanced system the new states  $\tilde{\mathbf{x}} = \mathbf{T}^{-1}\mathbf{x}$  are sorted according to their contribution to the Hankel singular values (HSV). This allows easily to reduce the states with the least impact onto the observability/controllability. A second large advantage is, that a lower bound on the  $H_\infty$  error is given for a reduced balanced system:

$$\|\mathbf{G}_n(s) - \mathbf{G}_r(s)\|_\infty < 2 \sum_{i=r+1}^n \sigma_i(\mathbf{G}_n) \quad (3.64)$$

The Gramians can be expressed as the sum of the contributions of the individual SISO systems:

$$\mathbf{W}_C = \sum \mathbf{W}_{C,u(i)}, \quad \mathbf{W}_O = \sum \mathbf{W}_{O,y(j)} \quad (3.65)$$

Accordingly it is possible to consider the individual inputs and outputs independently. Though it is necessary to scale the inputs and outputs to appropriated sizes, as they are all assumed to be equally important, but can contain totally different quantities with very unlike meaning. It is therefore important to include the expected amplitude of input and output signals into the  $\mathbf{P}_L$  and  $\mathbf{P}_S$  matrices e.g. in order to scale all inputs and outputs to unit amplitude or according to their relevancy.

For the state space representation of an  $m$  mode system ( $i = 1..m$ ) with two inputs and two outputs (either displacement- or velocity output) and with

$$\mathbf{A}_i = \begin{bmatrix} 0 & \omega_i \\ -\omega_i & -2\zeta_i\omega_i \end{bmatrix}; \quad \mathbf{B}_i = \begin{bmatrix} 0 & 0 \\ q_{i1} & q_{i2} \end{bmatrix}; \quad \mathbf{C}_i = \begin{bmatrix} p_{i1}/\omega_i & 0 \\ p_{i2}/\omega_i & 0 \end{bmatrix} \text{ or } \mathbf{C}_i = \begin{bmatrix} 0 & p_{v_{i1}} \\ 0 & p_{v_{i2}} \end{bmatrix},$$



$q_{ij} = \phi_{ik}^T \mathbf{P}_{Lkj}$ : contribution of  $u_j$  to mode  $i$

$p_{ij} = \phi_{ik}^T \mathbf{P}_{Skj}$ : contribution of mode  $i$  to output  $y_j$

as in (3.6) the following observability Gramians result for displacement- respectively velocity-outputs:

$$\mathbf{W}_{Oi} = -\frac{p_{i1}^2 + p_{i2}^2}{4\zeta_i \omega_i^3} \begin{bmatrix} 1 + 4\zeta_i^2 & 2\zeta_i \\ 2\zeta_i & 1 + 4\zeta_i^2 \end{bmatrix} \quad \text{respectively} \quad \mathbf{W}_{O_i} = -\frac{p_{v_{i1}}^2 + p_{v_{i2}}^2}{4\zeta_i \omega_i} \begin{bmatrix} 1 & 0 \\ 0 & 1 \end{bmatrix} \quad (3.66)$$

The controllability Gramians read:

$$\mathbf{W}_{Ci} = -\frac{p_{i1}^2 + p_{i2}^2}{4\zeta_i \omega_i} \begin{bmatrix} 1 & 0 \\ 0 & 1 \end{bmatrix} \quad (3.67)$$

The Hankel singular values for displacement outputs are given by

$$\begin{aligned} \gamma_{i/i+1} &= \text{eig}(\mathbf{W}_C \mathbf{W}_O)_{i/i+1} = \frac{1}{4} \sqrt{\frac{(1+2\zeta_i^2 \pm 2\zeta_i \sqrt{1+\zeta_i^2})(p_{i1}^2 + p_{i2}^2)(q_{i1}^2 + q_{i2}^2)}{\zeta_i^2 \omega_i^4}} \\ &= \frac{p_i q_i}{4} \sqrt{\frac{(1+2\zeta_i^2 \pm 2\zeta_i \sqrt{1+\zeta_i^2})}{\zeta_i^2 \omega_i^4}} \approx \frac{p_i q_i}{4\zeta_i \omega_i^2} \end{aligned} \quad (3.68)$$

with  $p_i = \sqrt{p_{i1}^2 + p_{i2}^2}$ ,  $q_i = \sqrt{q_{i1}^2 + q_{i2}^2}$  and the last approximation assumes small modal damping  $\zeta_i$ .

The velocity outputs result with  $p_{v_i} = \sqrt{p_{v_{i1}}^2 + p_{v_{i2}}^2}$  in

$$\begin{aligned} \gamma_{i/i+1} &= \frac{1}{4\zeta_i \omega_i} \sqrt{(p_{v_{i1}}^2 + p_{v_{i2}}^2)(q_{i1}^2 + q_{i2}^2)} \\ &= \frac{p_{v_i} q_i}{4\zeta_i \omega_i} \end{aligned} \quad (3.69)$$

Gregory ([36]) showed that for a lightly damped structure the Hankel singular values for outputs mixed from velocities and displacements can be approximated with:

$$\gamma_i \approx \gamma_{i+1} \approx \frac{1}{4\zeta_i \omega_i^2} \sqrt{q_i^2 (p_i^2 + \omega_i^2 p_{v_i}^2)} \quad (3.70)$$

Using therefore force inputs and either displacement outputs or velocity outputs allows a very fast exact computation of the HSVs. For low structural damping, equation (3.70) is a good approximation which is easy to compute. Hence the large effort for solving the Lyapunov equation is not necessary. Comparing the HSVs in equation (3.68) with the formula of the modal transfer function in equation (3.49) and considering the definitions of  $p_i$  and  $q_i$  according to (3.3) shows that the HSVs are the peak amplitude of the transfer function for a SISO system.

Due to the definition of Gramians in equations (3.54), they do not exist for systems with integrators. Structural models, which also include rigid body modes, have such poles at  $\omega = 0$ . To apply balanced model reduction, the modes have to be split into the two groups with real vibration modes ( $\omega > 0$ ) and the rigid body modes. The model reduction is only applied to the vibration modes and the others are simply kept. Moreover the representation of rigid body modes is not possible in the form suggested in (3.6) with

$$\mathbf{A}_i = \begin{bmatrix} 0 & \omega_i \\ -\omega_i & -2\zeta_i\omega_i \end{bmatrix}; \quad \mathbf{B}_i = \begin{bmatrix} [0] \\ [\phi_i]^T[\mathbf{P}_L] \end{bmatrix}; \quad \mathbf{C}_i = \begin{bmatrix} [\mathbf{P}_S]^T[\phi_i]/\omega_i & [0] \end{bmatrix},$$

since the  $\mathbf{C}_i$  matrix would not exist and the  $\mathbf{A}_i$  matrix would consist of zeros only. Therefore format analog to equation (3.4) with

$$\mathbf{A}_i = \begin{bmatrix} 0 & 1 \\ 0 & 0 \end{bmatrix}; \quad \mathbf{B}_i = \begin{bmatrix} [0] \\ [\phi_i]^T[\mathbf{P}_L] \end{bmatrix}; \quad \mathbf{C}_i = \begin{bmatrix} [\mathbf{P}_S]^T[\phi_i] & [0] \end{bmatrix}$$

must be used for each rigid body mode.

Due to the Fourier transformation and the Parseval theorem, Gramians are also defined in the frequency domain:

$$\begin{aligned} \mathbf{W}_C &= \frac{1}{2\pi} \int_{-\infty}^{\infty} (j\omega\mathbf{I} - \mathbf{A})^{-1} \mathbf{B} \mathbf{B}^H (j\omega\mathbf{I} - \mathbf{A})^{-H} d\omega \\ \mathbf{W}_O &= \frac{1}{2\pi} \int_{-\infty}^{\infty} (j\omega\mathbf{I} - \mathbf{A})^{-H} \mathbf{C}^H \mathbf{C} (j\omega\mathbf{I} - \mathbf{A})^{-1} d\omega \end{aligned} \quad (3.71)$$

Since input disturbances are usually not white noise signals it is advantageous to include the expected spectrum of the input into the model reduction. Similarly also the relevancy of different frequencies of the output signal is different. This is the reason why a frequency weighted balanced model reduction should be used. Thus the new reduction task reads:

$$\min_{\mathbf{G}_r(\omega)} \|\mathbf{W}_y(\omega)(\mathbf{G}(\omega) - \mathbf{G}_r(\omega))\mathbf{W}_u(\omega)\|_P \quad (3.72)$$

This means, the spectral distribution of the inputs and outputs is already included into the state-space model before model reduction. However, after a reduction the system and the weightings cannot be separated any more. If necessary, the reduced systems are again weighted with the inverse weighting matrices. Alternatively the input can be scaled accordingly.

An example for a load with non-uniform spectral distribution is the wind load, which has a decreasing amplitude with increasing frequency. Therefore the low order modes of a system are most important, whereas the higher order modes are anyway less excited. (see section 2.5.2).

### 3.4 Other reduction methods

Besides the balanced model reduction, many other methods exist, which were evaluated to be not as suited as the selected one. Nevertheless a short overview will be given to see the main characteristics of these methods.

A method to reduce the DOFs within the FE-model is the Guyan reduction, which gives also eigenvectors with less DOFs. In a semi-automatic process supported by the FE-software, the DOFs are divided into so called *master DOFs* and *slave DOFs*, where the forces are suppose to be applied only on the *masters* and the dynamics between *masters* and *slaves* should be negligible:

$$\begin{aligned} \begin{bmatrix} \mathbf{M}_M & \mathbf{M}_{MS} \\ \mathbf{M}_{SM} & \mathbf{M}_S \end{bmatrix} \begin{Bmatrix} \ddot{\mathbf{x}}_M \\ \ddot{\mathbf{x}}_S \end{Bmatrix} + \begin{bmatrix} \mathbf{K}_M & \mathbf{K}_{MS} \\ \mathbf{K}_{SM} & \mathbf{K}_S \end{bmatrix} \begin{Bmatrix} \mathbf{x}_M \\ \mathbf{x}_S \end{Bmatrix} = \begin{Bmatrix} \mathbf{f}_M \\ \mathbf{0} \end{Bmatrix} \\ \begin{bmatrix} \mathbf{M}_{SM} & \mathbf{M}_S \end{bmatrix} \begin{Bmatrix} \ddot{\mathbf{x}}_M \\ \ddot{\mathbf{x}}_S \end{Bmatrix} \approx \mathbf{0} \Rightarrow \mathbf{x}_S = -\mathbf{K}_S^{-1} \mathbf{K}_{SM} \mathbf{x}_M \end{aligned} \quad (3.73)$$

Then the mass represented by the *slave DOFs* is contributed to the *master DOFs* according to the stiffness matrix:

$$\begin{aligned} \begin{bmatrix} \mathbf{M}_M - \mathbf{M}_{MS} \mathbf{K}_S^{-1} \mathbf{K}_{SM} \end{bmatrix} \begin{Bmatrix} \ddot{\mathbf{x}}_M \end{Bmatrix} + \begin{bmatrix} \mathbf{K}_M - \mathbf{K}_{MS} \mathbf{K}_S^{-1} \mathbf{K}_{SM} \end{bmatrix} \begin{Bmatrix} \mathbf{x}_M \end{Bmatrix} = \begin{Bmatrix} \mathbf{f}_M \end{Bmatrix} \\ \begin{Bmatrix} \mathbf{x} \end{Bmatrix} = \begin{Bmatrix} \mathbf{x}_M \\ \mathbf{x}_S \end{Bmatrix} = \begin{bmatrix} \mathbf{I} \\ \mathbf{K}_S^{-1} \mathbf{K}_{SM} \end{bmatrix} \begin{Bmatrix} \mathbf{x}_M \end{Bmatrix} \end{aligned} \quad (3.74)$$

Today the meaning of the Guyan reduction has become lower, since the computers are powerful and therefore the computation time and resources required for a modal analysis are not crucial. Moreover for importing the eigenvectors to build a state-space model, it is sufficient to read only the DOFs with any inputs or outputs.

A very powerful method for model reduction is the Krylov method, which computes a subspace to represent a system. The idea is to expand the transfer function of the state-space system  $\Sigma = (\mathbf{A}, \mathbf{B}, \mathbf{C}, \mathbf{D})$  around  $s_0$ :

$$G(s) = \eta_0 + \eta_1(s - s_0) + \eta_2(s - s_0)^2 + \eta_3(s - s_0)^3 + \dots \quad (3.75)$$

with the so called moments  $\eta_j$  at  $s_0$ . The model reduction is to find a reduced system  $\hat{\Sigma} = (\hat{\mathbf{A}}, \hat{\mathbf{B}}, \hat{\mathbf{C}}, \hat{\mathbf{D}})$ , with

$$\hat{G}(s) = \hat{\eta}_0 + \hat{\eta}_1(s - s_0) + \hat{\eta}_2(s - s_0)^2 + \hat{\eta}_3(s - s_0)^3 + \dots \quad (3.76)$$

such that for a proper  $l$ :  $\eta_j = \hat{\eta}_j$ ,  $m = 1, 2, 3, \dots, l$ .

The Krylov subspace is computed in an iterative way and is e.g. for the matrix  $\mathbf{A} \in \mathbb{R}^{n \times n}$  and an initial vector  $\mathbf{b} \in \mathbb{R}^n$ :  $K_l(\mathbf{A}, \mathbf{b}) = \text{span}\{\mathbf{b}, \mathbf{A}\mathbf{b}, \dots, \mathbf{A}^{l-1}\mathbf{b}\}$ ,  $1 \leq l \leq n$ .

The Krylov methods involve the advantages to be highly efficient <sup>5</sup> and contain not the danger of ill-conditioning. However, there is no global error bound existing, the truncated system may be instable and sometimes the algorithms break down and have to restart. The method is recommended for systems with much less inputs and outputs than states, but for some thousands to one million states. State-space models of telescope structures are typically of some thousand states maximum, while having some hundreds to thousand inputs and outputs for segmented mirrors or bogie drive systems with distributed motors. That is the reason, why the balanced method is preferred. Moreover, the special structure of modal state-space models allows a much quicker computation of the Gramians than the standard algorithms, which are designed for full matrices.

For systems, that are composed of several elastic subsystems, the component mode synthesis was developed (see [37]). This allows, e.g., different organizations to built the models of the subsystems independently and changes affecting a subsystem require not the update of the complete structure, but only of the relevant component.

The structure is split into interface DOFs  $i$ , to which forces are applied or other substructures are connected to, and interior DOFs where no forces are acting on:

$$\begin{bmatrix} \mathbf{M}_{ii} & \mathbf{M}_{ij} \\ \mathbf{M}_{ji} & \mathbf{M}_{jj} \end{bmatrix} \begin{Bmatrix} \ddot{\mathbf{x}}_i \\ \ddot{\mathbf{x}}_j \end{Bmatrix} + \begin{bmatrix} \mathbf{K}_{ii} & \mathbf{K}_{ij} \\ \mathbf{K}_{ji} & \mathbf{K}_{jj} \end{bmatrix} \begin{Bmatrix} \mathbf{x}_i \\ \mathbf{x}_j \end{Bmatrix} = \begin{Bmatrix} \mathbf{f}_i \\ \mathbf{0} \end{Bmatrix} \quad (3.77)$$

Two kinds of mode sets are created from this equation: constraint modes  $\psi_{ji}$  and the fixed interface normal modes  $\Phi_{ik}$  with corresponding modal frequency  $\omega_k$ . The fixed interface normal modes are the structural modes of the system, which is fixed at all DOFs  $i$  and results from the eigenvalue problem corresponding to the equation:

$$\begin{bmatrix} \mathbf{M}_{jj} \end{bmatrix} \begin{Bmatrix} \ddot{\mathbf{x}}_j \end{Bmatrix} + \begin{bmatrix} \mathbf{K}_{jj} \end{bmatrix} \begin{Bmatrix} \mathbf{x}_j \end{Bmatrix} = \begin{Bmatrix} \mathbf{0} \end{Bmatrix} \quad (3.78)$$

The constraint modes are the static structural deformations caused by a unit displacement of each individual interface DOF  $i$ :

$$\begin{bmatrix} \mathbf{K}_{ii} & \mathbf{K}_{ij} \\ \mathbf{K}_{ji} & \mathbf{K}_{jj} \end{bmatrix} \begin{bmatrix} \mathbf{I}_{ii} \\ \psi_{ji} \end{bmatrix} = \begin{bmatrix} \mathbf{F}_{ii} \\ \mathbf{0} \end{bmatrix}, \quad (3.79)$$

where each column of  $\mathbf{F}_{ii}$  contains the required force to generate the unit displacement and the respective mode shape in  $\psi_{ji}$ . The resulting equation for  $\psi_{ji}$  reads:

$$\begin{bmatrix} \psi_{ji} \end{bmatrix} = - \begin{bmatrix} \mathbf{K}_{jj} \end{bmatrix}^{-1} \begin{bmatrix} \mathbf{K}_{ji} \end{bmatrix} \quad (3.80)$$

<sup>5</sup>The effort is for a reduced system with  $k$  DOFS of order  $\mathcal{O}(kn^2)$  and not  $\mathcal{O}(n^3)$  as balanced truncation methods.

Thus the complete transformation is:

$$\mathbf{x}_n = \left[ \Phi_{nm}^{C-B} \right] \eta_m \text{ respectively } \begin{Bmatrix} \mathbf{x}_i \\ \mathbf{x}_j \end{Bmatrix} = \begin{bmatrix} \mathbf{I}_{ii} & \mathbf{0} \\ \psi_{ji} & \phi_{jk} \end{bmatrix} \begin{Bmatrix} \mathbf{x}_i \\ \eta_k \end{Bmatrix} \quad (3.81)$$

Other concepts for selecting modes for the component mode synthesis are explained in [38].

Although there are advantages in using the component mode synthesis, it is often more comfortable to build only one complete FE-model and to include simple actuator models into the model, since building the model is then much simpler and less error-prone. This is especially the case if the interfaces are complex and consisting of many coupled DOFs.

## 3.5 Examples for reduced models created with the Structural Modeling Interface Toolbox (SMI)

### 3.5.1 Description of the toolbox

Within the scope of the Very Large Telescope Interferometer (VLTI) project ESO was developing the Integrated Modeling Toolbox (IMT), aiming on the integrated modeling of optical and infrared single- and multi-aperture telescopes. For the structural mechanical part of IMT the Institute of Lightweight Structures (LLB) has built the Structural Modeling Interface Toolbox (SMI), which is called interface, as it uses modal data of an FE analysis and creates a state-space model and a Simulink block as final results. SMI is designed for IMT and therefore BeamWarrior is usually used as optical modeling tool, but it is a completely stand-alone toolbox, which uses a general format of input data and therefore can also be used with other integrated modeling software packages.

The key idea of SMI is to provide an easy-to-use package to create structural models with suitable accuracy and size for complex systems with a large number of inputs and outputs and potentially a wide variety of variants. Therefore the tools preparing the model generation include controlling an FE-analysis and reading binary result files from ANSYS. Both forces and accelerations can be handled as input. Routines help to extract the required data for rigid body motions of mirrors and to define load sets according to the geometry of the FE model and allow an automatic documentation of inputs and outputs.

The toolbox provides tools for model reduction and criteria to evaluate reduced models. However, the user has to decide, whether a reduced model complies with the

demanded accuracy. The included routines are therefore intended to be used interactively via a graphical user interface.

Figure 3.4 shows the scheme of SMI. It provides an interface between commercially available FE software and IMT. There are structural data calculated with an FE software as input and Simulink models as output. To create a dynamic model of the mechanical structure, the mechanical data like mass and stiffness matrices or modal data (natural frequencies and mode shapes) are retrieved from the FE analysis. Moreover the desired output DOFs and points of application of the input forces must be defined by the matrices  $\mathbf{P}_L$  for forces,  $\mathbf{P}_B$  for base acceleration and  $\mathbf{P}_S$  for sensors and relevant outputs. The main tasks of SMI are the generation of a dynamic state-space model of the structure, reduction of the model size and evaluation of the model quality.

An additional feature of the SMI is the capability to run parametric studies on structures. Structural parameters can be varied within the toolbox and passed to the FE-software. The FEM analysis is rerun and the resulting analysis result is parsed back to SMI. Figure 3.5 shows the interactions between different SMI components. The SMI main window is a central element in the toolbox, from which the five sub-program groups are started. These groups are the control of FE-computations and parametric studies (FE Data creation), the generation of input- and output-matrices according to the FE-DOFs, the creation of a first dynamic model from the FE-results, the model reduction and evaluation and finally the creation of a Simulink block. The two program groups in the top are concerned with FE-data. The groups model creation and model condensation deal with LTI-models in Matlab. In a standard session, all five program groups are successively used from top to down as shown in figure 3.5. However, all components can be used independently – considering that some tools require results from other tools as input data. The control of FE computations

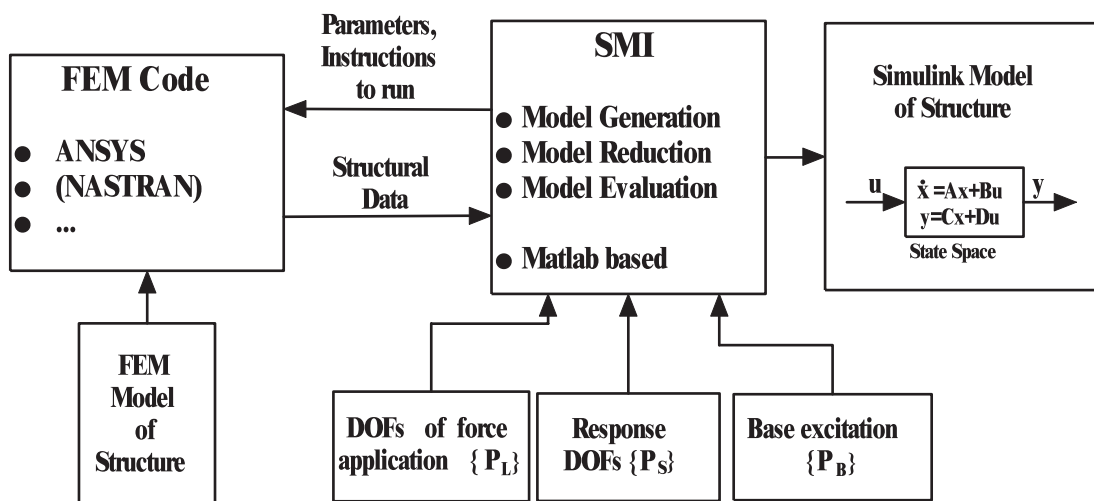


Figure 3.4: Scheme of the architecture of SMI. SMI is an interface between the FE model on the left and a final Simulink state-space model on the right.

is especially designed for the commercial FE package ANSYS. If an FE model of a mechanical structure is available, SMI directly allows to set options and calculate a modal analysis. The resulting modal data are read from the binary ANSYS result files and stored in Matlab readable format. If the FE model has been created in a parametric way, parameter variations can also be done within SMI. This parameter could be, for example, the angle of inclination of the telescope. This capabilities help a user, who is not very familiar to FE software, to create suitable modal data required as input for a dynamic model of the structure.

SMI offers different tools for the model reduction and model evaluation. In a first step the modal model can be reduced by manual selection of modes. This can be done by a user-defined frequency range, by a marginal value for the effective modal mass or by selecting individual modes. As example for the graphical user interface, figure 3.6

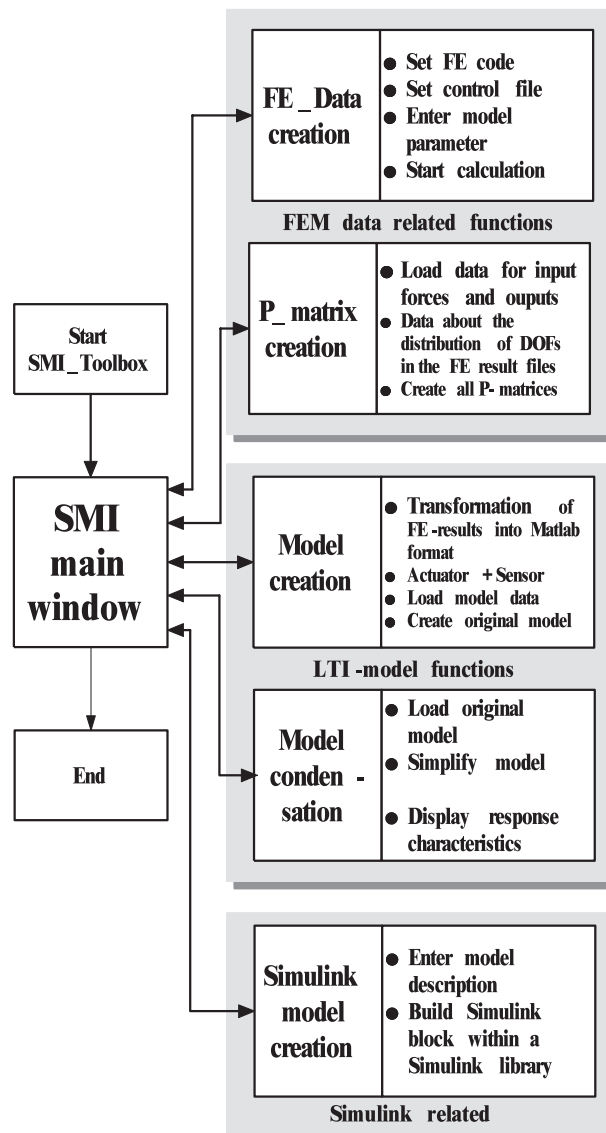


Figure 3.5: SMI architecture and components

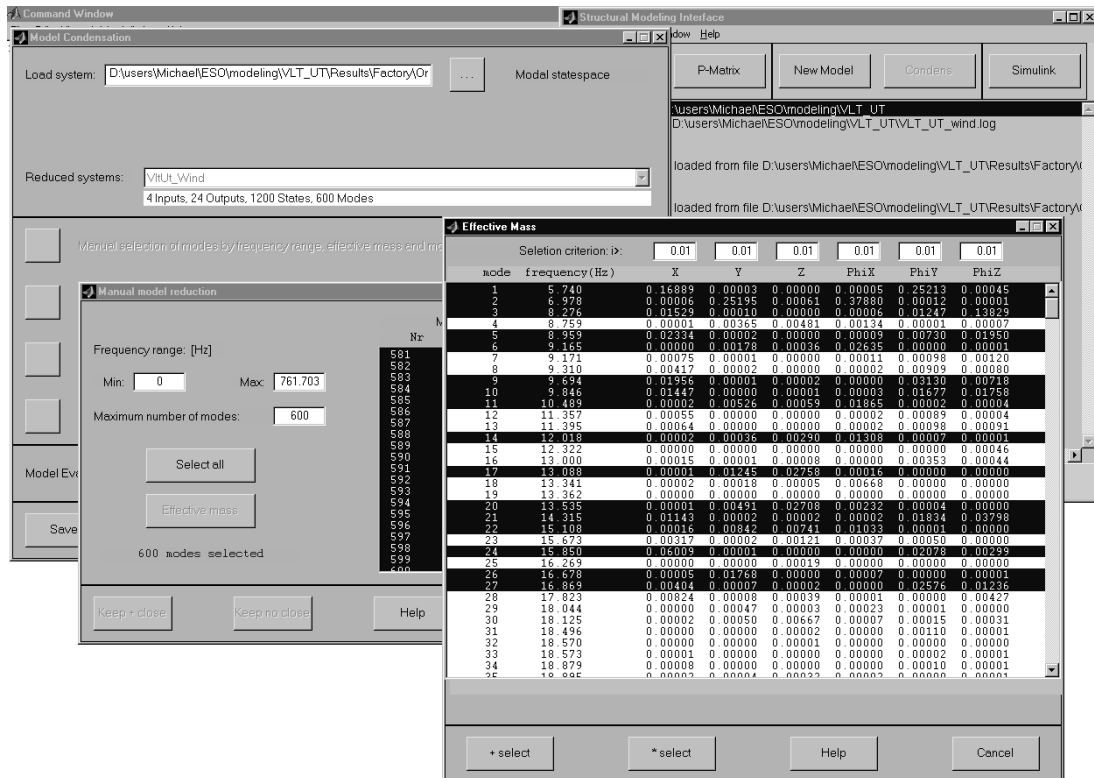


Figure 3.6: SMI provides several tools for model reduction. This figure shows the graphical user interface with a table of effective modal masses.

shows the window for model reduction based on the effective mass table. In a second stage states can be canceled by pole/zero cancellation (realization with minimal states) and by a transformation to balanced system representation with truncating the least observable/controllable modes. For the evaluation SMI provides a direct link to the LTI-viewer of the Matlab Control System Toolbox. The LTI-viewer allows to plot characteristic responses of linear time-invariant (LTI) systems in both, time and frequency domain. This includes step- and impulse-response or Bode plot and Nyquist plot of the systems. This allows directly to compare a reduced system with a full state system e.g. by the transfer functions. The LTI-viewer also calculates peak response, setting time and static gain. As a second evaluation tool, SMI allows to calculate the system response to a given input PSD. This response PSD can be compared with a reference PSD from measurements or to the response of a reference system. SMI computes root-mean-square (rms) (i.e., standard deviation) values of the output PSD in user-defined frequency ranges and the rms value of the difference between two system outputs. To get, e.g., an output with physical meaning it is possible to include a sensitivity matrix in the calculation of output and/or input. If the system outputs are, e.g., the displacements of mirrors, an optical sensitivity can be included.



### 3.5.2 Examples for reduced models

#### Dynamic model of the Very Large Telescope (VLT)

An example of applying SMI is the creation of a dynamic model of the VLT for the use in the VLTI Integrated Model. The structural model must represent the characteristic dynamics for wind load and seismic excitation.

The mechanical structure of the VLT UT is modeled in ANSYS (see figure 3.7). The FE model has 9485 elements and 38268 DOFs. Performing a modal analysis 600 modes between 5 and 120 Hz are extracted. The wind load on the VLT UT is determined analog to chapter 2.5.2. The global force field is split into four components each having different spectral distributions: the load on M1 mirror (M1), the load on M3 mirror and the M3 tower (M3), the load on the tube including center piece and Serrurier bars (TU) and the load on top unit with M2 housing, M2 spider and M2 top ring (TR) (see figure 3.7).

The optical modeling tool BeamWarrior delivers an optical sensitivity matrix of the OP and other relevant optical quantities like lateral pupil shift, Zernike coefficients to express the wavefront error, etc. of the mean ray in the focal plane due to the rigid body displacements  $\Delta x$ ;  $\Delta y$ ;  $\Delta z$  and rotations  $\Delta\phi_x$ ;  $\Delta\phi_y$ ;  $\Delta\phi_z$  of the 8 mirrors M1...M8. In this study the sensitivity matrix was calculated with an incremental

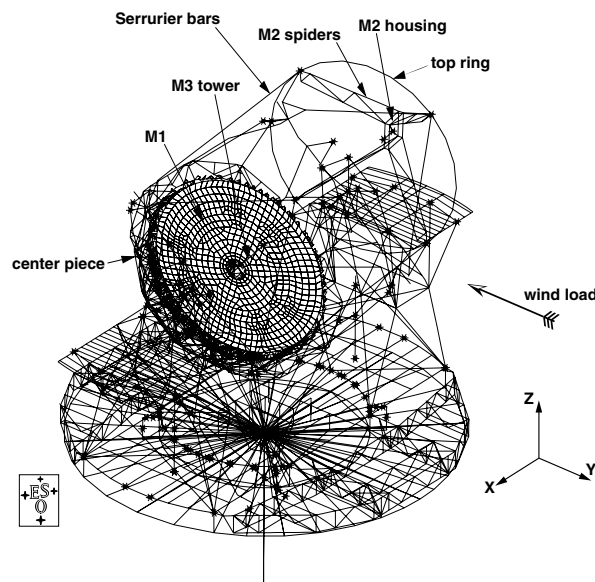


Figure 3.7: Finite element model of a Unit Telescope of the VLT. The wind blows in -y direction onto the telescope with  $40^\circ$  zenith angle. The total wind load is split into the four components M1, M3, TU and TR.

displacement of  $10^{-5}m$ . A dynamic model of the telescope structure therefore requires 48 outputs with the generalized displacements of the 8 mirrors.

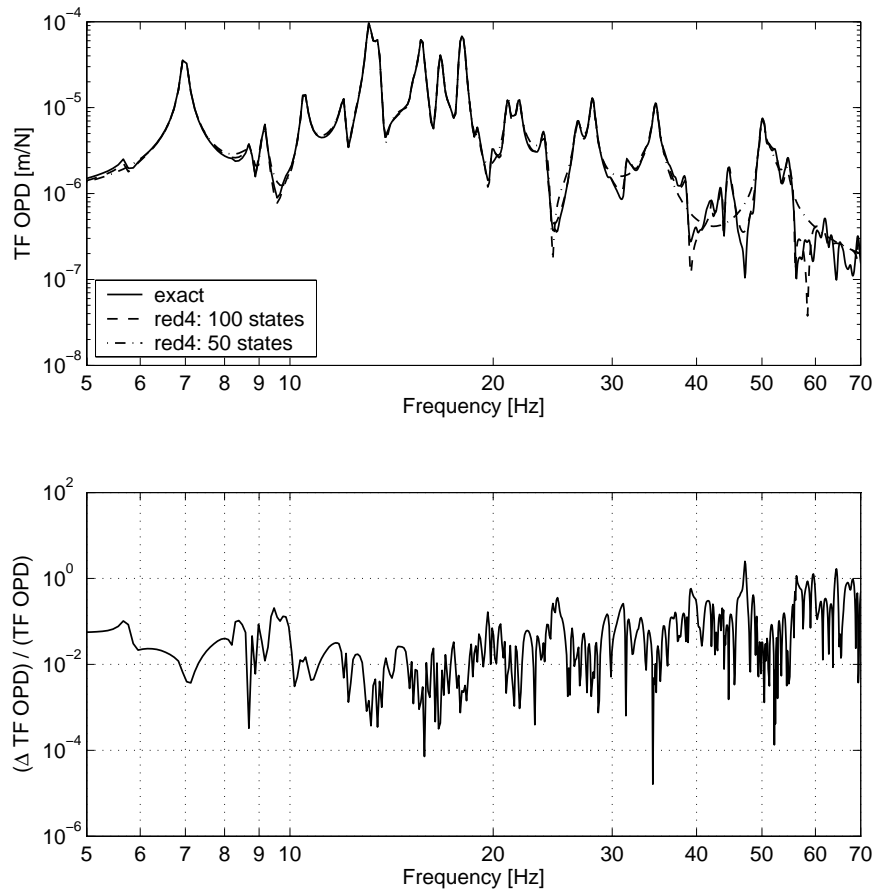


Figure 3.8: TF of the OPL due to wind load on M1: model reduction from 1200 to 100 states.

The model reduction is always a compromise between model size, which is directly linked to computational cost in a simulation, and accuracy. Figure 3.8 shows on the top the transfer function of the OPD due to the wind load on mirror M1. The full model with 1200 states was reduced to 100 and to 50 states considering only this single transfer function. The model with 100 states is in the frequency range between 5 and 70 Hz very similar to the full state model and only small differences can be seen in the higher frequency range. The resulting relative error can be seen in the plot below. The error is between 1% and 10% for frequencies lower than 20 Hz and rises than slowly up to 100%. The reason for this increasing relative error is the definition of the Gramians, which consider especially the peak amplitude of a mode and since the transfer function is falling with increasing frequency, the low order modes are most important. Contrary to the relative error the absolute error is not rising with increasing frequency. The 50 states reduced model also demonstrates this effect, as the correlation to the exact function is good for the lower frequencies and especially for the range between 10 and 20 Hz with the largest amplitudes of the transfer

function, but shows errors due to truncated modes in the frequencies larger than 35 Hz.

Keeping a model more general implies to provide a larger number of inputs and outputs. A possible example is here the general interface between structure and optics with the rigid body motions of the 8 telescope mirrors. The benefit is the modularity, which allows to use one structural model together with different optical sensitivities, which can include different outputs of one system, different configurations or different instruments.

Computing the Gramians assumes the same relevancy of all inputs and outputs and therefore they have to be scaled accordingly. To investigate these effects due to scaling inputs and outputs three different concepts for the model reduction are applied:

- a) **red1**: Direct balanced truncation without weighting of inputs and outputs for the full systems with 7 inputs and 48 outputs without considering the optical sensitivity
- b) **red2**: Considering only the wind on M1 as input and an optical sensitivity matrix, which computes the lateral pupil shift in x- and y-direction, the OPL, the tip/tilt and the defocus
- c) **red3**: Keeping all 48 outputs unscaled, but scaling the four input for the loads with a frequency dependent weighting matrix according to the expected spectrum.

Figure 3.9 shows the resulting PSDs for the OPD due to wind load on mirror M1 (left) and the absolute error of the PSDs with respect to the full state model (right). The full state model incorporated again 600 modes (i.e. 1200 states) and was each time reduced to 100 states. The model **red1** shows the worst performance, but is therefore the most general approach. The peaks of the first modes are well represented, but the model suffers from a large static error and larger errors in the frequencies with smaller amplitudes of the transfer function (between two consecutive modes). Still **red1** is a model that incorporates the main characteristics of the dynamics between 5 and 20 Hz. The two other models perform better and especially **red3** represents the low frequency range very well. This is of course caused by the frequency dependent scaling according to the wind load, which has a falling spectrum for increasing frequency. The error plots and table 3.1 confirm this.

Table 3.1: Absolute and relative rms error for the computed PSDs of the OPD between the full state model (exact) and the three reduced models.

	exact	Red1	Red2	Red3
$rms(\Delta PSD_{OPD})$	2.35e-007	1.61e-007	5.58e-008	3.35e-008
$rms(\Delta PSD_{OPD})/rms_{exact}$	0	0.68	0.23716	0.14233

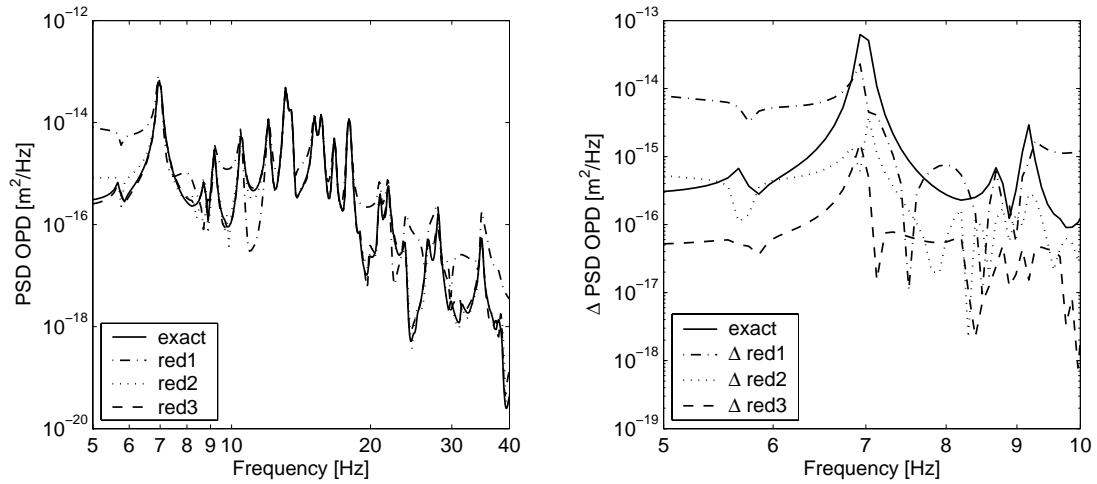


Figure 3.9: PSDs of the OPL due to wind load on M1: Comparison of the three different methods for model reduction (red1, red2, red3).

### Dynamic model of the Overwhelmingly Large Telescope (OWL)

The preliminary design of OWL of ESO envisages friction drives for both the altitude and the azimuth rotation of the telescope. This concept involves the danger of stick-slip effects due to the nonlinearity in the friction forces. A control system must provide the required forces for tracking while coping with the interaction between the friction forces, external disturbances like wind as well as the dynamics and flexibility of the mechanical structure. Moreover the dynamics of the structure are changing while tracking due to the varying spatial mass and stiffness distribution and different locations for the altitude bogies (e.g. for zenith pointing and 60° zenith angle).

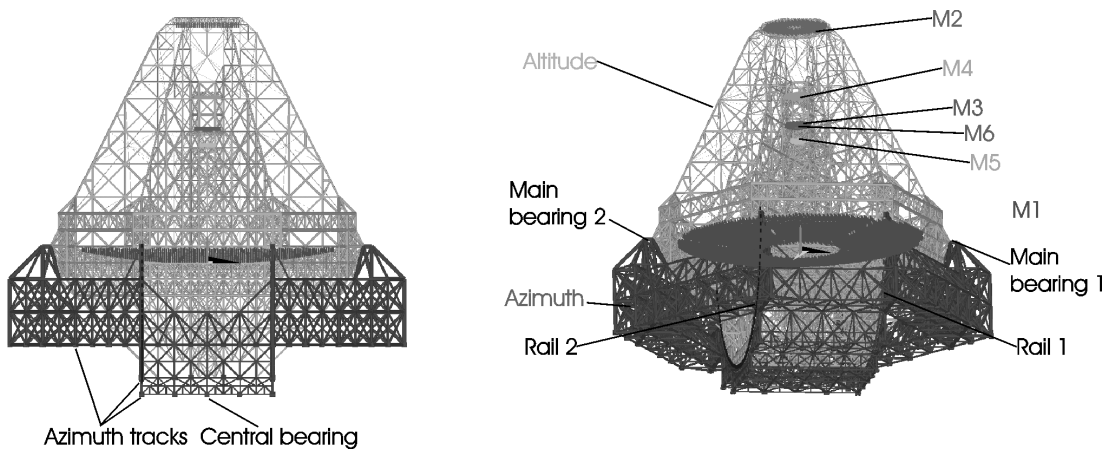


Figure 3.10: FE model of the OWL and major structural components. The azimuth structure rotates on the azimuth tracks. The altitude structure is supported with the two main bearings and two rails.

Figure 3.10 shows the FE model of OWL zenith pointing with the altitude and azimuth structure and mirrors M1 - M6. To cover all possible configurations a set of 5

different corner-stone combinations was selected. For altitude drive the frontal wind was selected as worst for zenith pointing, 30° and 60° zenith angle as the global moment around the altitude axis is the relevant quantity. As opposed to the altitude drive the global moment around the vertical azimuth axis is critical for the azimuth tracking and hence, lateral wind load for 30° and 60° zenith angle were modeled.

Modeling the wind load according to 2.5.2, the telescope was split into 14 groups. Each of the 150 altitude bogies and 250 azimuth bogies was acting with a pair of forces (in opposite directions) onto the different parts of the structure. For modeling the friction the differential displacement and velocity of each bogie and the bogie load normal onto the rail are required. In addition the rigid bogie motions of the 6 mirrors is provided with the primary mirror M1 split into 6 segments computing an average value over the respective segments. Hence a model has about 150 inputs and 350 outputs.

The FE model corresponding to the (open-loop) structural model includes lateral and normal stiffness values for the rails and bogies. The wheels were not coupled to the tracks in rail direction to simulate the open-loop condition (driving forces = 0). 800 modes were extracted from a modal analysis including one rigid body mode.

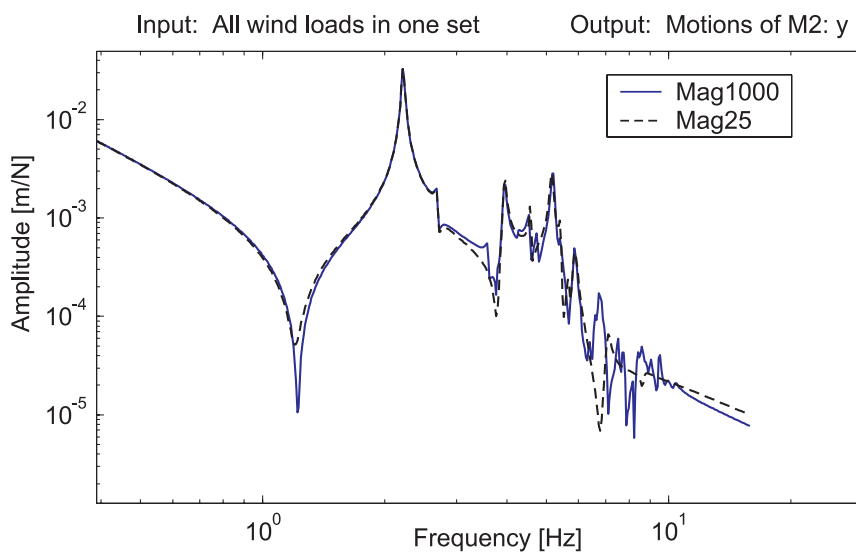


Figure 3.11: Transfer functions of wind load on OWL to the motions of mirror M2 in y-direction. Full state model (1000 states) in comparison to a reduced state model (25 states).

Figure 3.11 and 3.12 show two examples for transfer functions for a 1000 state model and a 25 state model. Figure 3.11 shows the accuracy of the reduced model for representing the motion of mirror M2 in the wind direction due to the wind load. For the friction modeling the bogie motions are required. The quality of the 25 states model can be evaluated comparing the transfer function with a full state model. As representative transfer function the differential displacement of bogie #10 is plotted due to an input of all altitude bogies with an equal force.

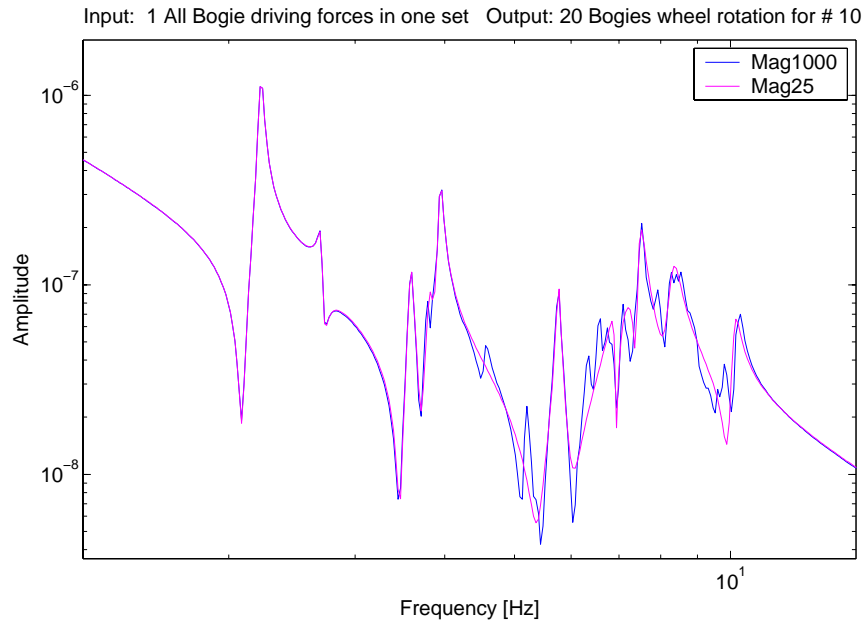


Figure 3.12: Transfer functions of the altitude drive (all bogies acting simultaneously with the same force) of OWL to the differential displacement of altitude bogie #10. Full state model (1000 states) in comparison to a reduced state model (25 states).

As opposed to these examples with good approximation results, figure 3.13 shows the transfer function of the displacement of mirror M2 in x-direction and y-direction due to the altitude drive of OWL. Since the altitude drive does not move the mirror M2 in x-direction at all, the amplitude of the transfer function is only a residual error with a very small value, whereas the altitude drive causes a real motion of M2 in y-direction. The transfer function in x-direction is much worse represented after the model reduction than the one in y-direction due to the small amplitude. However, the total amplitude in x-direction is still very small and only the relative error is large, but not the absolute one.

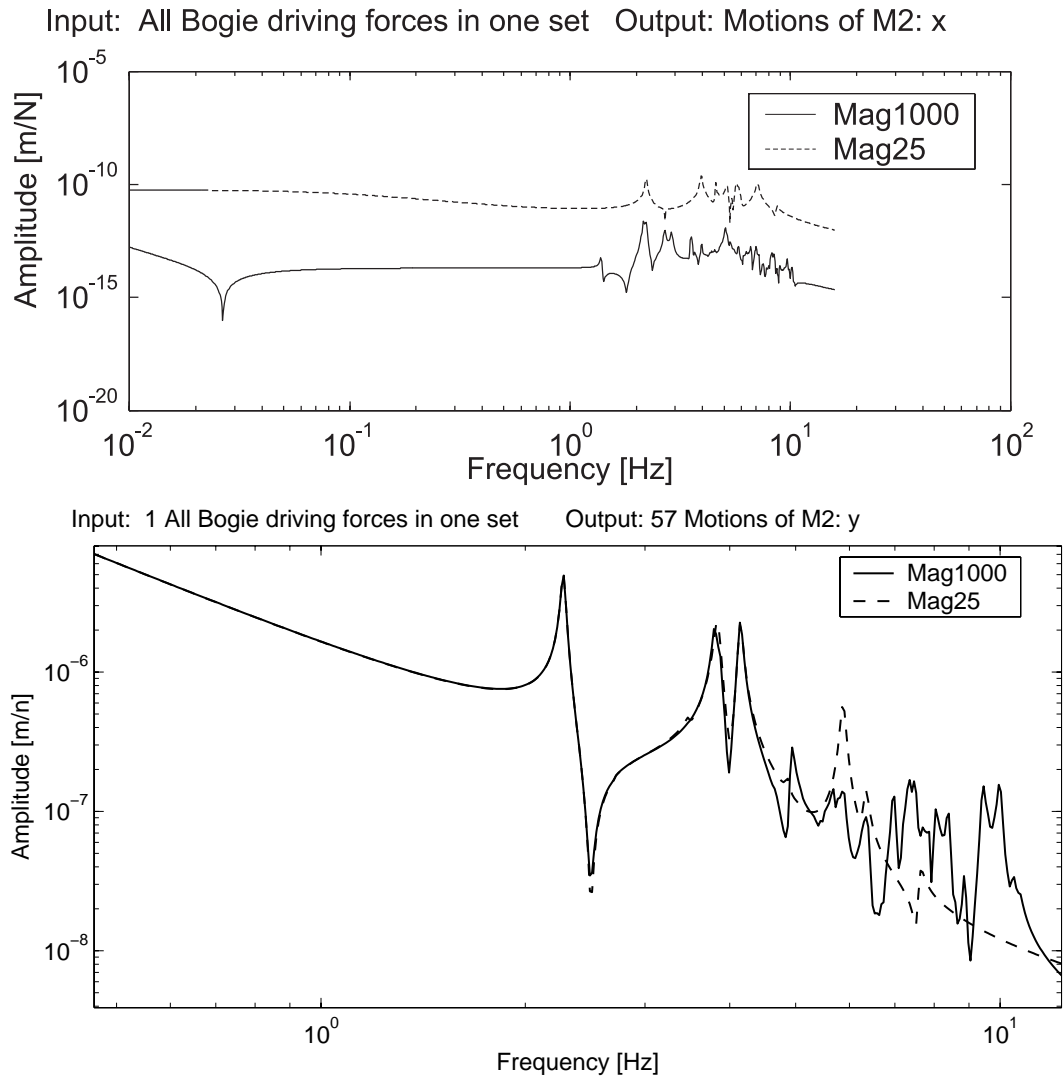


Figure 3.13: Transfer functions of the altitude drive of OWL to the motions of mirror M2 in x-direction and y-direction. Full state model (1000 states) in comparison to a reduced state model (25 states).





## 4 Solutions for selected issues in telescope structural mechanics

Accurate integrated models require also an accurate modeling of disturbances and of boundary conditions. An example of inaccuracy in the effects of disturbances are scattering material parameters. This is usually avoided by the selection of appropriate material and manufacturing technology. A best suited material for space-applications and light-weight constructions is carbon fiber reinforced plastics (CFRP) due to the extremely high specific stiffness. However, in CFRP small variations in the material properties cannot be avoided in the manufacturing process. An approach of concerning these effects is explained at the example of LOTHAR, a reflector concept for space application.

While varying material properties can e.g. cause shape errors of mirrors, the telescope dynamics is not only dependent on the mechanical structure, but also on the foundation. The impact of the ground on the telescope dynamics is usually not considered. For dynamic models of telescope structures the foundation is often assumed to be rigid. Though telescopes are frequently built on volcanic sites, where the ground can be highly inhomogeneous and of only poor stiffness due to the porosity of the volcano stone. Using the example of OWL a technic of modeling the influence of the foundation onto the telescope dynamics is explained.

### 4.1 Scattering in material parameters

Scattering in material parameters is a kind of perturbation of a system, as it has a large impact onto the effects created by external loads. To take the effects of stochastically varying parameters into account the conservative way is the worst case assumption. However, it is not always easy to define the worst case and the result does not allow to asses, which degradation would be realistic to expect.

A possible solution is a monte carlo simulation, where a larger variety of possible parameter distributions is analyzed to get a probability distribution for the effects and errors. An example for such an analysis is the reflector LOTHAR, which was designed by Astrium GmbH, Germany, as part of the space based infrared telescope in the First/Planck project.[39, 40]

LOTHAR is a sandwich construction featuring CFRP face skins and also a CFRP honeycomb core. The major advantage of using CFRP is the high ratio of Youngs modulus  $E$  to the density  $\rho$ . This allows very stiff light-weight constructions (see also chapter 2.3) with the advantage of high natural frequencies while saving mass, a main driver for space applications. Due to the manufacturing process the fiber volume fraction  $V_f$  of the face skin laminate shows some stochastic variation. Varying material quantities  $E$ ,  $\rho$  or the thermal expansion coefficient (CTE) and consequently varying local mechanical properties such as stiffness and thermal expansions are resulting. Since the manufacturing is done at room temperature and the operational temperature is at  $-210^\circ\text{C}$ , the effects of varying CTE are crucial.

Two major load cases are investigated, the first one for the cooling down from room temperature to operation temperature ( $\Delta T = -228\text{K}$ ) and the second one for a variation of the operational temperature by  $\pm 15\text{K}$ . As a worst case assumption a systematic error of 1%  $\Delta V_f$  between front skin and back skin is investigated. In the monte carlo simulation statistically variations of the  $V_f$  of front side, back side and core material of up to 0.5% are created.

For simulating the behavior of the reflector a finite element model is used. For the face skins shell elements are used and for the honeycomb core solid elements. Due to the modelling of the core by solid elements so called *smeared properties* have to be used for the honeycomb core representing the global behavior of the honeycomb structure. The front skin is composed of 828 elements, which corresponds to a spatial resolution of approximately 0.06m. The reflector is supported at three nodes on the back face skin in normal and circumferential direction relative to the plane composed

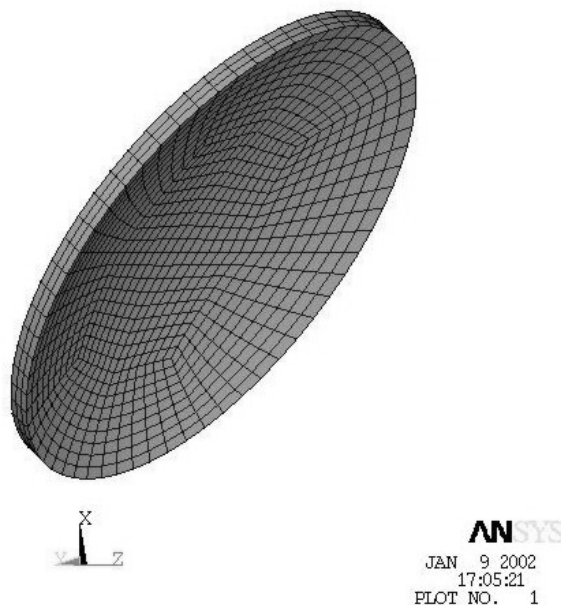


Figure 4.1: Finite Element Model of the LOTHAR reflector

of the three support points representing its isostatic characteristics. A picture of the FEM model is shown in Figure 4.1.

#### 4.1.1 Analysis setup

For this computations a flexible analysis and computation environment is set up that can easily be adjusted to geometry and configuration changes and allows to be applied to similar problems without much effort. This leads to the analysis setup shown in figure 4.2 below.

All preprocessing including geometry generation, generation of nodal and element data, computation of material properties of the face skin laminates with varying fiber content is done in MATLAB. The output of the preprocessing are the FEM-input files for the sensitivity analysis with respect to the fiber content of each element (a one by one fiber volume fraction variation of each element) for all load cases as well as scripts for job controlling on a PC cluster.

The finite element analysis is done with the FEM code ANSYS. Due to a high number of analyses required for the random analyses a PC cluster with 32 Athlon700 PCs is used. Postprocessing is then again performed within MATLAB. It includes on the one hand programs for the surface error computation, RMS calculation and fitting procedures. On the other hand the generation of the random fiber volume fraction distributions on the reflector and the corresponding analyses are performed.

The goal of the random analysis is to get information about the effects of stochastic variations of fiber volume fraction ( $V_f$ ) on the reflector performance (RMS-value). Two aspects are of special interest: one is the information about the upper limit of RMS values that may occur (*worst case*), the other one is information about the

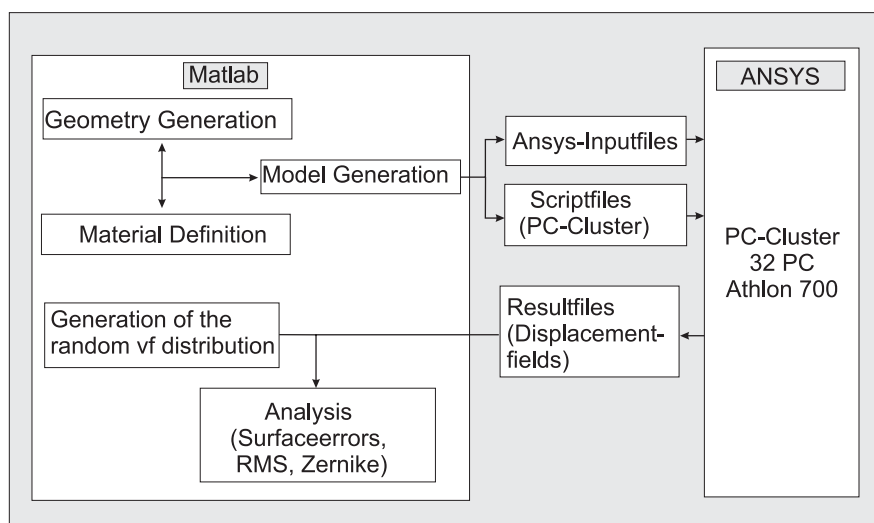


Figure 4.2: Analysis setup for the LOTHAR-reflector FEM analysis.

frequency distribution of the RMS values, i.e. how likely a certain RMS-value will be exceeded.

Due to the very own nature of random processes even for a very high number of realizations it is not absolutely sure that the worst possible distribution pattern is among the considered ones. In order to cover the whole range of possible effects with a sufficient probability, a twofold approach is chosen. On the one hand a high number of random distributions is analyzed (10.000), on the other hand the two special and conservative distributions of a uniform  $V_f$  deviation of  $\pm 0.5\%$  on the front face and a uniform  $V_f$  deviation of  $\mp 0.5\%$  on the back face (load case *Delta-p* with  $+0.5\%$   $V_f$  at the front skin and  $-0.5\%$   $V_f$  at the back skin, load case *Delta-m* vice versa). This distributions are taken separately, because they are very unlikely to occur in the random analysis and they present extreme distribution patterns, which are expected to provide an upper and lower RMS limit.

#### 4.1.2 Creation of random distributions

The most obvious method to realize the required number of random analyses is to create a corresponding number of FEM input files with a different distribution pattern each and analyze them. The disadvantage of this approach is that e.g. 10 000 random distributions require the same number of FEM analyses, i.e. the number of required FEM analyses rises linearly with the number of random analyses.

To reduce the computational costs of the required high number of stochastic analyses a different approach is chosen here:

The effects of the considered deviation of  $\pm 0.5\%$  on the material properties is linear in the considered region. A variation of  $+0.5\%$   $V_f$  results in a relative change of  $E_1$  of  $+0.9\%$  and in a relative change of  $CTE_1$  of  $-1.35\%$ .

As the resulting changes to the material properties are relatively small ( 1%) a linear approximation of the displacement field due to random distribution of  $V_f$ -variations by superposition of the displacement fields due to  $V_f$ -changes at single elements is shown to be reasonable accurate.

So first the fiber content of the face skins or core respectively is changed for a single element and the corresponding FEM analysis is performed. This is repeated for all elements of the front and back face and the core. As a result the sensitivity of the displacement field of the whole reflector for a change at that specific element (location) is computed. This results in a sensitivity matrix of the displacement field to the  $\Delta V_f$  distribution, which represents the following functional correlation:

$$\Delta \mathbf{u} = f(\text{modified element}, \Delta V_f) \quad (4.1)$$

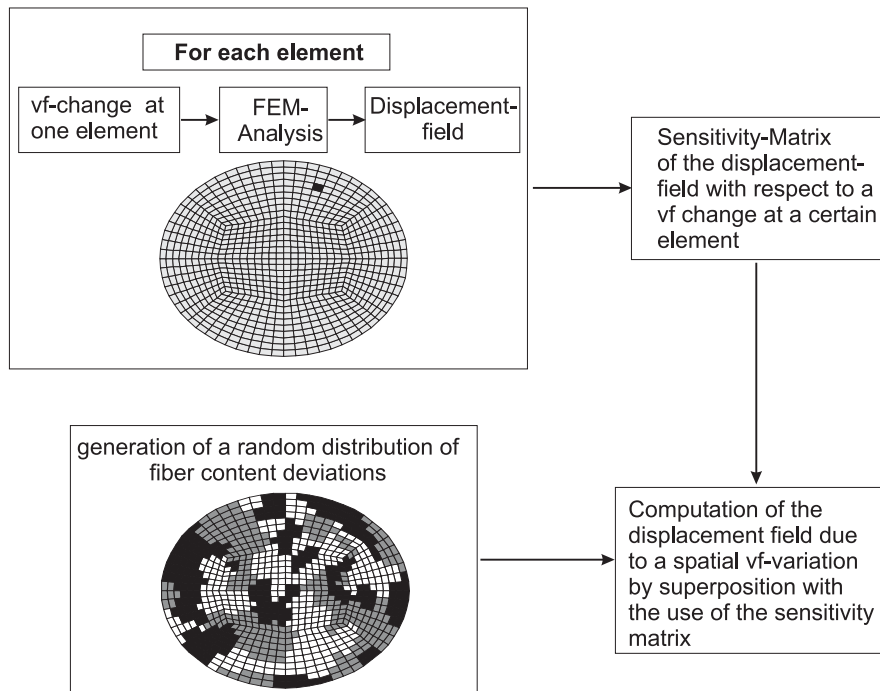


Figure 4.3: Approach for analyses with random  $V_f$  distributions

Finally for a certain random distributions of  $V_f$  variation the displacement field can be computed by superposition. With this approach the number of FEM analyses is reduced to the number of elements, no matter how many random analyses are required. The approach is also sketched in Figure 4.3.

Figure 4.4 shows examples for the sensitivity of the surface error distribution due to the change of the  $V_f$  of an individual element. The elements well inside the reflector cause only a local deformation, whereas those ones at the outer rim create a wave around the reflector with alternating surface error. However, if the respective inner

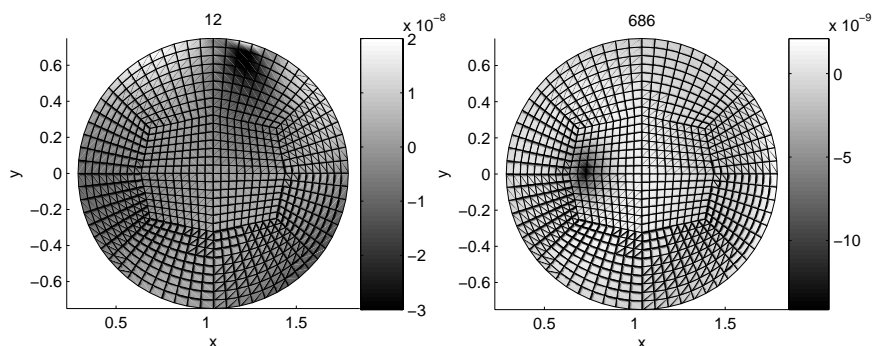


Figure 4.4: Examples for the sensitivity of the surface error distribution due to cool down from room to operational temperature. The  $V_f$  was changed by  $+0.5\%$  for the two different elements 12 and 686.

element is located at a support point, this local circular dent like deformation results in a rigid body rotation of the whole reflector and thus causes a larger total error.

For the statistical distribution of the  $V_f$  only very little measurement data are available which allow to estimate an expected peak to valley value of  $\pm 0.5\%$ , but not to derive a spatial spectrum. As a conservative approach only  $\Delta V_f$  values of  $-0.5\%$ ,  $0\%$  and  $+0.5\%$  are used. To generate a spatial random distribution first a random number of points on the face skin is chosen. To each of this points an also randomly chosen  $V_f$  deviation is assigned. Both random processes have a uniformly distributed probability increasing the likelihood of extreme distributions like a uniform  $\Delta V_f$ . Once these points are arranged, each element is assigned the  $V_f$  deviation of that point which it has the minimum distance to (see figure 4.3). With this approach various distribution patterns are covered reaching from extremes having the same  $V_f$  deviations uniformly over a whole face skin to having it only over a very small cluster of elements.

### 4.1.3 Simulation results for the load cases

#### Nominal reflector and worst cases

Due to the nominal CTE of  $6.1e-7$  1/K the reflector will significantly change its geometric shape due to cooling down from manufacturing to operational temperature (i.e., load case *Cool down* from  $18^\circ\text{C}$  to  $-210^\circ\text{C}$ ). Figure 4.5 on the left shows the resulting surface error distribution, which causes a total RMS error of  $13.03e-6$  m. However, the error is very uniform and can therefore be considered within the manufacturing by using an accordingly scaled form. The instrument and subreflector will anyway be aligned and adjusted to the reflector focus at operational temperature. Hence, the reflector can be fitted to a similar off-axis ellipsoid with moved vertex and changed elliptic parameters. After this fitting procedure the residual error diminishes practically (see figure 4.5 on the right).

As the worst configurations the two load cases *Delta-m* and *Delta-p* are chosen. In figure 4.6 the surface error distributions are displayed without fitting on the top and after optimizing location and elliptic parameters on the bottom.

Initially the *Delta-m* case results in an RMS of  $17.123 \mu\text{m}$ , which is an increase of circa  $4 \mu\text{m}$  compared to the reference case ( $13 \mu\text{m}$ ), whereas the *Delta-p* case results in reduction of circa  $4 \mu\text{m}$  smaller RMS value ( $9.811 \mu\text{m}$ ). Because of the linear behavior the *Delta-p* and the *Delta-m*  $V_f$  distributions are symmetric to the reference case. After the correction both distributions show the expected symmetry and therefore also have the same RMS value of  $0.371 \mu\text{m}$ .

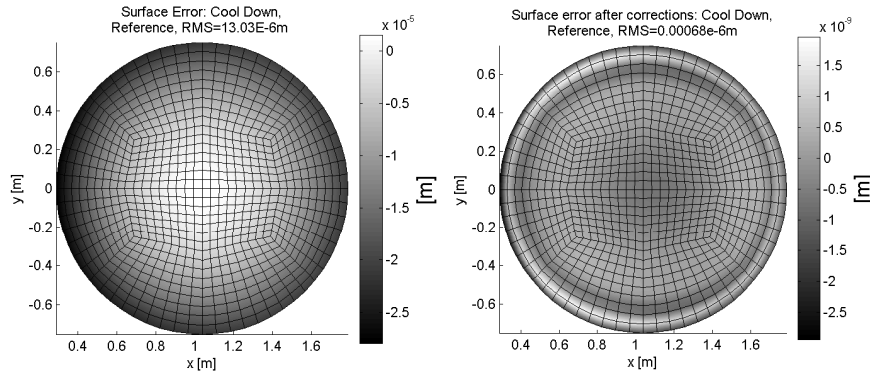


Figure 4.5: Due to the nominal CTE of  $6.1 \cdot 10^{-7}$  1/K cooling the reflector down to operational temperature causes a large surface error (left). After fitting the reflector the residual RMS is negligible (right).

### Frequency curves for the statistically varying $V_f$

For the random study 10 000 analyses with various distribution patters have been performed. In Figure 4.7 on the left the frequency distribution of the RMS value for the initial surface errors is shown. The distribution shows a symmetric pattern with a mean value of  $13.08 \mu m$  that coincides well with the RMS value of the reference case,  $13.03 \mu m$ . The standard deviation is  $0.568 \mu m$ , the maximum RMS that occurs is  $16.382 \mu m$ , the lowest RMS value is  $10.391 \mu m$ . This is still within the scope given by the *Delta-m* and *Delta-p*  $V_f$ -distributions,  $17.123 \mu m$  and  $9.811 \mu m$ . Thus as expected the *Delta* distributions prove to be the worst case distributions.

The frequency distribution of the RMS of surface errors after correction is plotted in Figure 4.7 on the right. Because there are no negative RMS values the distribution pattern is no longer symmetric around the RMS value of the corrected reference case, which was approximately  $0 \mu m$ . The mean value for this case is  $0.468 \mu m$  with a standard deviation close to  $0.125 \mu m$ . The highest RMS value that occurs is  $1.235 \mu m$ , the lowest as expected approximately  $0 \mu m$ . So for the surface errors after corrections obviously there can be random patterns of  $V_f$  deviations which prove to have a worse effect on the surface quality than the *Delta*  $V_f$ -distributions, which showed a RMS of  $0.371 \mu m$  after corrections. All in all it has to be noted that these high RMS values are very rare events that happened only once in 10.000 random analyses.

In contrast to the *Cool down* load case before, no fitting procedure is possible in the *Otp15* load case ( $T = -210^\circ C \pm 15K$ ) for minimizing surface errors, because *Otp15* is the load case at operational stage, where no further corrections or adjustments to the reflector support can be made. So the resulting initial surface errors and corresponding RMS values are those to be directly applied.

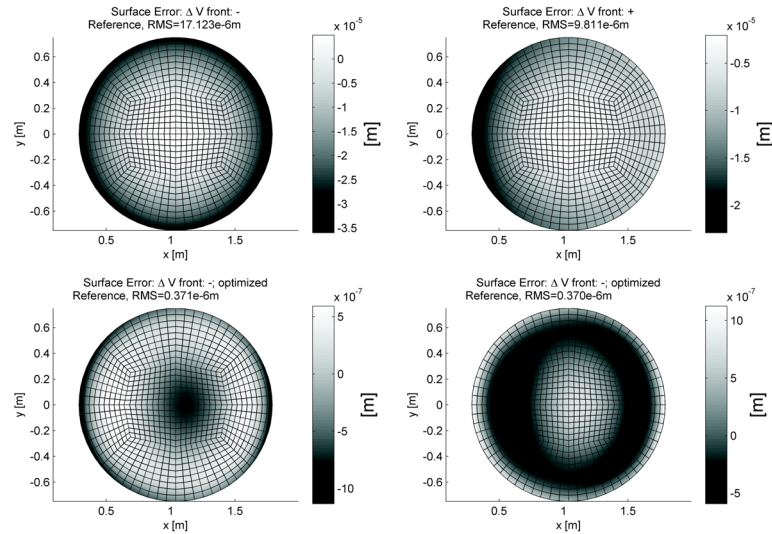


Figure 4.6: The worst case fiber volume distributions  $\Delta m$  (left) and  $\Delta p$  (right) change the deformation of the nominal reflector symmetrically (upper graphics). After fitting (lower two graphics), both cause the same residual error, but with different sign.

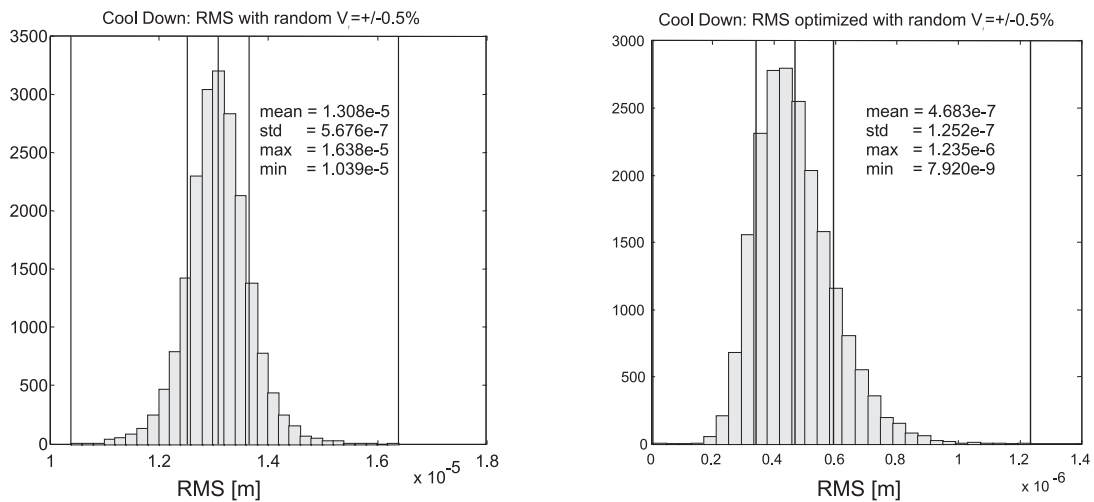


Figure 4.7: Histograms of the frequency of a certain RMS error for statistically varying  $V_f$  for the load case *Cool down*. On the left the direct results are plotted, on the right the residual RMS after fitting is shown.

In Figure 4.8 on the left the sensitivity of the RMS value of the whole reflector due to a  $V_f$ -change at single elements is shown. The RMS values are certainly not linearly related to the  $V_f$ -changes at single elements and therefore this sensitivity to the RMS value cannot be used to compute the total RMS by superposition. However, it gives an idea of the relevancy of the different locations on the reflector.

Like expected from figure 4.4 the support points are the most sensitive locations, although isostatically supported. A deviation in fiber content there will have the



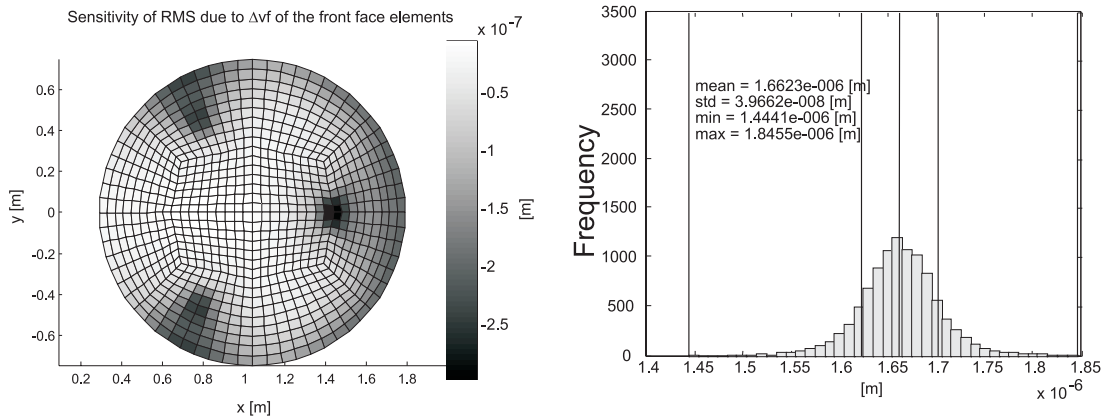


Figure 4.8: Surface error due to varying  $V_f$  for the operational load case  $OP$ . The sensitivity (left) expresses the distribution of RMS by changing  $V_f$  a single element by 0.5% (please regard explanation in the text). The histogram of the RMS error is shown on the right.

most effect on the RMS value due to the rigid body rotation that is caused by a deformation similar to local buckling near the modified element. In contrast to the CD load case here no fitting procedure is allowed, which will compensate for these rigid body motions. These rigid body motions occur mainly due to the specific modeling of the support points in this FEM model and maybe do not take place or only to a less extent with a different support structure.

In Figure 4.8 on the right the frequency distribution of the RMS values for the random distribution of fiber content deviations is shown for the  $Otp15$  load case. This time the distribution is symmetrical with the mean RMS value of  $1.662\mu m$  and a standard deviation of  $0.040\mu m$ . The highest RMS that occurs is  $1.846\mu m$ .

#### 4.1.4 Conclusion

For a non-trivial load a Monte Carlo simulation is necessary to identify the worst case. Besides worst case information the full probability density distribution e.g. for a certain surface error is generated to allow to assess the risk more reliably. However, measurement data of the varying parameters are necessary to determine an accurate distribution function for the scattering input parameters of the simulation. Due to the large numbers of simulations required to cover the worst case and to get the resulting probability density distribution, it can be more efficient to use the sensitivity of the displacement field and compute afterwards the statistical distributions from the inputs distributions and the sensitivity.

For the simulation of the LOTHAR reflector a general computational structure was developed which easily can be applied to an (nearly) arbitrary reflector with scattering material parameters. Matlab showed up to be well suited to control the computations

and generate and postprocess a large variety of parameter variations. Using a PC-Cluster is very powerful, if a high number of similar analysis runs has to be performed.

## 4.2 Dynamic effects of ground and telescope foundation

The effects of the telescope foundation are usually not included into a dynamical model of the telescope structure, although the locations of stellar observatories are often on volcanic sites with soil of only poor mechanical properties. However, what error results from assuming an infinite stiff ground (fixed supports), what dynamic effects are caused by the interaction between soil and structure and which effects have an impact onto the telescope performance? A possible approach investigating these questions is explained for the OWL telescope.

Soil shows in general a very non-linear and inhomogeneous behavior. Assuming linear properties is a simplification, which is only valid for very small amplitudes of displacements and forces. The interaction between soil and telescope means firstly a finite stiffness for the foundation, but moreover energy transport from the telescope to the ground and vice versa. Applying the FE-method only a finite domain of soil can be included requiring appropriate transmitting boundary conditions at the artificial bounds, which means a matching of the local impedance properties at the boundaries, that do not exist in reality. Many different methods for this are described in the literature (see [41, 42, 43, 44, 45]), which are different in accuracy and effort and can lead to non-local integral formulations in order to fulfil the conditions for stress and displacement along the whole artificial boundary. Besides this 'mechanical' solution of impedance matching, also a 'geometric' approach is possible increasing the material damping in the outer region of the domain to absorb the most of the energy arriving at the boundary.

The wave propagation is governed by the Navier equation of motion for the continuum (assuming the summing rule over the same indices):

$$\mu \frac{\partial^2 u_i}{\partial x_j \partial x_j} + (\lambda + \mu) \frac{\partial^2 u_j}{\partial x_i \partial x_j} + f_i = \rho \frac{\partial^2 u_i}{\partial t^2}, \quad i, j = 1, 2, 3 \quad (4.2)$$

Here  $u_i$  is the vector-type displacement field,  $f_i$  external body forces and  $\lambda$  and  $\mu$  the Lamé constants<sup>1</sup>.

Without body forces ( $f_i = 0$ ) and assuming (locally) a plane wave, where the displacement  $u_i$  depends only on the variable  $x_1$  and the time  $t$ , this gives:

---

<sup>1</sup> $\mu = G = \frac{E}{2(1+\nu)}$ ;  $\lambda = \frac{\nu E}{(1+\nu)(1-2\nu)}$

$$\frac{\partial^2 u_1}{\partial x_1^2} - \frac{1}{c_P^2} \ddot{u}_1 = 0, \quad \frac{\partial^2 u_2}{\partial x_1^2} - \frac{1}{c_S^2} \ddot{u}_2 = 0, \quad \frac{\partial^2 u_3}{\partial x_1^2} - \frac{1}{c_S^2} \ddot{u}_3 = 0, \quad (4.3)$$

where  $c_P^2 = (\lambda + 2\mu)/\rho = E/\rho(1-\nu)/((1+\nu)(1-2\nu))$  and  $c_S^2 = \mu/\rho = E/\rho/(2(1+\nu))$ . The plane wave solutions for equations (4.3) are compression waves, so called P-waves and shear waves, called S-waves with the wave numbers  $\mathbf{k}^P = \frac{2\pi}{\lambda_P} = \frac{2\pi f}{c_P}$  and  $\mathbf{k}^S = \frac{2\pi}{\lambda_S} = \frac{2\pi f}{c_S}$ :

$$u_i^P(\mathbf{x}, t) = A_i^P f_P(\mathbf{x}\mathbf{k}^P - c_P t), \quad u_i^S(\mathbf{x}, t) = A_i^S f_S(\mathbf{x}\mathbf{k}^S - c_S t) \quad (4.4)$$

The appropriate boundary condition gives the required stresses for the given displacements and velocities, while the velocity fields  $\dot{u}_i = \frac{\partial u}{\partial t}$  are similar to the strain fields  $\epsilon_{ij} = \frac{1}{2} \left\{ \frac{\partial u_i}{\partial x_j} + \frac{\partial u_j}{\partial x_i} \right\}$  and therefore, the strain fields can be expressed in terms of the velocity field with  $\psi_\kappa = \mathbf{x}\mathbf{k}^\kappa - c_\kappa t$  ( $\kappa = P, S$ ):

$$\begin{aligned} \dot{u}_i^P(\mathbf{x}, t) &= -c_P A_i^P f'_P(\psi_P) & \dot{u}_i^S(\mathbf{x}, t) &= -c_S A_i^S f'_S(\psi_S) \\ \epsilon_{ij}^P(\mathbf{x}, t) &= \frac{1}{2} \{ A_i^P k_j^P + A_j^P k_i^P \} f'_P(\psi_P) & \epsilon_{ij}^S(\mathbf{x}, t) &= \frac{1}{2} \{ A_i^S k_j^S + A_j^S k_i^S \} f'_S(\psi_S) \\ &= \frac{1}{2} \left\{ -\frac{k_j^P}{c_P} \dot{u}_i^P - \frac{k_i^P}{c_P} \dot{u}_j^P \right\} & &= \frac{1}{2} \left\{ -\frac{k_j^S}{c_S} \dot{u}_i^S - \frac{k_i^S}{c_S} \dot{u}_j^S \right\} \end{aligned} \quad (4.5)$$

The total resulting stress field is given by the sum of the contributions of the P- and the S-waves:

$$\sigma_{ij}(\mathbf{x}, t) = \sigma_{ij}^P + \sigma_{ij}^S = \lambda \epsilon_{kk}^P(\mathbf{x}, t) \delta_{ij} + 2\mu \epsilon_{ij}^P(\mathbf{x}, t) + 2\mu \epsilon_{ij}^S(\mathbf{x}, t) \quad (4.6)$$

Hence, the surface stress at the boundary can be expressed using an impedance tensor  $z_{ij}$  as:

$$T_i(\mathbf{x}, t) = \sigma_{ij}(\mathbf{x}, t) n_j(\mathbf{x}) = -z_{ij} \dot{u}_j(\mathbf{x}, t), \quad (4.7)$$

with the points  $\mathbf{x}$  on the boundary and the normal vector  $\mathbf{n}(\mathbf{x})$ .

The impedance results to  $Z = \rho c_P$  for P-waves and  $Z = \rho c_S$  for shear waves. These non-reflecting boundary conditions are also implemented in LS-Dyna ([46]), a FE-tool for time-integration of wave propagation and nonlinear systems.

This impedance condition is exactly correct, when applied at infinity and only an approximation at a finite boundary. If the radiation direction is not perpendicular to the boundary, the reflected wave increases with larger deviations from the normal direction. Modeling this equation, viscous dampers are introduced for all nodes at the outer rim.(see [41])

Besides P-waves and S-waves also other types of waves exist, e.g., Rayleigh waves. Within the modeling of the OWL foundation only P-waves and S-waves are considered,

which cause normal stress respectively shear stress. Thus two wave impedances exist,  $c_P$  and  $c_S$  and applying them to a boundary node three discrete damper elements are used acting in boundary normal direction with damping constants  $d_{ni} = \rho c_P A_i$  and in the tangential plane with  $d_{ti} = \rho c_S A_i$  where  $A_i$  is the equivalent boundary area represented by node  $i$ .

### 4.2.1 FE-model of a telescope structure including soil

The described boundary conditions are not correct for static loads since the dampers cause no forces for static loads. That is the reason why two models are considered, one with fixed boundaries and one with dampers simulating the transmitting condition.

To evaluate the dynamic performance of the OWL the transfer functions from wind excitations to the displacement of the mirrors M1 and M2 are considered.

Modeling the soil in sufficient resolution means on one hand using at least about 6 FE-nodes per wavelength. On other hand the transient boundary should be applied at least one wavelength distant from the source of radiation, in this case the telescope. The softest foundation is assumed to be crucial and thus the maximum and minimum wavelength are defined by  $\lambda_{max} = c_{max}/f_{min} = c_P/f_{min}$  respectively  $\lambda_{min} = c_{min}/f_{max} = c_S/f_{max}$ . With  $E = 500 \cdot 10^6 \text{ N/m}^2$  and  $\rho = 1300 \text{ kg/m}^3$  the wave velocities  $c_P$  and  $c_S$  are:  $c_P = 720 \text{ m/s}$ ,  $c_S = 380 \text{ m/s}$ . The frequency range to model is between 2 Hz (the first telescope mode) and 5 Hz. Therefore, the maximum and minimum wavelength are  $\lambda_{max} = 720/2 \text{ m} = 360 \text{ m}$  respectively  $\lambda_{min} = 380/5 \text{ m} = 76 \text{ m}$ . Accordingly the required resolution is  $\lambda_{min}/6 = 12.7 \text{ m}$  and the cylinder or half-sphere to be modeled of diameter  $2 * \lambda_{max} = 720 \text{ m}$ .

Figure 4.9 shows the finite element model of the OWL with the modeled soil domain. Since the most relevant mode shapes of the OWL are symmetric with respect to the symmetry plane of the telescope perpendicular to the altitude axis, only a half model is used. The resulting model consists of 70859 nodes (with 3 DOFs per node for nodes of the soil and 6 DOFs for nodes of the telescope structure). To avoid local effects at the boundaries a domain of diameter 450m and height 150m is chosen, where the OWL structure reaches 27m under ground level and approximately 170m diameter with the outermost azimuth rail. This slightly violates the conditions of required resolution and model diameter, but would otherwise lead to a much too large FE-model.

In the domain closed to the telescope several layers are included which allow to realistically represent a real existing soil according to test drills in a future investigation. At present only the general effect is investigated assuming homogeneous soil properties over the complete domain. 9 different parameters for Youngs modulus  $E$  and density  $\rho$  were selected (see table 4.1) to represent possible soils from very soft tuff stone

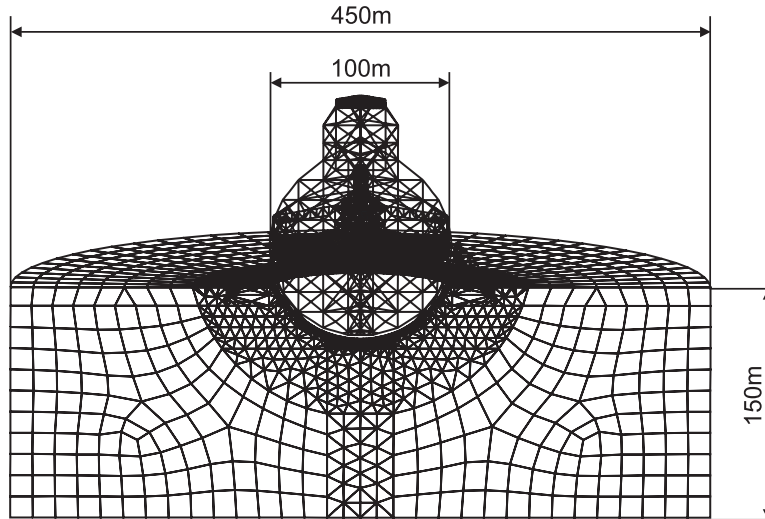


Figure 4.9: FE-model of the OWL with foundation and ground

(GroundVer1) to hard rock (GroundVer8) and quasi infinite stiffness (GroundVar9 with a Youngs modulus for the soil of five times that of steel).

#### 4.2.2 Results of the modal analysis and harmonic response

The transfer function of the wind load on the OWL to the y-displacement of mirror M1 and M2 are selected as the main criteria to evaluate the ground effects onto the telescope dynamics. To fully understand the system also static and modal results are analyzed.

Comparing the mass of the telescope to the mass of the soil to be removed for the foundation (spherical calotte) the telescope is stated to be a very light structure with

Table 4.1: List of parameters used for studying the effects of different soil properties.

#	Name	Youngs modulus $E [10^6 N/m^2]$	Density $\rho [kg/m^3]$	possible type
1	OwlGroundVer1	500	1300	tuff stone
2	OwlGroundVer2	1000	1460	
3	OwlGroundVer3	2000	1620	
4	OwlGroundVer4	5000	1780	sand stone
5	OwlGroundVer5	10000	1940	
6	OwlGroundVer6	20000	2100	
7	OwlGroundVer7	40000	2260	granite, basalt
8	OwlGroundVer8	80000	2420	granite, basalt
9	OwlGroundVer9	$10^6$	2600	quasi-rigid

only 1/3000 of the modelled mass and 1/100 of the removed mass (see table 4.2). This is the reason why the telescope has only little influence onto the dynamics of the ground.

Although the Youngs modulus of steel is much higher than that of the soft soil, the total stiffness of the telescope is much lower than the effective stiffness of the soil, since the telescope distributes its load onto a large area of ground. Table 4.3 and figure 4.10 show the effect of the static wind load onto the displacements of mirror M1 and M2. Dependent on the Youngs modulus of the soil the total displacement is changing only slightly. The stiffness of M1 with respect to wind load is higher and therefore the relative loss of stiffness is larger for M1 than for M2. The total loss of stiffness is only of the order of the effects caused by the azimuth bogies and thus is not significant.

The eigenfrequencies resulting from a modal analysis are dependent on the stiffness of the soil. Figure 4.11 shows the eigenfrequency of the first ground mode over the specific stiffness  $E/\rho$  of the ground. As expected the frequency of the first ground mode is in a good approximation rising with the square root of the specific stiffness.

The modal analysis shows three types of modes, which can be seen in figure 4.12: pure ground modes (left top), pure telescope modes (right top) and mixed modes with elastic deformations of both the telescope and the soil (left bottom). Using viscose dampers to realize the transient boundary conditions also rigid body modes occur (right bottom).

To compare the computed modes with the telescope modes with fixed supports, the Modal Assurances Criterion (MAC), the Modal Scale Factor (MSF) and the Modal Participation Factor (MPF) with respect to the wind load are computed. The MAC is a

Table 4.2: Telescope mass, mass of the modelled soil and mass of the soil to be removed due to the telescope foundation for a light soil ( $\rho = 1300kg/m^3$ )

	telescope	removed soil	modeled soil
	full model	spherical calotte	(d=450m, h=150m)
mass [kg]	13 10 <sup>6</sup>	1.1 10 <sup>9</sup>	31 10 <sup>9</sup>

Table 4.3: Influence of the soil onto the static stiffness. The values give the relative change (without sign) of displacement with respect to the quasi infinite stiff soil.

	bogies	$\Delta(E = 500; E = 10^6)$	$\Delta(E = 2000; E = 10^6)$
M1 y-displacement	3.32%	3.37%	1.02%
M2 y-displacement	1.36%	1.82 %	0.56%

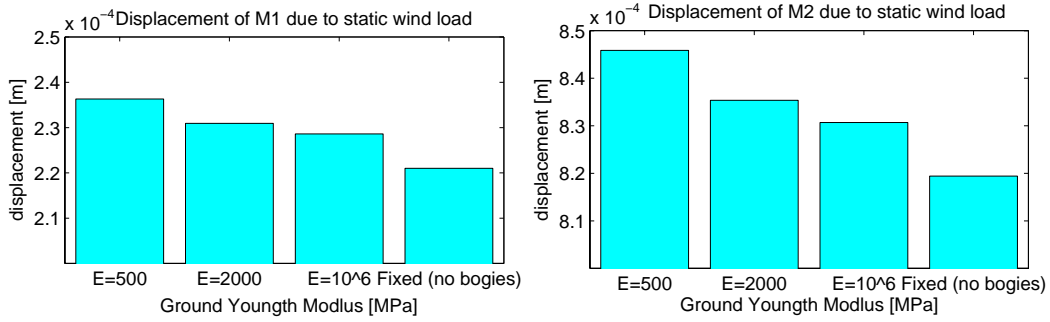


Figure 4.10: y-displacement of mirrors M1 (left) and M2 (right) due to static wind load for different stiffness of the soil. The change between the soft soil ( $E = 500MPa$ ) and the infinite stiff reference ( $E = 10^6MPa$ ) is only about 3%. For comparison the effect of the stiffness of the azimuth bogies is shown, which is also circa 3%.

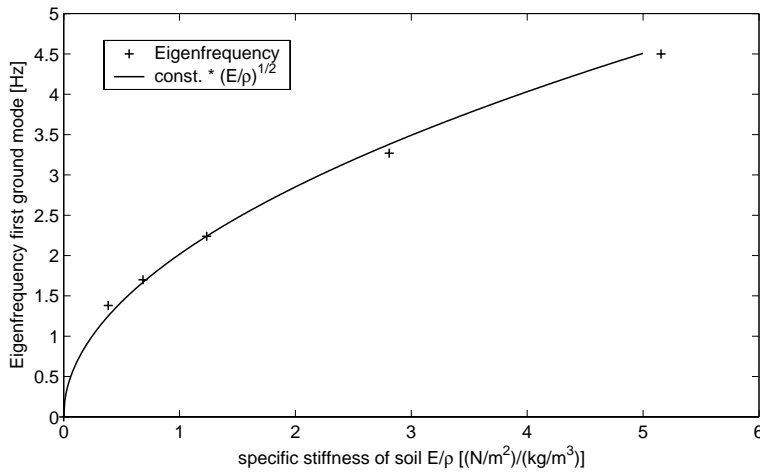


Figure 4.11: Eigenfrequency of the first ground mode over the specific stiffness  $E/\rho$  of the ground and interpolated square root function.

correlation value, which describes whether there is a linear relation between two mode shapes ( $MAC(\phi_1, \phi_2) = 1 \Leftrightarrow \phi_1 = \alpha\phi_2$ ) or if two mode shapes are completely different ( $MAC < 0.1$ ):

$$MAC(\phi_1, \phi_2) = \frac{(\phi_1^H \phi_2)^2}{(\phi_1^H \phi_1)(\phi_2^H \phi_2)}; \quad 0 \leq MAC \leq 1, \quad (4.8)$$

where  $\phi_1, \phi_2$  are two mode shape vectors and the superscript  $H$  denotes the complex conjugated, transposed vector. If two eigenvectors are similar, the MSF allows to compare the amplitudes having the value 1 if both vectors are identical. The MSF is the best fit factor of proportionality  $\alpha^2$  between two vectors:

$$^2\Delta = \min_{\alpha}((\phi_2 - \alpha\phi_1)^H(\phi_2 - \alpha\phi_1)) \Rightarrow MSF = \alpha(\Delta_{min})$$

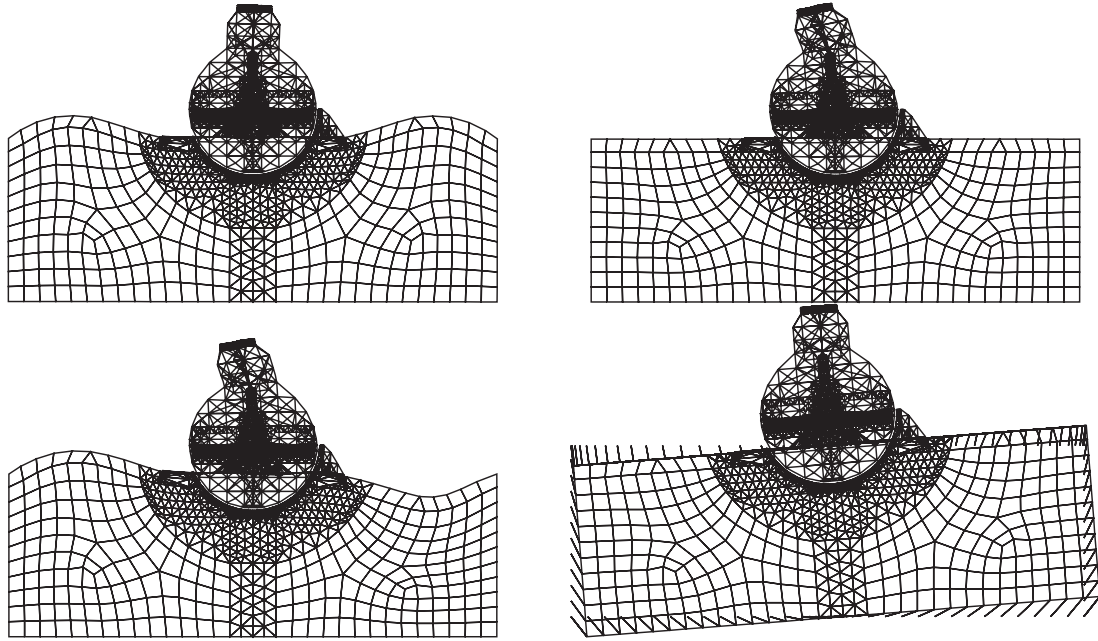


Figure 4.12: Modeling the telescope with the soil three types of modes occur: ground motion only (left top), telescope motion only (right top) or simultaneous motion of both (left bottom). The models with dampers show also rigid body modes (right bottom).

$$MSF(\phi_1, \phi_2) = \frac{\phi_1^H \phi_2}{\phi_1^H \phi_1}. \quad (4.9)$$

For the equation of motion in modal coordinates the scalar product between the mode shape and the force vector govern the degree of excitation of this mode (neglecting the frequency dependence). Therefore the MPF is also an important criterion to evaluate a mode:

$$MPF(\phi_1, f) = \phi_1^H f. \quad (4.10)$$

Figure 4.13 shows the MAC between the telescope modes and the modes of the telescope with foundations for soft soil ( $E = 500 \text{ MPa}$ : top left), medium stiff soil ( $E = 2000 \text{ MPa}$ : top right) and the quasi infinite stiff soil ( $E = 10^6 \text{ MPa}$ : bottom). Since the telescope nodes are only defined on the telescope DOFs, the MAC is applied only to the telescope DOFs not including the DOFs of the foundation and soil. ([47])

The models with soft soil have a significantly higher modal density in the region of the lower modes due to ground modes and mixed modes. Many of these mode shapes are similar to the same telescope mode. With increasing stiffness of the soil the modal density decreases and less modes are similar to the same telescope mode. The modes of the extremely stiff soil are in fact identical to the telescope modes.



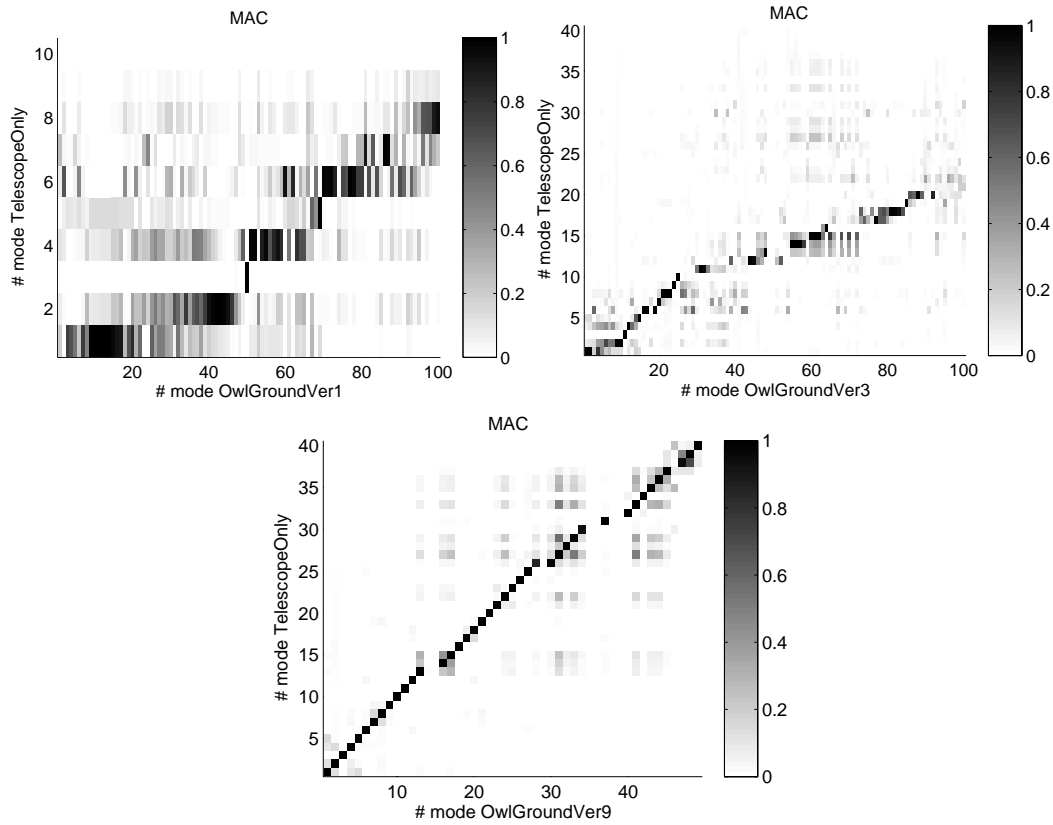


Figure 4.13: Comparison of the mode shapes with respect to the telescope on fixed supports using the MAC: For soft soil (top left:  $E = 500MPa$ ) many modes are (locally) similar to the same telescope mode. In the stiffer modes (top right:  $E = 2000MPa$ ) less ground dominated modes occur. The very stiff model (bottom:  $E = 10^6MPa$ ) contains (nearly) no ground modes, but only the telescope modes.

The existence of several modes with a shape similar to a certain telescope mode is possible without violating the orthogonality property of eigenvectors, since the similarity is only locally for the telescope DOFs. Most of the mode shapes with eigenfrequency close to a telescope mode are locally similar to this mode shape.

To analyze this in more detail for the first 19 modes of the soft model the MAC, MSF and normalized<sup>3</sup>  $|MPF^*|$  are displayed in the bar chart in figure 4.14 and for the modes with large MAC listed in table 4.5. Most of the modes 3..19 are very similar to telescope mode 1 (MAC > 0.75), the modes 9..14 have all a MAC > 0.99 and thus the identical mode shape. The MSF and  $|MPF|$  are both very similar. Only the mode 13, which is with respect to the eigenfrequency closest to the first telescope mode, has a participation factor of nearly 0.9. All the others are much less excited.

The computed eigenfrequencies of the telescope with foundation is dependent on the size of the modelled soil. To investigate this effect a model twice as large as

<sup>3</sup> $|MPF^*| = |MPF/MPF_{1,TelescopeOnly}|$

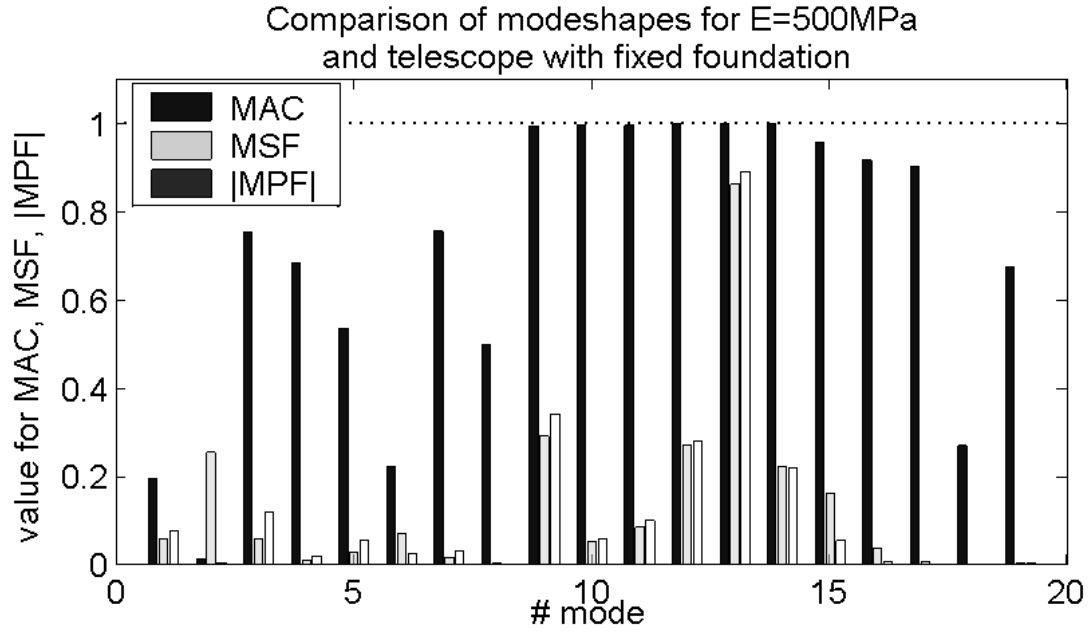


Figure 4.14: MAC, MSF and normalized  $|MPF^*|$  (with respect to the MPF of the first telescope mode with fixed supports) between the first mode of the telescope with fixed supports and the foundation model *OwlGroundVer1* with  $E = 500\text{MPa}$ .

Table 4.5: List of eigenfrequency, MAC and MSF for the modes of model *OwlGround-Ver1*, that are similar to the first telescope mode.

Mode Telescope	Mode GroundVer1	Eigenfrequency Telescope	Eigenfrequency GroundVer1	MAC	MSF
1	3	2.0769	1.3728	0.7540	0.0601
1	7	2.0769	1.7301	0.7557	0.0179
1	9	2.0769	1.9653	0.9925	0.2918
1	10	2.0769	2.0367	0.9963	0.0521
1	11	2.0769	2.0376	0.9946	0.0857
1	12	2.0769	2.0655	0.9998	0.2701
1	13	2.0769	2.0703	0.9999	0.8618
1	14	2.0769	2.0831	0.9999	0.2218
1	15	2.0769	2.2303	0.9549	0.1627
1	16	2.0769	2.2698	0.9161	0.0380
1	17	2.0769	2.3097	0.9014	0.0071
1	20	2.0769	2.4501	0.8185	0.0242

the reference was computed. Table 4.4 shows the eigenfrequencies of the first four respective ground modes of two models with ground diameters 900m respectively 450m and height 300m respectively 150m, which correspond well to the scaling laws: the eigenfrequency of the two times larger model is roughly half that of the smaller model.

Table 4.4: List of eigenfrequencies (in Hz) for the first 4 modes ( $E = 2000MPa$ ,  $\rho = 1620kg/m^3$ ).

# of ground mode		1	2	3	4
h = 300m	$\varnothing = 900m$	1.06	1.12	1.24	1.35
h = 150m	$\varnothing = 450m$	2.24	2.29	2.53	2.75

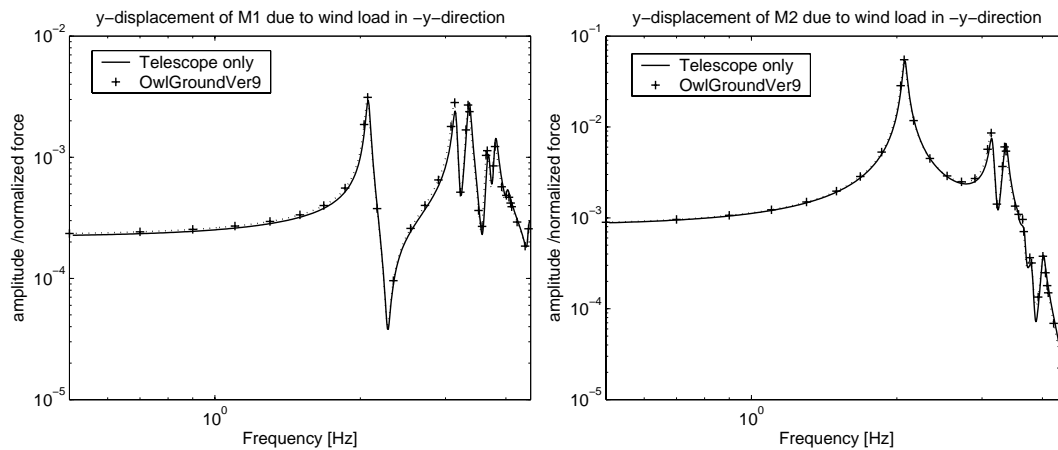


Figure 4.15: Comparison of the transfer functions between y-displacement of mirrors M1 (left) respectively M2 (right) due to wind load for the reference foundation model (*OwlGroundVar9* with  $E=10e6MPa$  and fully reflecting boundary condition) and the telescope model with fixed supports.

The decisive criteria for evaluating the effects of different foundations are the transfer functions of the mirror displacements due to the wind load. The transfer functions were computed assuming conservatively a modal damping factor of  $\zeta = 0.01$  for the models with fixed bounds and a material damping<sup>4</sup> of  $\beta = 0.0015[1/Hz]$  for the model with transmitting boundary. The material damping of the soil is certainly higher and could be assumed to be about 5%. This larger damping would further reduce the negative effects of the ground. Figure 4.15 shows the transfer function of the mirror displacements of M1 (left) and M2 (right) for both the telescope structure on fixed supports and the telescope on a quasi infinite stiff soil assuming a modal damping factor of 0.01. The transfer functions of both models are practically identical

<sup>4</sup> $\beta = \frac{2\zeta}{\omega_i} = \frac{2*0.01}{2*\pi*2.2Hz} = 0.0015$ , i.e. the  $\beta$ -damping is adjusted for the first telescope modes.

and justify together with the MAC plot in figure 4.13 to use model *OwlGroundVar9* as a reference.

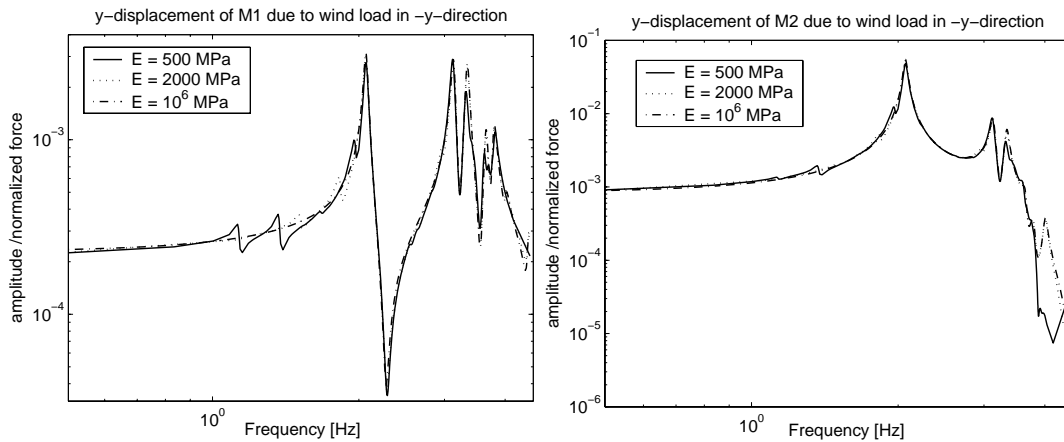


Figure 4.16: Effects of the soil stiffness onto the transfer functions between  $y$ -displacement of mirrors M1 (left) respectively M2 (right) due to wind load.

Figure 4.16 shows the transfer functions for three different types of soil: the very soft ground with  $E = 500MPa$ , the medium stiff ground with  $E = 2000MPa$  and the very stiff reference with  $E = 10e6MPa$ . The transfer functions of all three are very similar and dominated by the telescope dynamics. The main difference between the stiff reference and the softer models are, as expected, extra peaks, which occur, e.g. for the soft model, at the first ground modes (mode #1 at 1.13Hz, mode #3 at 1.37Hz) and at some of the mixed modes, e.g. mode #9 at 1.96Hz, which has a MSF of approximately 0.3 (see table 4.5). However, all in all the total stiffness of the soil is such large, that the wind load, which is only acting on the telescope structure, cannot excite these modes with a large participation of the ground to very large amplitudes, so that even the resonances of this ground modes are an order of magnitude smaller than the telescope peaks.

With increasing stiffness of the soil these extra peaks due to the ground modes are less distinct and shifted to higher frequencies as expected from the modal results. The larger differences for the frequency range above 4Hz is caused by a lack of modes computed for the very soft model, but no difference due to the model.

These effects can be seen for both the transfer function of mirrors M1 and M2. The main difference between the both mirrors is the compliance of M2, which is much higher and thus the peaks of the ground modes are even smaller compared to the peak amplitude of the first telescope mode. This effect is the very same as for the stiffness effects of the foundation.

Using these foundation models with fixed DOFs at the bounds of the modeled ground introduces an error into the transfer functions, since the energy radiated from the telescope into the foundation is propagating to the model bounds and than reflected

back toward the telescope. In reality (assuming a homogeneous soil) this energy is transported out of the system, i.e. a kind of geometric damping exists due to the loss of system energy at the model bounds. To include this effects the transmitting boundary conditions are modeled using discrete dampers.

Figure 4.17 shows the comparison of the transfer function of the soft ground with  $E = 500MPa$  for both the transmitting boundary and the fixed boundary. In either case the transfer functions are very similar. The non-reflecting boundary even reduces the influence of the ground to the response due to the wind load and the small peak close to the first telescope mode at about 2Hz even vanishes. A main difference to the model with fixed boundary are the rigid body modes and modes with much smaller eigenfrequency. The effects of rigid body modes cannot be seen in the displayed frequency range and due to the large ground mass modeled they are only relevant for much lower frequencies, where no telescope dynamics occur and thus a static analysis is sufficient. One of the lower frequency modes causes a small peak at about  $0.74Hz$ , but again the peak amplitude is relatively small as the mode is well damped due to the boundary conditions.

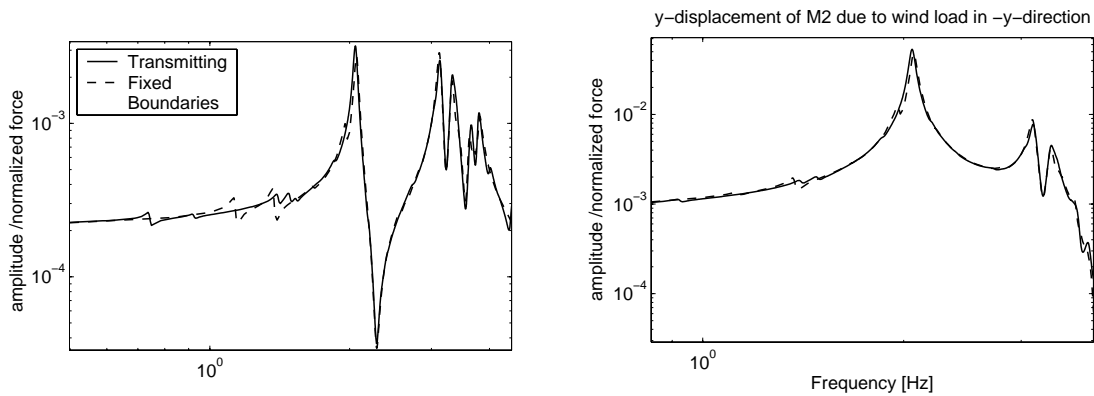


Figure 4.17: Effects of the transmitting boundary condition onto the transfer function.

### 4.2.3 Conclusion

The research of the interaction between the OWL, its foundation and the soil showed that only a small dynamic effect of the ground can be expected within the range of the material parameters under research. The main reason is the relatively light telescope structure and the large area the telescope is supported on. Thus in relation to the telescope specific stiffness the foundation specific stiffness is high and hence the total deformations are dominated by the telescope flexibility. As the telescope mass is such low, it is expected that telescope vibrations will involve only ground vibrations of a very small amplitude. Though, this implies also nearly no radiation of energy out of the telescope structure into the foundation, which would be an additional damping.

However, for a different telescope concept this could be different. Even if the telescope seems not to suffer too much under degradation of dynamic performance due to the interaction with the soil, a site with hard rock as ground material is still to be preferred as only dynamic effects are considered here and static problems with respect to the strength are not regarded. Moreover negative effects are increasing rapidly with lower stiffness of the soil.

# **5 An efficient method for integrated modeling — The example of the Very Large Telescope Interferometer (VLTI) Integrated Model**

Considering all ideas developed in the previous chapters, an integrated model is developed for the European Southern Observatory's Very Large Telescope Interferometer. Using this "real-life" example the efficiency of this approach is demonstrated.

## **5.1 Basics features of the VLTI Integrated Model**

The VLTI Integrated Model is a Matlab-based software package, which dynamically generates a Simulink model allowing time-dependent, multi-disciplinary system analysis of the VLTI. The model can be used to support VLTI system engineering, but also intends to develop concepts that can easily be applied to other telescopes like e.g. OWL.

The main characteristics of this concept is a consistent model with one configuration file, which is used to generate the optical model, select the suitable structural model and to build the complete model with all control loops and components. The model is designed using a modular approach offering a high flexibility. For all component types prototypes are stored in a Simulink library to dynamically adjust the blocks and create the model according to the configuration. This allows easily to exchange components, refine subsystems or test, e.g., different controller designs. To give the Simulink model an intuitive structure, the architecture is not only based on the control loops, but the real VLTI structure and main VLTI components are reflected. For modeling the optics a nonlinear optical analysis is done in a preprocessing phase using BeamWarrior, which provides static results and sensitivities between disturbances and optical characteristics in the exit pupil. In principle any plane or surface in the optical path can be selected to compute linear optical models (LOMs) between an input and

an arbitrary optical quantity. This is applied to include actuators and sensors, e.g. for tip/tilt control. Broad band effects can be simulated as each sensor- or instrument-band can be split into a user defined set of spectral sub-bands.

SMI (see chapter 3.5) is used to extract linear state-space models from FE-models for the telescope structure. This is not done within the preprocessing phase of the Integrated Model, but performed separately and stored for relevant telescope configurations in a directory. A strong coupling between the configuration file and a parametric ANSYS model was assessed to be inconvenient due to reducing the flexibility of changing and improving the telescope structure. Moreover this would cause a dramatic effort to adjust, e.g., the wind load to every possible configuration. Not only the points of attack will change dependent on the telescope pointing with respect to the wind direction, but also the wind profile and the mutual obstruction of telescope components.

The VLTl Integrated Model focuses on the dynamic characteristics of the interferometer and hence the main outputs are the time-dependent electromagnetic field distributions at the interferometer exit pupils in the beam combination laboratory, which can serve as inputs to a model of scientific instruments (e.g. VINCI, GENIE) performing the coherent superposition of the fields to form interference fringes. Although a detailed instrument model performing the beam combination is outside the scope of the Integrated Model, to evaluate the VLTl performance, the model allows to coherently superpose the interferometric beams after modal filtering by single-mode fibers. This is a highly nonlinear process and hence, implies high computational cost. To increase the efficiency an approximation method developed within the scope of the FINCH project (see section 5.2) by ESO and Astrium is included for modal filtering.

Major advantages of the VLTl Integrated Model are the possibility to analyze the effects of control parameters and to apply disturbances of desired level and arbitrary combination. In addition to that, the model allows to create easily linear dynamic models between any input and output for closed loop control and open loop.

## **5.2 BeamWarrior — The optical modeling tool**

BeamWarrior is a tool to generate models of the optical signal flow influenced by perturbations. Its development was initiated in 1997, driven by the lack of powerful, open-architecture optical modeling code which could easily be customized to create models for integration into a control loop simulation. The institutions which have supported the development are Astrium EADS, Friedrichshafen, Germany, ESO and the German Aerospace Center (DLR). Present and future work is done in an ESO-Astrium team. In the framework of an ESA Technology Research Programme, BeamWarrior is used to develop an integrated model (FINCH) of the spaceborne nulling interfer-



ometry mission *Darwin*. The FINCH project is currently in its Phase II concentrating on the implementation of extended astronomical sources.

The *BeamWarrior Kernel* is a library of ANSI C functions for optical modeling which can be accessed either by a custom C application or via the *BeamWarrior Optical Modeling Tool*. The latter is a general-purpose application which reads a sequence of computational steps to be performed and the results to be produced from an ASCII “control file”. The *Optical Modeling Tool* has been designed for flexible generation of linear optical models (i.e. sensitivity matrices). Besides its main purpose, namely the creation of dynamic optical models, *BeamWarrior* can also be employed for a large variety of static optical analysis tasks. Examples can be found in the references.

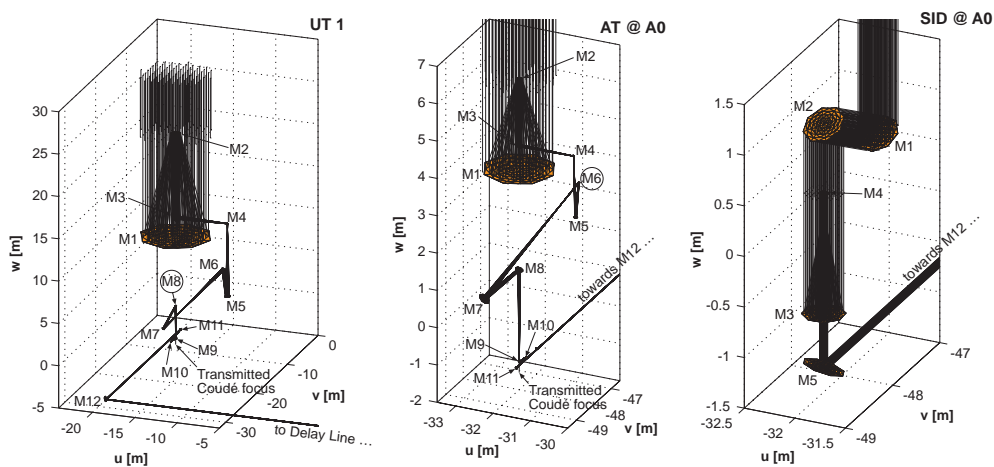


Figure 5.1: *BeamWarrior* models of the three types of VLT telescopes (left to right): Unit Telescope (UT), Auxiliary Telescope (AT) and Siderostat (SID); the encircled mirror labels “M8” (UT) and “M6” (AT) indicate mirrors onto which a pupil (= image of aperture stop M2) is located. For the UT and AT, an image of the star is located in the transmitted Coudé focus below the dichroic mirror M9 and in the reflected Coudé focus on the field mirror M10. Note the different scales of the three plots.

Light propagation is simulated by geometrical- or wave-optical methods which can be flexibly combined in a “hybrid propagation model”. The geometrical-optical domain is covered by a radiometric polarization ray tracing algorithm. Wave-optical (diffraction) propagation is handled by three alternative approaches, each being suitable for specific cases: (1) the “direct method” based on numerical approximation of the Rayleigh-Sommerfeld integral, (2) the “angular spectrum method” using a decomposition of the optical field into a set of homogeneous and evanescent plane waves, and (3) the Gaussian beam decomposition technique which can be used to simulate an “end-to-end” wave optical propagation —from the incident wavefront to the detector. In addition to these free-space propagation algorithms, the tool can also simulate the modal filtering of an optical field by coupling into a single-mode step-index fiber.

All Kernel algorithms consider polarization effects and are radiometrically calibrated. BeamWarrior allows to compute optical signals in a broad spectral range. This is handled by sequentially computing the result in adjacent narrow spectral sub-bands. Wavelength-dependent material properties are stored in a specific material catalogue. Electric fields at the output of different arms of a stellar interferometer can be superposed coherently. A description of some of the algorithms can be found in the references.[5, 48]

Within the VLTI Integrated Model BeamWarrior is used for the optical modeling. Examples for the modeling of the three different telescope types Unit Telescope (UT), Auxiliary Telescope (AT) and Siderostat (SID) are shown in figure 5.1. Light from an unresolved, infinitely remote celestial point source is arriving at the telescope and propagated through the telescope optics including Coudé train and relay optics, transfer optics, Delay Line and laboratory beam compression/feeding optics.

Figure 5.2 shows the resulting spatial distribution of electric field amplitude and phase in the exit pupil plane of a VLTI interferometer arm. Moreover BeamWarrior allows to generate optical sensitivity matrices by applying defined perturbations to optical components like a mirror displacement and evaluating the deviations from the output quantities for nominally aligned optics. As explained later, this results are used as the basic quantities for the linear optical model.

A more general type of optical model is the non-linear optical model. It is adequate if the changes in optical output parameters of interest are not proportional to the applied perturbations, e.g., in the case of large-scale perturbations. In such a case, a BeamWarrior computation must be performed at every time step of a dynamic simulation. A usage of this kind of models is not planned in the VLTI Integrated Model.

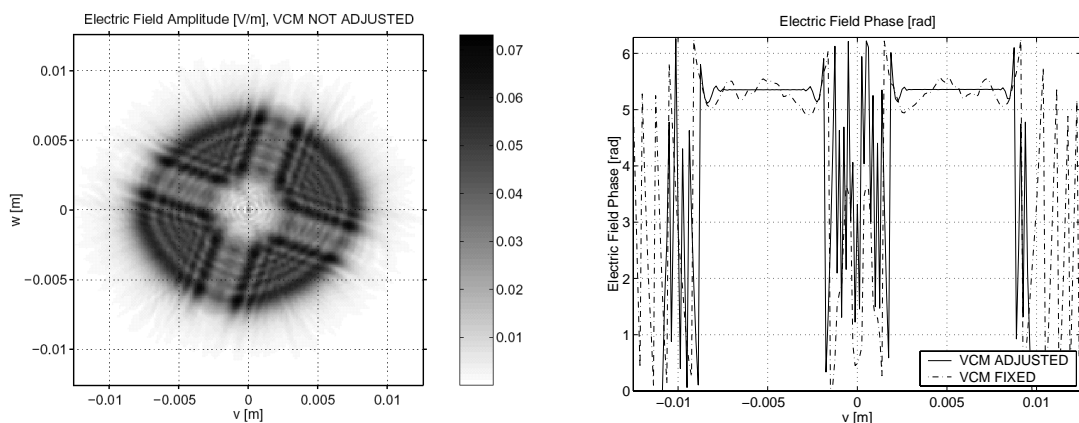


Figure 5.2: Amplitude (left) and phase (right) of the electric field distribution in the nominal exit pupil (parallel to  $(v, w)$ -plane, diameter 18 mm) of a VLTI interferometer arm (Siderostat telescope,  $\lambda = 2.2$ , point source magnitude  $m_K = -6$ ).

## 5.3 Architecture and design of the VLTI-Integrated Model

The Integrated Model of VLTI represents the main control loops of the interferometer and includes most relevant disturbance sources. At current background radiation, internal tilt and adaptive optics are not include. The format of its outputs is in Matlab format, but routines are provided to store data in the format of the "real-world" VLTI (i.e. Flexible Image Transport System (FITS)).

### 5.3.1 Computing the dynamic interferometer response

The integrated model computes the response of VLTI to a point source (unresolved, infinitely remote) observed on axis. The incident wavefront is an homogeneous (i.e. constant intensity) plane wave. Radiometrically, the source is characterized by its apparent magnitude in a given spectral band (e.g. K-band). Light propagation is simulated splitting the spectral band into a set of sub-bands. Each sub-band is represented by a single wavelength equal to the center wavelength of the sub-band. The point source is assumed to be naturally polarized.

The main output of the model is a complete description of the time-dependent electric field in the exit pupil of each interferometer arm ("time-dependent pupil function"). For computation of the dynamic electric field distributions the method described in [49] is used: The complex electric vector field  $\mathbf{E}_i^{Pol}(\mathbf{x}, t)$  at the exit pupil of arm  $i$  is given by the product of a static complex vector field  $\mathbf{E}_i^{Pol}(\mathbf{x})$  and a time-dependent phase factor  $\exp(j\Delta\phi_i(\mathbf{x}, t))$ :

$$\mathbf{E}_i^{Pol}(\mathbf{x}, t) = \mathbf{E}_i^{Pol}(\mathbf{x}) \exp(j\Delta\phi_i(\mathbf{x}, t)) \quad (Arm\ i, Pol = s, p). \quad (5.1)$$

where the superscript  $Pol = s, p$  denotes the two uncorrelated orthogonal polarization components of the naturally polarized source,  $t$  the time and  $\mathbf{x} = (v, w)$  a two-dimensional position vector in the exit pupil (compare Figure 5.2). The dynamic "phase error"  $\Delta\phi_i(\mathbf{x}, t)$  arises from fluctuations of the optical path in the exit pupil with respect to the nominal situation. As the displacements of optical elements due to disturbances and active control are sufficiently small the resulting phase error can be regarded as polarization-independent, i.e. the *same* phase factor applies to all Cartesian components of  $\mathbf{E}_i^{Pol}$ . The phase error is linked to an "optical path error"  $\Delta OP(\mathbf{x}, t) = \lambda/(2\pi)\Delta\phi_i(\mathbf{x}, t)$  which itself can be expressed as decomposition into  $N$  orthogonal Zernike polynomials  $\psi_m(\mathbf{x})$ :

$$\Delta OP(\mathbf{x}, t) = \sum_{m=1}^N \delta\xi_m(t)\psi_m(\mathbf{x}) \quad (5.2)$$

The  $N$  time-dependent coefficients  $\delta\xi_m(t)$  are the deviations of the  $N$  Zernike coefficients from the static situation. In addition to dynamic phase errors, the model also takes dynamic pupil motion into account.

As stated above, the method described computes the response to a point source. However, for linear and space-invariant (isoplanatism) systems the formalism can be extended straightforwardly to simulate observation of extended objects (see Schöller et al 2000 [49]) using a Fourier-optical approach, where an extended source is computed from the image of a point source convolved with the visibility function of the source. This method is not applicable for modeling a modal filter like a single-mode waveguide, since changing the location of the source causes a change in the amplitude and not the location of the intensity pattern at the fiber output (see sections 5.3.3 and 5.3.4).

### 5.3.2 Model architecture

The architectural design of the VLTI integrated model covers up to eight interferometer arms (in single-feed mode). Each arm is equipped with a “photon collector” (Unit Telescope (UT), Auxiliary Telescope (AT) or Siderostat (SID)) and a DL. For a system description of the VLTI the reader is referred to *Glindemann 2004*. [50]

The model uses a three phased approach: During the *initialization phase*, user-defined parameters are set (e.g. array configuration, source characteristics and angular position, disturbance and control loop parameters, simulation time and sampling). BeamWarrior performs the two tasks: (i) compute the static electric vector fields  $\mathbf{E}_i^{Pol}(\mathbf{x}, t)$  for all interferometer arms ( $i = 1 \dots i_{max}; i_{max} \leq 8$ ) and both star polarizations ( $Pol = s, p$ ), and (ii) generate the linear optical models (sensitivity matrices) needed for the dynamic simulation.

The *dynamic simulation phase* is the core of the integrated model. It is implemented as a Simulink model. A Simulink block diagram with multiple levels representing the different subsystems is dynamically generated to match the chosen array configuration.

In the *post-processing phase* the results of the dynamic simulation are combined with the static results obtained in the initialization phase. A simplified model of the VINCI instrument can be include already into the simulation phase computing the interference fringes assuming pupil-plane beam combination with a temporal optical pathlength modulation scheme. Alternatively, another instrument model could be used in a future version.

### Control loops

The VLTI Integrated model represents three main control loops relevant for the dynamic telescope performance: the *fringe tracking loop*, the *fast tip/tilt loop* and the *lateral pupil position control loop*. Since the model focuses on the dynamic performance, quasi-static control loops like the active optics compensating for thermal disturbance and varying gravity load or the control system for pointing and tracking are not included.

The *fringe tracking control loop* forms the central control loop of the VLTI. It defines the top-layer of the model architecture as shown in Figure 5.3. The objective of this control loop is to compensate for the (temporarily varying) optical path difference (OPD) between two interferometer arms. Figure 5.4 depicts the block diagram of the subsystem “Fringe Tracking” appearing in Figure 5.3. The measurement of the OPD is performed by a Fringe Sensor Unit (FSU) located in the beam combination laboratory. The stellar light is shared between FSU and scientific instrument (e.g. VINCI). In general, instrument and FSU operate in different spectral bands. Therefore the light is split by use of dichroic feeding optics. The OPD Controller (OPDC) converts the measured OPD into a command passed to the DL (carriage + Piezo actuator). Optionally, an additional OPD modulation command can be sent in case of pupil plane beam combination. The fringe tracking control loop is present for all three types of photon collectors (UT, AT and SID). Currently, we have implemented a model of the FSU FINITO which is currently being commissioned on the VLTI. The DL model is a discrete linear state-space model identified from measurements on site.

For UTs and ATs the *fast tip/tilt loop* compensates for wavefront tip/tilt induced by wind load and atmospheric turbulence. The tip/tilt error is derived from measuring the image position at the transmitted Coudé focus (below the dichroic mirror M9) (see Figure 5.1). An integrator provides a correction signal to an active mirror (M2 for UT, M6 for AT) which can be actuated in two DOFs (tip/tilt). The tip/tilt control is not available on a SID. Within the model, the image position is computed as spot

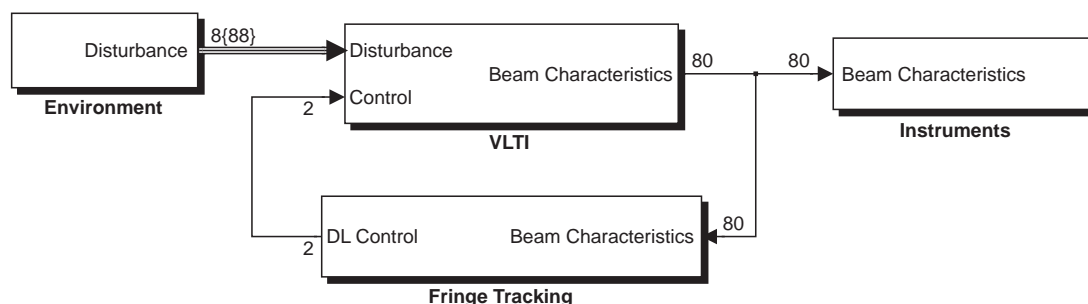


Figure 5.3: Top-level architecture of the VLTI Integrated Model; the labels attached to the signal flow lines correspond to a two-aperture configuration (see Section 5.3.2)

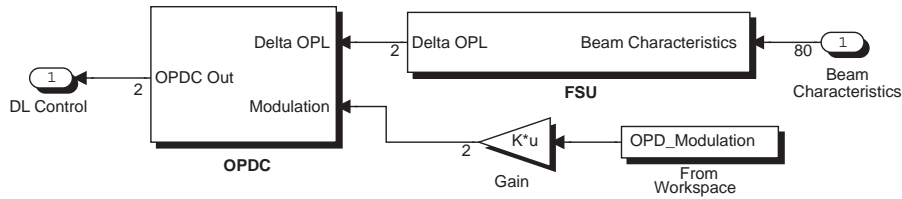


Figure 5.4: Sensor (FSU) and controller (OPDC) of the fringe tracking control loop; each interferometer arm has its own plant model (Delay Line (DL)) (see Figure 5.6). The labels attached to the signal flow lines correspond to a two-aperture configuration (see Section 5.3.2).

diagram centroid using a BeamWarrior linear optical model for the beam train through the telescope optics (M1...M3), Coudé train (M4...M8) and M9.

This *lateral pupil position control loop* (UT and AT only) corrects the lateral position of the exit pupil in the beam combination laboratory. The measurement is taken in the laboratory and fed back to the field mirror M10 which can be actuated in two DOFs (tip/tilt) (see Figure 5.1). Within the model the lateral pupil position is computed using a BeamWarrior linear optical model for the beam train through the whole VLT optical train up to the instrument entrance (telescope including Coudé train and relay optics, transfer optics, DL, laboratory beam compression/feeding optics). The “real” VLT does not provide closed-loop control of lateral pupil position (realized by a zero feedback gain in the model). Instead of this, the exit pupil is centered on a CCD matrix by an automatic alignment system before each observation run.

Figure 5.6 displays the block diagram of a single UT interferometer arm. The signal flows of both tip/tilt loop and lateral pupil position loop are fully contained in the subsystem since these two control loops act independently on each VLT arm. In contrast, the fringe tracking loop controlling the OPD *between* different arms is implemented on the top-most level of the model. For a description of the signal representations, see Section 5.3.2.

### Modeling of the disturbances

The model considers the following environmental disturbances: wind load, micro-seismic excitation and atmospheric turbulence. Currently wind load and micro-seismic excitation are simulated for UTs only. Moreover the piston term of the internal turbulence inside the DL tunnel is added to the respective OPLs and white noise terms are added to sensors and actuators like the Fringe Sensor Unit or the DL.

The *wind load* acting on the telescope (structure & optics) is modelled using the model as described in section 3.5.2 with four different load cases.

The *seismic motion of the ground* is simulated by measured PSDs of typical ground acceleration at Cerro Paranal (see chapter 2.5.2). The ground acceleration PSD is converted into a random time series serving as further input to the structure model—in addition to the dynamic wind forces.(see Appendix A)

*Atmospheric turbulence* creates temporal and spatial fluctuations of the phase of the electric field of each interferometer beam (see chapter 2.5.3). In current version the three lowest order modes (piston and tip/tilt) are computed using analytical expressions of their PSDs based on Kolmogorov statistics (see equations (2.30)-(2.33)). The correlation between atmospheric piston on two telescope apertures separated by a given baseline is simulated. The PSDs are converted into random time series. Higher-order modes are represented by time-varying Zernike coefficients. These are extracted from moving phase screens independently computed for each aperture. Piston is (partially) corrected by the fringe tracking loop. Tip/tilt is compensated by the fast tip/tilt control loop. The higher-order modes remain uncorrected (assuming the absence of an adaptive optics system) and are directly added to the electric field distributions at the exit pupils in the beam combination laboratory.

### Representation of the signals

In the dynamic simulation, each interferometer beam is characterized by its *beam characteristics state vector*  $\mathbf{z} = (\delta v, \delta w, \delta OPL, \delta \xi_1, \dots, \delta \xi_N)^T$ . The components  $\delta v$  and  $\delta w$  are the deviations of the exit pupil center from its static position (measured in the  $(v, w)$ -plane in the beam combination laboratory, see Figure 5.2). The dynamic wavefront aberrations are encoded in a set of Zernike polynomials with coefficients  $\xi_i$  ( $i = 1 \dots N$ ;  $3 \leq N \leq 37$ ) (see equation (5.2)). The Zernike decomposition uses a normalization radius which is assumed to be constant.

Figure 5.5 shows schematically the signals for one spectral band of one arm. The external inputs for the state-space model of the telescope structure are the four load cases for wind excitation and the three ground accelerations for micro-seismicity. The resulting vibrations of the eight mirrors are provided to the optical model with six rigid body motions per mirror. The optical model is a linear sensitivity matrix computing from this mirror disturbances the lateral pupil shift, the OPL of the so called Chief ray (i.e. the ray in the center) and the Zernike coefficients in the exit pupil. The atmospheric turbulence is directly expressed in Zernikes and is therefore directly fed through the telescope to the exit pupil. Together with the static electric field, these time-dependent deviation give the dynamic electric field in the exit pupil.

The state vector  $\mathbf{z}$  has the size  $(3 + N) \times 1$ , i.e.  $40 \times 1$  for  $N = 37$ . This is reflected in the labels attached to the signal flow lines in the Simulink block diagram of the single interferometer arm shown in Figure 5.6. The block diagrams showing the top-level architecture (Figure 5.3) and the fringe tracking loop (Figure 5.4) represent an array configuration with two apertures. Their beam characteristics signal flow lines (label

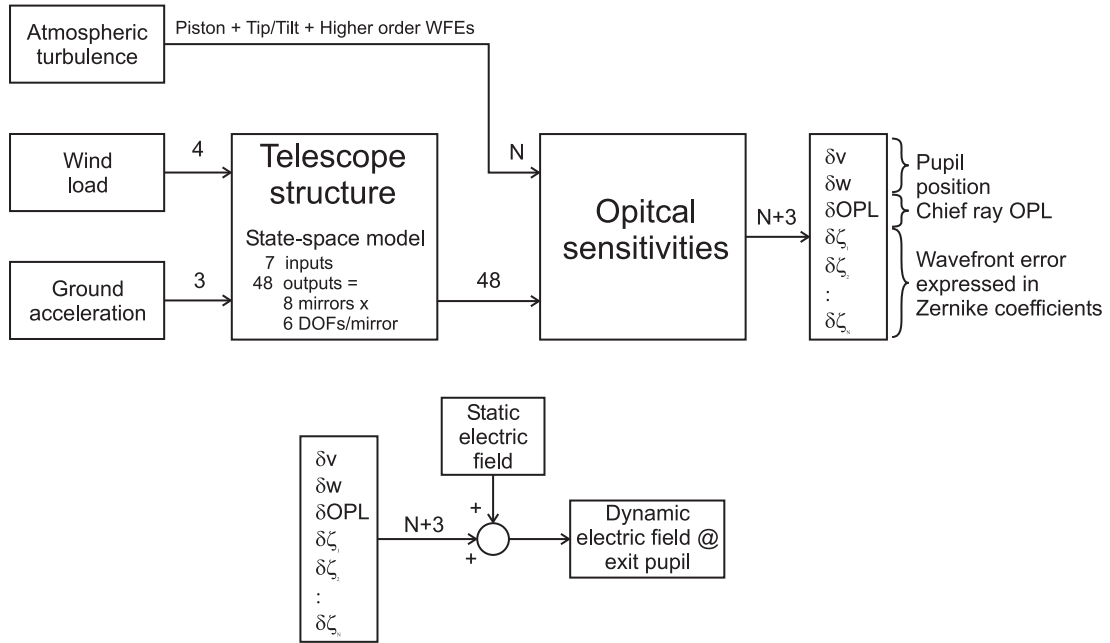


Figure 5.5: Schematic drawing of the signal flow for one arm and one band in the Integrated Model.

“80”) hold two vectors  $z_1$  and  $z_2$  related to the two interferometric beams. In general the instrument band is split into several sub-bands, and additional bands are used for the fringe tracking sensor and the tip/tilt sensor, since these sensors use light of spectral bands separated from the scientific band.

The disturbance signal vector entering the subsystem model of a single UT arm (Figure 5.6) is of size  $(7 + N) \times 1$  ( $= 44 \times 1$  for  $N = 37$ ). The label “4{44}” in Figure 5.6 indicates that the disturbance vector is divided into four groups: (i) wind load (4 components corresponding to the four above mentioned load cases, see Section 5.3.2), (ii) seismic noise (3 components representing the accelerations along  $u$ ,  $v$  and  $w$ -directions), (iii) atmospheric piston and tip/tilt (3 components), and (iv) higher-order modes of atmospheric turbulence ( $37 - 3 = 34$  components). The telescope subsystem (block labeled “Telescope”) contains an SMI-created structure model coupled to a BeamWarrior-created linear optical model. The output vector of the linear state-space structure model has the size  $48 \times 1$ —holding 6 DOFs (translation and rotation) for each mirror  $M1 \dots M8$ . It is passed as input to the optical model represented by a  $40 \times 48$  sensitivity matrix. All control loops directly act on the beam characteristics vector  $z$ . The fast tip/tilt loop additionally acts on a  $2 \times 1$  vector  $(\delta X, \delta Y)$  defining the deviation of the image position in the transmitted Coudé focus from its static value.



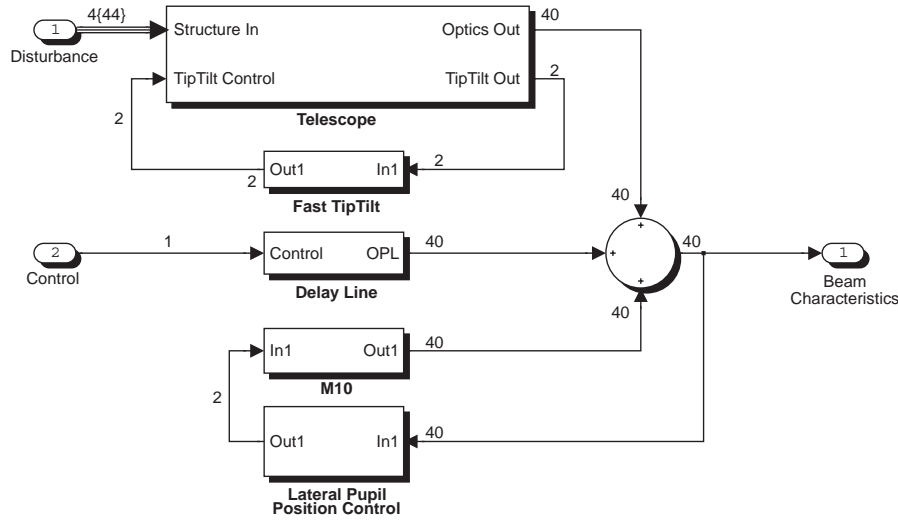


Figure 5.6: Subsystem model of a single interferometer arm (UT) with the main control loops

### 5.3.3 Simplified beam combiner models

The outputs of the integrated model are the time-dependent electric fields in the VLTI exit pupils located in the beam combination laboratory. This location corresponds to the interface between the interferometer and the scientific instruments. The model output can serve as input to an instrument model. We have developed a simplified model of the test instrument VINCI currently operating with the VLTI [51]. It computes interference fringes assuming “pupil-plane” (i.e. coaxial) beam combination of two beams using a temporal optical pathlength modulation scheme. VINCI performs modal filtering using single-mode fibers to “clean” the wavefronts before interferometric superposition. In this way spatially and temporarily varying wavefront aberrations across each beam are “translated” into temporal variations of optical power at the fiber output.

After modal filtering, the fields of the two arms related to the *same* star polarization and the *same* spectral sub-band are superposed in a partial coherent way considering temporal coherence effects due to the finite spectral bandwidth of the respective sub-band. This results in separate interferograms for the two star polarizations  $Pol = s, p$ , the different spectral bands and the Cartesian components of the electric field, which are then added on intensity-basis.

### 5.3.4 An efficient method for beam combination - the Ruilier approximation

Both, the simulation of instruments operating in a broad spectral band, and the modeling of extended source interferometry with a beam combiner using single-mode

fibers require a fast method of modeling beam combination, as otherwise each spectral sub-band and each point of an extended source has to be propagated separately through the optical system. Since the latter is a highly non-linear process, a linearization is not possible. Within the development of BeamWarrior and the VLTI Integrated Model different methods were analyzed. The one is a direct method, where for each time-step the electric field is computed at the telescope exit pupil and then modally filtered by means of a classical FFT-based algorithm. A faster approximation is the Ruilier approach developed for BeamWarrior within the FINCH project.

The different steps for the "direct" method are:

- Creation of the electric field in a plane before the fiber entrance, which is the exit pupil of the telescope: In the linear optical model the time-dependent electric field is built of the static electric field and the time-dependent deviations expressed with Zernike polynomials and lateral shift. This gives a separate electric field for each interferometer arm, for each Cartesian component, for each of the two star polarizations and, in the case of an extended source, for each source point.
- Propagation of the light through the fiber. This includes the coupling of the fields into the fiber, which is an highly non-linear process dependent on the spatial distribution of amplitude and phase as well as the lateral position of the telescope exit pupil.
- Coherent combination of the light of both interferometer arm, which has to be computed separately for each spectral band, for each source polarization and for each Cartesian component.
- The incoherent superposition of all the intensities of the individual spectral bands, the different source polarizations and the different Cartesian components.

The realization of this direct method involves a high computational cost, as this has to be performed at each time step. The implementation of the first three items is realized with the Simulink S-functions "BuildMonochromaticFields", "SMFibrePropagation" and "CoherentSuperposition", that were developed within the scope of the FINCH project and provided for testing purposes by EADS Astrium, Germany.(see figure 5.7)

To accelerate this computation, the first two of these four steps are replaced by a method developed by C. Ruilier, which is valid for small Zernike aberrations.[52, 53] The complex output intensity of the fiber at the beam combiner is approximated by the ideal output and a degradation and phase shift due to the wavefront error expressed with Zernike polynomials in the pupil plane. Ideal output means the intensity and phase produced by the modal filtering of an unaberrated reference beam with amplitude profile  $\hat{E}_{Pupil}$  and a flat wavefront.

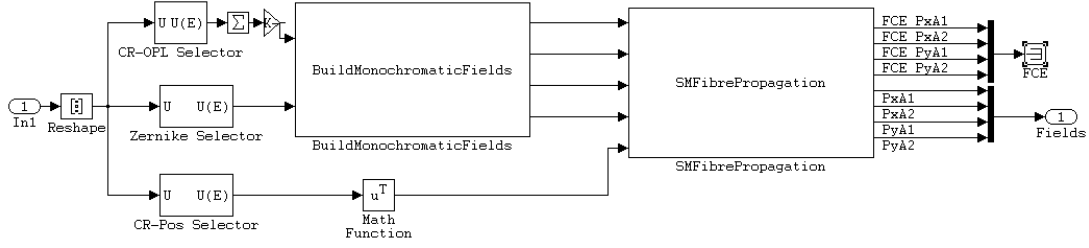


Figure 5.7: For the exact simulation of the modal filtering process Simulink S-functions are used. “BuildMonochromaticFields” generates the time-dependent electric fields from the static electric fields and the time-dependent deviations. “SMFibrePropagation” simulates the propagation of the light through the single mode fiber resulting in complex electric fields separately for the source polarizations and cartesian components.

Zernike polynomials are an orthogonal set, but due to the coupling into the fiber the individual Zernike terms are no more decoupled, since the distribution of electric field amplitude and the waveguide mode of the fiber have to be taken into account. To include this correlation a matrix  $k_{m,n}$  is computed

$$k_{m,n} = \frac{\int \int \psi_m(r, \theta) \psi_n(r, \theta) \hat{E}_{mode}(r, \theta) \hat{E}_{pupil}(r, \theta) r dr d\theta}{\int \int \hat{E}_{mode}(r, \theta) \hat{E}_{pupil}(r, \theta) r dr d\theta}, \quad (5.3)$$

where  $\psi_m(r, \theta)$  and  $\psi_n(r, \theta)$  are the Zernike polynomials,  $\hat{E}_{mode}(r, \theta)$  is the amplitude profile of the fundamental mode backpropagated to the plane of the injection optics and  $\hat{E}_{pupil}$  is the electric field amplitude profile in the plane of the injection optics (“pupil function”).

For the wavefront phase at a wavelength  $\lambda$  written in terms of Zernike polynomials  $\psi_m$  and Zernike coefficients  $\zeta_m$  (in units of m)  $\phi(r, \theta) = \frac{2\pi}{\lambda} \sum_m \zeta_m \psi_m(r, \theta)$  the normalized power coupling efficiency can be written as:

$$\rho^{WFE} \approx \exp \left\{ \left( -\frac{2\pi}{\lambda} \right)^2 \sum_{m,n \geq 2} \zeta_m \zeta_n k_{m,n} \right\}; \quad 0 \leq \rho^{WFE} \leq 1 \quad (5.4)$$

The approximation for the phase change due to modal filtering reads:

$$\Delta\phi^{WFE} = \frac{2\pi}{\lambda} \sum_{m \geq 1} \zeta_m k_{m,1} \quad (5.5)$$

Thus, the phase shift is linearly approximated with the Zernike coefficients and the loss in power coupling efficiency is an exponential function with second order terms of Zernike coefficients. After the electric field amplitude  $\hat{E}^{Static}$  and phase  $\phi^{Static}$  are computed with a direct propagation of the unaberrated reference beam with amplitude

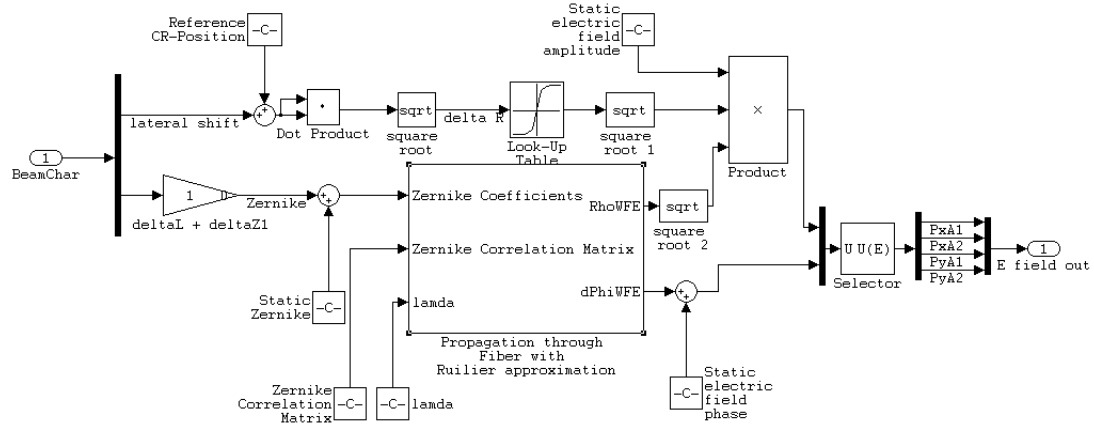


Figure 5.8: Ruilier method for simulating the modal filtering process. The upper part deals with the effects of lateral beam shift using a look-up table. The wavefront errors expressed in Zernike coefficients are the concern of the lower part resulting in both loss of field coupling efficiency and a phase shift.

profile  $\hat{E}_{Pupil}$  and a flat wavefront, the resulting dynamic electric field is approximated with the amplitude and phase

$$\hat{E}(t) \approx \hat{E}^{Static} \sqrt{\rho^{WFE}(t)}; \quad \phi(t) = \phi^{Static} + \Delta\phi^{WFE}(t) \quad (5.6)$$

Besides the wavefront error the lateral shift of the telescope exit pupil with respect to the optical fiber has to be taken into account. As a first approximation, this is considered independent of the wavefront error reducing the field coupling efficiencies only. In the Simulink model the effects due to lateral shift are realized using a two-dimensional lookup-table. However, the effects due to lateral beam shift are not fully decoupled from the wavefront errors. Thus these effects have to be further investigated in more detail to include them into a future version of the model. The Simulink blocks corresponding to the Ruilier approximation of the optical fiber are shown in figure 5.8.

## 5.4 Simulation results

A large variety of simulations can be done with the VLT Integrated Model combining, e.g., different disturbances, control parameters and configurations. Only some examples will be given in the following for the typical wind velocity of 10 m/s focusing on the relevance of the individual disturbances and telescope components.

### 5.4.1 Test of plausibility for a sensitivity matrix

Within the VLTI Integrated Model the relevant optical quantities are directly connected to the rigid body motions of the mirrors. As an example table 5.1 shows a part of the full sensitivity matrix for the first three mirrors of the UT. The displayed optical quantities are the lateral shift of the VLTI exit pupil ( $\Delta X_{Pupil}$  and  $\Delta Y_{Pupil}$ ) and the four lowest Zernike polynomials describing the wavefront error in the exit pupil. The rigid body motions of the mirrors are described in a local coordinate system with  $X$  aligned to the altitude axis and  $Z$  aligned to the optical axis of mirror M1.

The OPL is the quantity which can easily be checked for plausibility. For mirror M1 and M2 the OPL is very insensitive for a translations  $\Delta X$  and  $\Delta Y$  as these are perpendicular to the optical axis. For a  $\Delta Z$  shift both mirrors have the same magnitude of nearly 2 in their sensitivity as the OPL of both the incident ray and the reflected one is (nearly) changed by  $\Delta Z$ . The sensitivity values have different signs as the incident ray is for M1 oriented to  $-Z$  and for M2 to  $+Z$ . The tertiary M3 is a flat mirror oriented with  $45^\circ$  to the  $Z$  axis to redirect the light towards the Nasmyth-focus. Hence translation  $\Delta Y$  has no effect onto the OPL and both  $\Delta X$  and  $\Delta Z$  have a sensitivity of one again with different signs.

All optical quantities are insensitive for a rotation of M1 or M2 along the  $Z$ -axis according to the rotational symmetry of these mirrors. The pupil position is mostly influenced by tilting mirror M1, but it is also very sensitive to a tip of M2 or M3. The lateral translations of M1 and M2 result both with a large amplification in a pupil shift.

The wavefront tip/tilt in the exit pupil are mostly influenced by the tip/tilt of M1. Besides the OPL,  $\Delta Z$  of M1 and M2 have the largest impact onto the focus error. The reason for this is the optical layout of the VLT, since this is of Ritchey-Chretien type und thus the (nearly) parabolic primary shares a common focus with the (nearly) hyperbolic secondary. A  $\Delta Z$  motion of M1 or M2 moves the mirrors focal point out of the focus of the other mirror and causes therefore a focal error in the exit pupil.

The sensitivity matrix created remotely by BeamWarrior corresponds therefore to expected values.

### 5.4.2 Contribution of different components to the error due to wind load

To analyze the windload in more detail, the effects are split into the the contributions of the individual mirrors M1, M2 and M3. Moreover the errors due to the four different force sets for the wind load M1, M3, TU and TR are investigated.

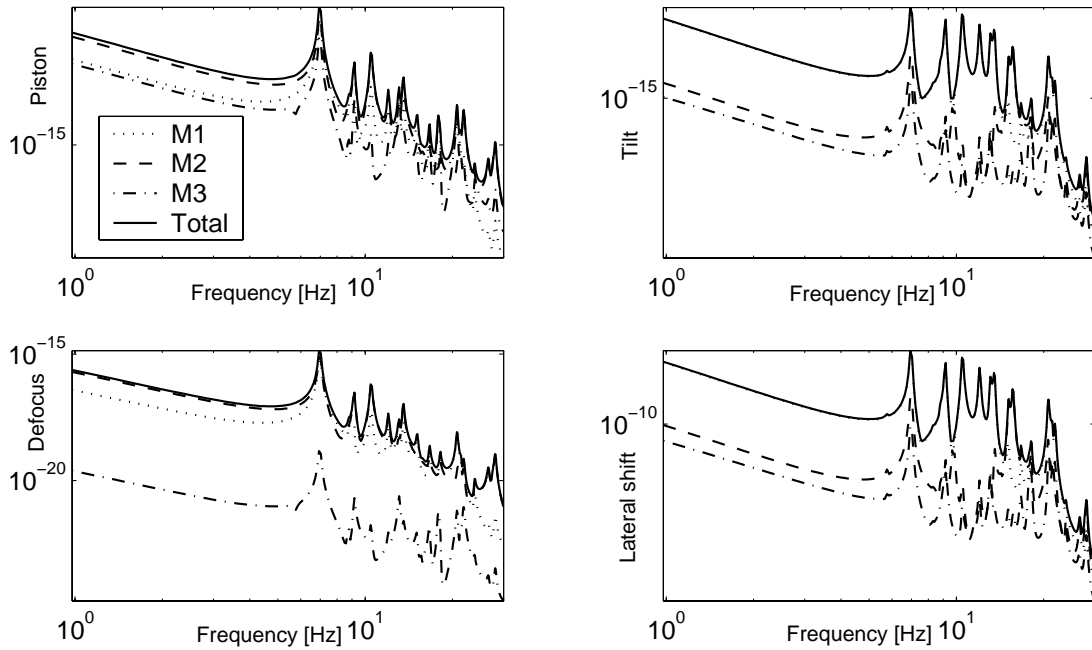


Figure 5.9: Contributions of the mirrors M1 M2 M3 of the UT to the PSD errors for piston, tilt, lateral pupil shift and defocus due to wind load.

Figure 5.9 shows the PSDs of the low order wavefront errors  $\Delta(OPL)$  ( $= \Delta(piston)$ ),  $\Delta(tilt)$ ,  $\Delta(defocus)$  and  $\Delta(lateral\ pupil\ position)$  with the individual effects caused by the motion of M1, M2 and M3 together with the total values. The piston is dominated by the motion of mirror M2 although both M1 and M2 have the same sensitivity. Due to the stiffness and the loads the vibrations of M2 are larger than that of M1. For the tilt practically only M1 is responsible which is also caused by the sensitivity, which is more than seven times larger for M1 than for M2 or M3. For defocus, both M1 and M2 share the resonance peaks with about the same amplitudes while M2 becomes more important in the low frequency range. The lateral pupil shift is practically only governed by the motion of M1 which corresponds well to the expectations due to the sensitivity table 5.1.

Besides the effects due to the three mirrors of the main optics, the four load sets with load on mirror M1 (M1), the load on M3 mirror and the M3 tower (M3), the load on the tube including center piece and Serrurier bars (TU) and the load on the top unit with M2 housing, M2 spider and M2 top ring (TR) (see figure 3.7 and section 3.5.2) are investigated separately. Again the low order wavefront errors are shown in figure 5.10. The effects due to the loads TU and TR are the most important, whereas the contribution of mirror M3 and M3 tower is the smallest. The different corner frequencies for the different spectral distributions of the load sets cannot be seen in this graphics, as they are below one Hz, where the wind load is acting exclusively statically on the structure.

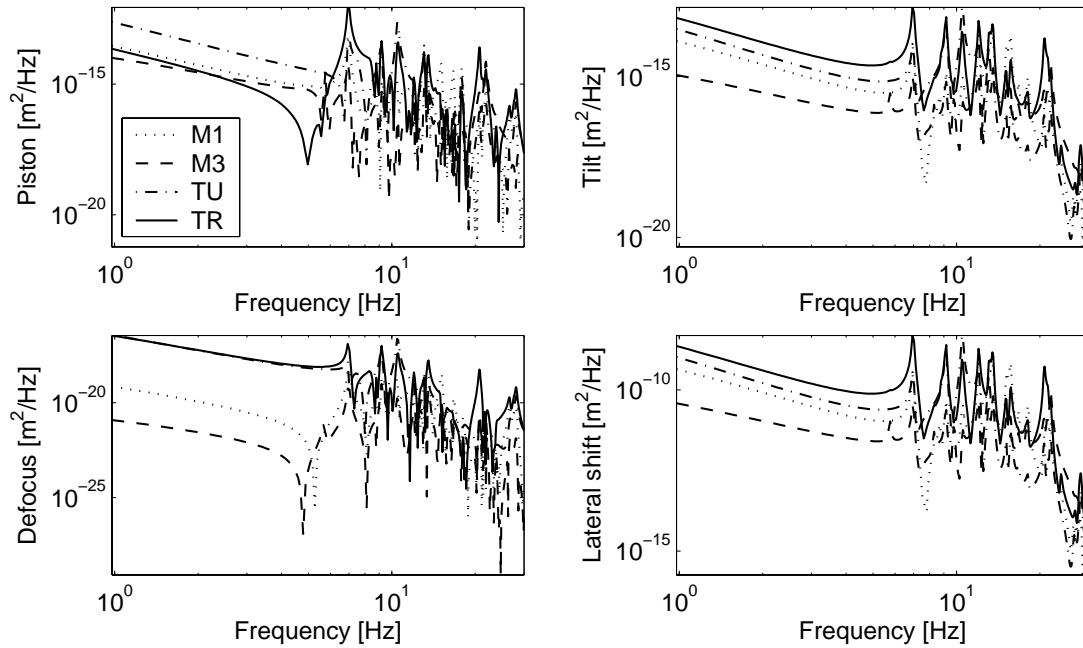


Figure 5.10: Contribution of the four load cases M1, M3, TU and TR of the UT to the low order PSD errors due to wind load.

### 5.4.3 Contribution of different disturbances to the error

Apart from the wind load the atmospheric turbulence and the micro seismic excitation are the most important error sources. In figure 5.11 the low order wavefront errors again with piston, tilt, focus error and lateral pupil shift are shown. For the higher order errors astigmatism and coma are displayed in figure 5.12. The low frequency piston of the atmosphere is dominant whereas the peaks due to the structural vibrations in the eigenfrequencies exceed the atmospheric turbulence for both the wind load and the seismic excitation. The wind load is declining with increasing frequency whereas the seismic amplitude stays on a nearly constant level within the displayed frequency range. Thus for higher frequencies the seismic piston effects exceed the wind effects.

For the wavefront tilt the structural deflections are more important than the atmospheric turbulence. Already in the low frequency range the tilt due to wind load is larger than the atmospheric tilt. The constant seismic contribution and the decreasing wind effects can be seen again.

For the focal error the effects due to mirror motion are less important than the atmosphere. Only some resonance peaks due to wind reach the level of the atmospheric error. The same is even more true for the higher order wavefront errors. As figure 5.12 shows, the atmospheric high order errors exceed the effect due to wind and seismicity by some orders of magnitude and can therefore nearly be neglected in this model. However, this is simply the case as only the rigid body motions of all mirrors are included into the simulation. This approach is valid, as apart from M1 all mirrors are relatively small, stiff mirrors, where the wind load does not cause a large elastic

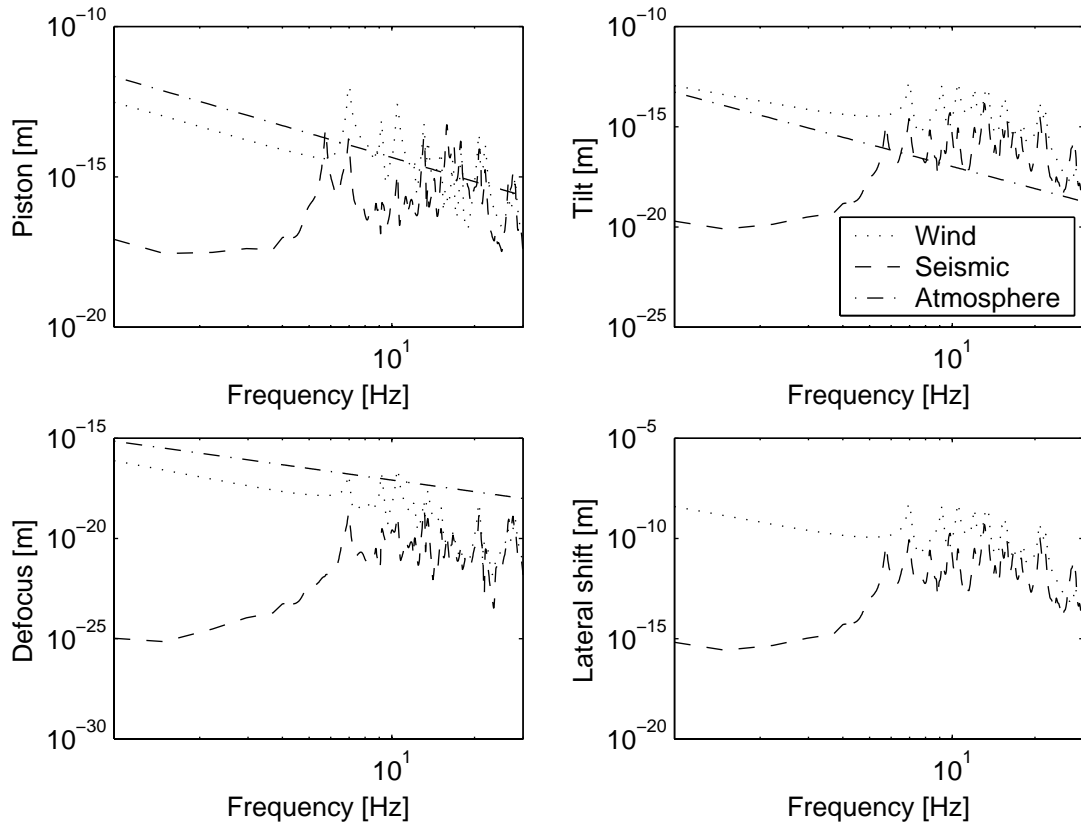


Figure 5.11: Contribution of wind load, seismic excitation and atmospheric turbulence to the low order errors (piston, tilt, lateral pupil shift and focus error).

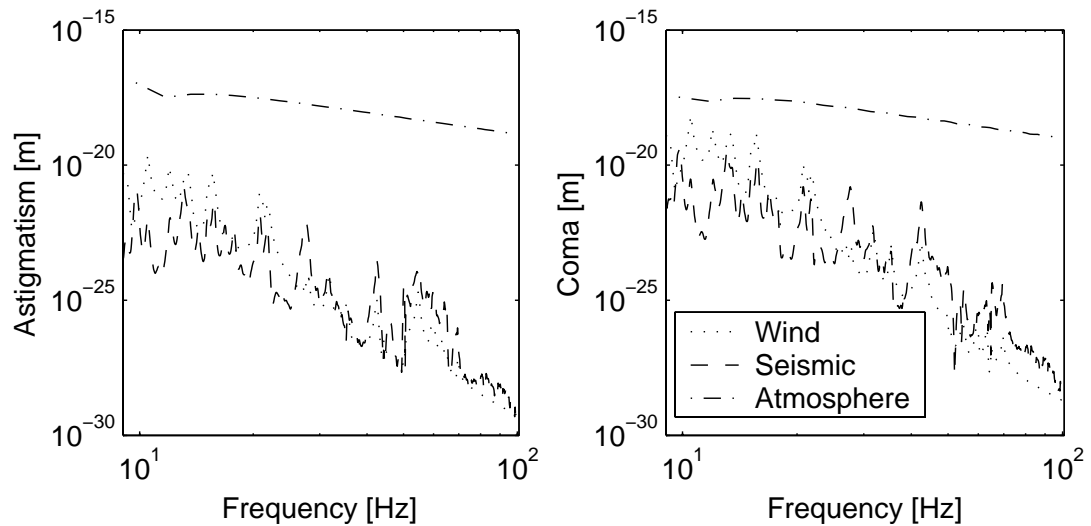


Figure 5.12: Contribution of wind load, seismic excitation and atmospheric turbulence to the higher wavefront errors showed by mean of astigmatism and coma.

deformation. For mirror M1 an active optics control loop keeps the desired mirror shape with a bandwidth up to some Hz.



### 5.4.4 Disturbance rejection of the control loops

The disturbance rejection of the Fringe Tracking Loop (=OPD control loop) and Fast Tip/Tilt Control loop are shown in figures 5.13 and 5.14. The Fringe Sensor Unit (FSU) measures the OPD between both interferometer arms in the laboratory. This signal is fed back over the OPD controller (OPDC) to the Delay Line (=actuator). For the UT the tip/tilt controller uses the measurement of the wavefront tilt at the transmitted Coudé focus (as a lateral shift of the stellar image (in BeamWarrior: spot diagram centroid)) and feeds the signal back to the tip/tilt mirror M2.

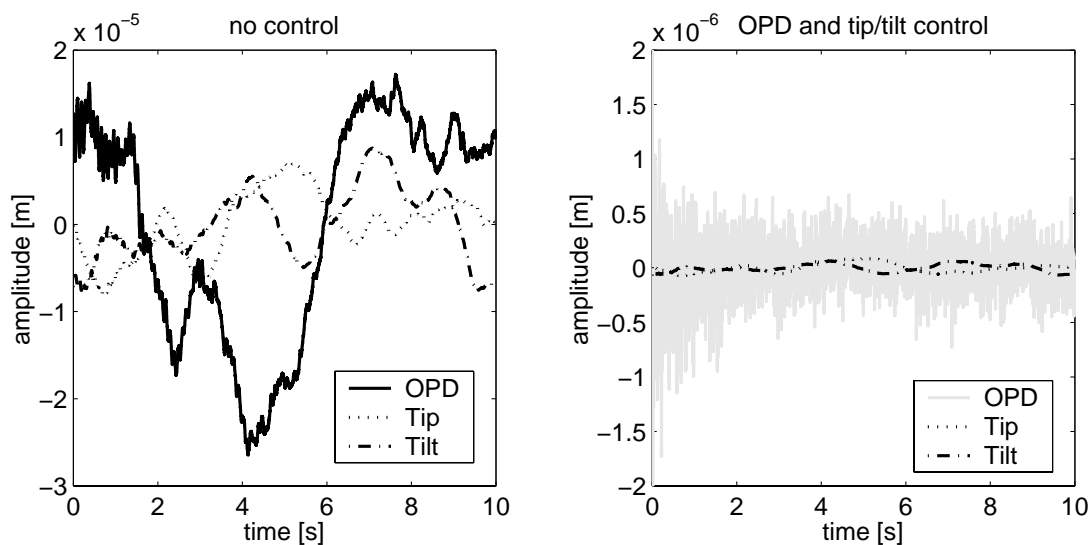


Figure 5.13: Time-history effect of the Fringe Tracking Control loop and the Fast Tip/Tilt Control loop onto the OPD and the tilt of the wavefront in the exit pupil.

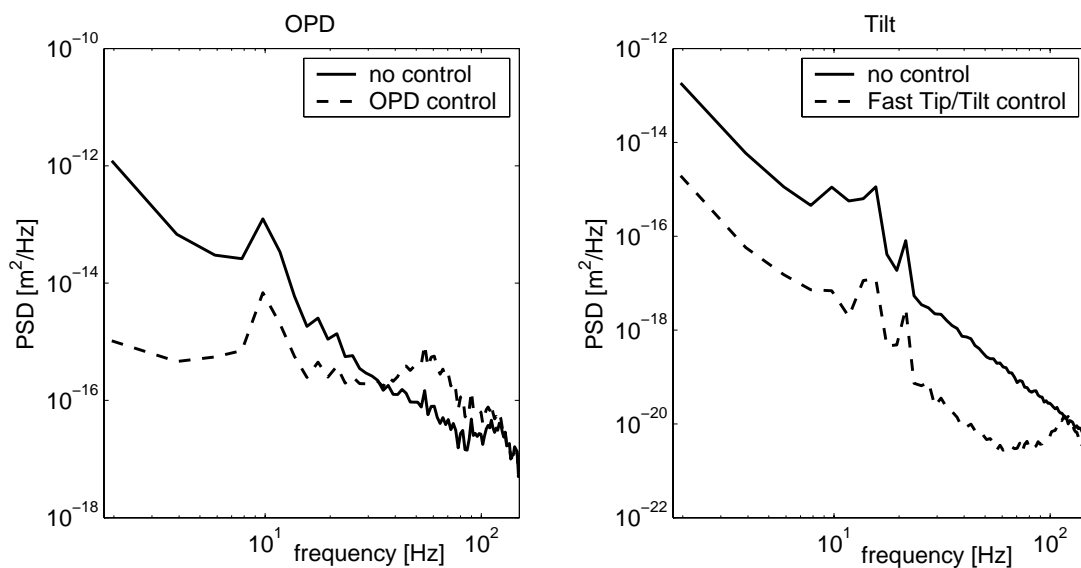


Figure 5.14: Disturbance rejection of the Fringe Tracking Control loop and the Fast Tip/Tilt Control loop in the frequency domain.

Figure 5.13 shows with the example of a time-history without control (left) and with closed loop control (right) the reduction of the wavefront errors. Especially the low frequency OPD error is removed, while the signal is oscillating with the high frequency components. In figure 5.14 the corresponding PSDs are plotted. The bandwidth of the OPDC (left) is limited due to the dynamics of the Delay Line and the noise signals added to the sensor and actuator outputs. The integrating part of the controller reduces very efficient the low order OPD error, but between 12 and 100 Hz the controlled OPD is even worse than the open loop OPD. For higher frequencies the roll-off of the OPDC becomes high enough and thus the open loop and the closed loop signals are identical. According to the right plot in 5.14 the Fast Tip/Tilt control loop acts with nearly constant efficiency up to 60 Hz. This is caused by a dominant proportional part in the controller. The low frequency dynamic could be further improved by increasing the integrating component in this control loop. The disturbance rejection decreases again for higher frequencies due to the limited dynamics of the components in the loop.

The specification for the wavefront errors is typically dependent on the observation band and the exposure time. For shorter times the statistical errors are smaller (see appendix A). Table 5.2 lists the rms errors for the OPD and the wavefront tilt in the exit pupil for different exposure times. This table allows quantitatively to evaluate the efficiency of the applied controllers reducing significantly the rms errors for short time exposure and for longer exposure times.

Table 5.2: Open loop and closed loop rms errors for OPD and tilt computed for a wavelength of  $2.2\mu\text{m}$  for different exposure times.

time	OPD [1e-6 m]		Tilt [mas on sky]	
[s]	no OPD control	OPD control	no tip/tilt control	tip/tilt control
0.1	1.04	0.369	19.6	0.0147
1.0	4.09	0.375	102	0.0933
10	12.60	0.382	203	0.211

### 5.4.5 Accuracy evaluation of the Ruilier approximation

The computational cost for the Ruilier approximation is significantly lower than that for the exact method. A comparison of required simulation time shows an acceleration of a factor of about 7700 for a  $101 \times 101$  pixel map. However, the method is limited to small aberrations. Figure 5.15 shows examples of loss in field coupling efficiency and phase shift due to simple aberrations. The rising error for increasing wavefront errors can be seen. Table 5.3 lists the maximum difference between the exact method and the approximation for different levels of aberrations.

The effects of lateral pupil shift are relatively small for slight shift-values. As the look-up table is directly created from simulations with the *exact* method no differences can be seen in figure 5.16 on the left top. The loss in field coupling efficiency due to the Zernike wavefront errors is approximated with a Gaussian function. The output phase is linearly expressed dependent on the Zernike coefficients (compare to equations (5.4) respectively (5.5)). The maximum error between the Ruilier approximation and the *exact* method is much dependent on the Zernike polynomial. Table 5.3 shows for example at a level of  $0.5\mu m$  wavefront error a significant higher deviation for the focus error than for tilt, astigmatism, coma or spherical aberration. As figure 5.16 shows on the lower right plot, the coupling between two errors can further reduce the range, where the approximation is valid. While the tilt cause a small phase error up to nearly  $2\mu m$  and the spherical aberration up to  $1\mu m$ , the combination of  $0.5\mu m$  tilt and  $0.5\mu m$  spherical aberrations already reaches the limits of valid approximation. Hence before applying this approximation method it should be checked that the Zernike coefficients do not exceed conservatively chosen limits.

For wind load and atmospheric turbulence the resulting intensity histories are plotted in figure 5.16 and 5.17. As for the instrument VINCI three signals are produced: the two intensity measurement of the individual arms and the interferometric signal with the characteristic fringe pattern. In figure 5.16 the only disturbance is the wind load, while the OPD and tip/tilt wavefront error is fully compensated by the control loops. The radiometric intensities of both interferometer arms are nearly constant and the interference fringes show a pattern similar to the ideal shape in figure 2.5. The reason for this are the relatively small higher order wavefront aberrations due to wind load.

Both the *exact* method and the Ruilier approximation give very similar results as can be seen in the magnified plot on the left. Table 5.4 compares the approximation errors for the three channels depending on the applied control loops. The OPD control loop has no direct influence onto the approximation since an extra OPD causes simply an additional phase difference between both arms and thus the accuracy for the intensities of arm 1 and arm 2 do not change. The small decrease of error for the interferometric intensity is due to a larger maximum amplitude this signal. The tip/tilt wavefront error contributes significantly to the deflection between both methods. Hence closing this control loop increases the accuracy of the approximation method.

As shown in section 5.4.3 the atmospheric turbulence causes much larger high order wavefront aberrations than the telescope vibrations due to wind load or seismicity. In figure 5.17 the time-histories of the individual intensities are plotted. The radiometric intensities are no more constant but vary over the time due to a varying coupling efficiency of the electric field into the optical fiber. The average interferometric signal is varying in the same way since it is composed of the intensities of the arms. Moreover the fringe contrast is varying, which is maximum for the superposition of two signals with the respective phase difference of  $\pi$  and the same amplitude.

The large high order wavefront errors are the reason why the Ruilier approximation shows distinct deviations from the *exact* method. Therefore this method cannot be applied simulating atmospheric turbulence of this magnitude without an adaptive optics system.

Table 5.1: Sensitivity matrix of the rigid body motions of primary mirror M1, secondary mirror M2 and tertiary mirror M3 of the Unit Telescope (UT) of VLT.

		$\Delta X_{Pupil}$	$\Delta Y_{Pupil}$	OPL	Tip	Tilt	Defocus
M1	$\Delta X$	44.772	-27.699	0.001	-0.229	0.149	+1.7439e-005
	$\Delta Y$	29.048	42.605	0.003	-0.149	-0.229	-2.9972e-005
	$\Delta Z$	0.015	0.025	-1.982	-0.000	-0.000	+1.8773e-002
	$\Delta\phi_x$	-836.400	-1226.929	-0.047	4.318	6.646	+3.8157e-004
	$\Delta\phi_y$	1290.391	-798.079	0.050	-6.647	4.313	+3.3641e-004
	$\Delta\phi_z$	0.368	-0.243	-0.002	-0.002	0.001	+2.7663e-006
M2	$\Delta X$	-39.447	24.395	-0.002	0.201	-0.131	-1.4537e-005
	$\Delta Y$	-25.546	-37.490	-0.001	0.131	0.202	+1.8132e-005
	$\Delta Z$	-0.019	-0.026	1.981	0.001	0.000	-1.9107e-002
	$\Delta\phi_x$	116.370	170.739	0.005	-0.601	-0.925	-5.1494e-005
	$\Delta\phi_y$	-179.539	111.055	-0.005	0.925	-0.600	-4.7876e-005
	$\Delta\phi_z$	-0.061	0.038	-0.000	0.000	-0.000	+1.7298e-007
M3	$\Delta X$	-5.364	3.317	1.000	0.028	-0.018	-2.7691e-004
	$\Delta Y$	-0.002	0.001	0.000	0.000	-0.000	-7.5529e-008
	$\Delta Z$	5.363	-3.317	-1.000	-0.028	0.018	+2.7692e-004
	$\Delta\phi_x$	-23.786	-34.904	-0.001	0.123	0.190	+7.0752e-006
	$\Delta\phi_y$	73.403	-45.394	0.002	-0.379	0.246	+1.3122e-005
	$\Delta\phi_z$	-23.762	-34.919	-0.001	0.123	0.190	+7.1638e-006

Table 5.3: Accuracy of the Ruilier approximation for varying a single Zernike wavefront aberration. The table lists the difference of the exact propagation for the center wavelength  $\lambda_c = 2.2\mu m$  expressed in the maximum relative amplitude error (respectively the ideal efficiency) and the phase shift in [rad]. The level gives the Zernike coefficient in [m]; e.g. a tilt of level  $1.00e-6$  gives a maximum wavefront error of  $1.00e-6$  m at the outer rim.

Level [m]	Tilt		Focus error		Astigmatism		Coma		Spherical	
	$\Delta\rho$ [%]	$\Delta\phi$ [rad]	$\Delta\rho$ [%]	$\Delta\phi$ [rad]	$\Delta\rho$ [%]	$\Delta\phi$ [rad]	$\Delta\rho$ [%]	$\Delta\phi$ [rad]	$\Delta\rho$ [%]	$\Delta\phi$ [rad]
$1.00e-7$	0.29	0.02	0.57	0.02	0.25	0.02	0.26	0.02	0.34	0.02
$5.00e-7$	1.22	0.03	8.63	0.10	0.63	0.03	1.01	0.04	1.07	0.02
$1.00e-6$	4.26	0.04	17.76	0.74	3.12	0.04	5.32	0.06	8.26	0.15
$3.00e-6$	7.26	3.71	33.00	5.20	28.05	0.05	16.90	3.55	30.20	4.28

Table 5.4: Relative error (rms-error in per cent of maximum amplitude) between exact computation and Ruilier approximation for time simulations. Three cases are listed for wavefront errors due to wind load: without control, closed Fringe Tracking loop (OPD control) without tip/tilt control and both OPD control and tip/tilt control.

[%]	Intensity arm1	Intensity arm2	Intensity interferometer
no control	1.08	0.50	0.64
OPD control	1.08	0.51	0.53
OPD + tip/tilt control	0.12	0.02	0.28

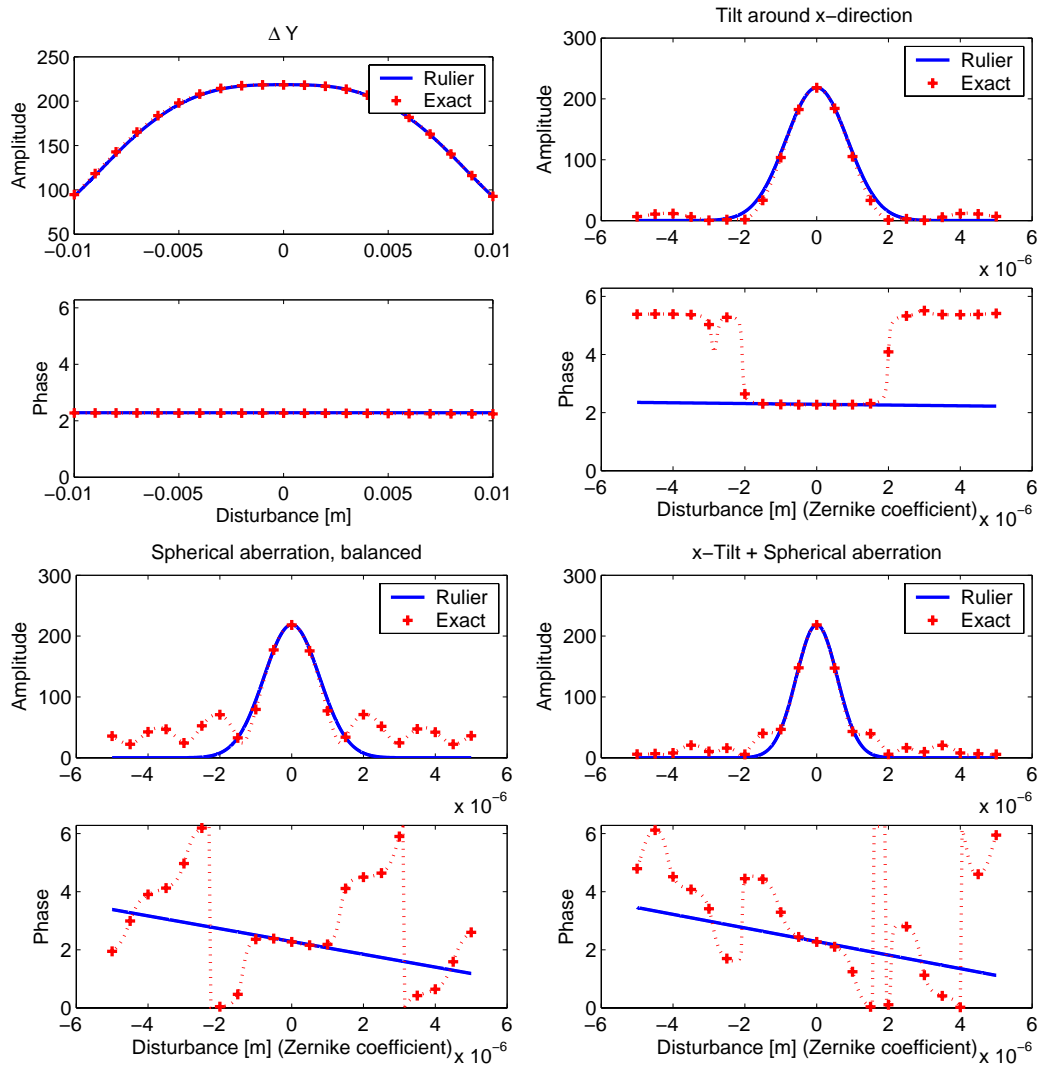


Figure 5.15: Intensity loss and phase shift due to simple phase aberrations. For small aberrations the Rulier methods gives a good approximation. The effects of simple aberrations are displayed for  $\lambda_c = 2.2\mu m$  (starting at top left plot): lateral shift (no difference due to look-up table), tilt, spherical aberration and combination of tilt and spherical aberration (both coefficients varying with equal magnitude)

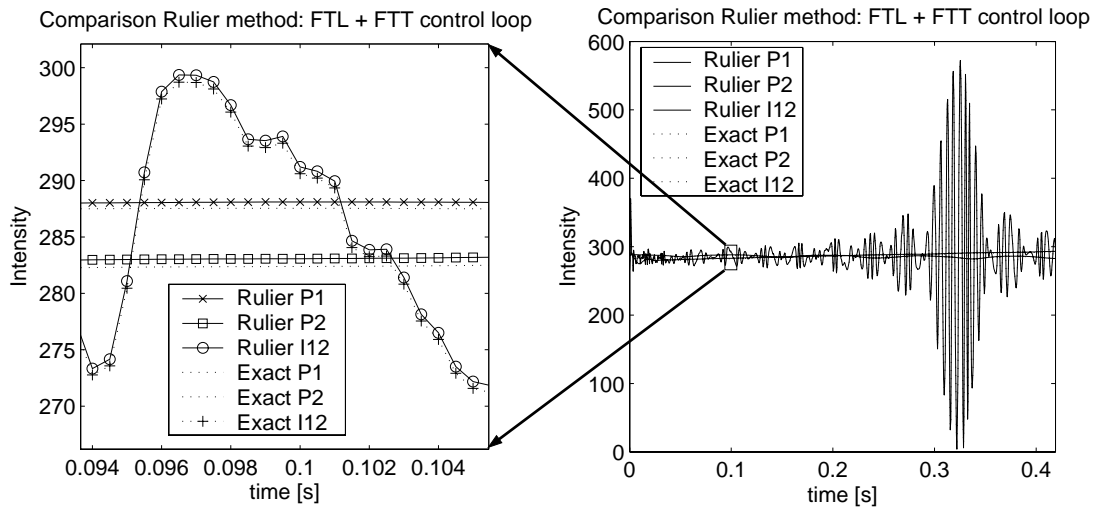


Figure 5.16: Example for the time-history of the VINCI output: intensities of the two interferometer arms P1, P2 and the interferometric fringe intensity I12 due to wind load.

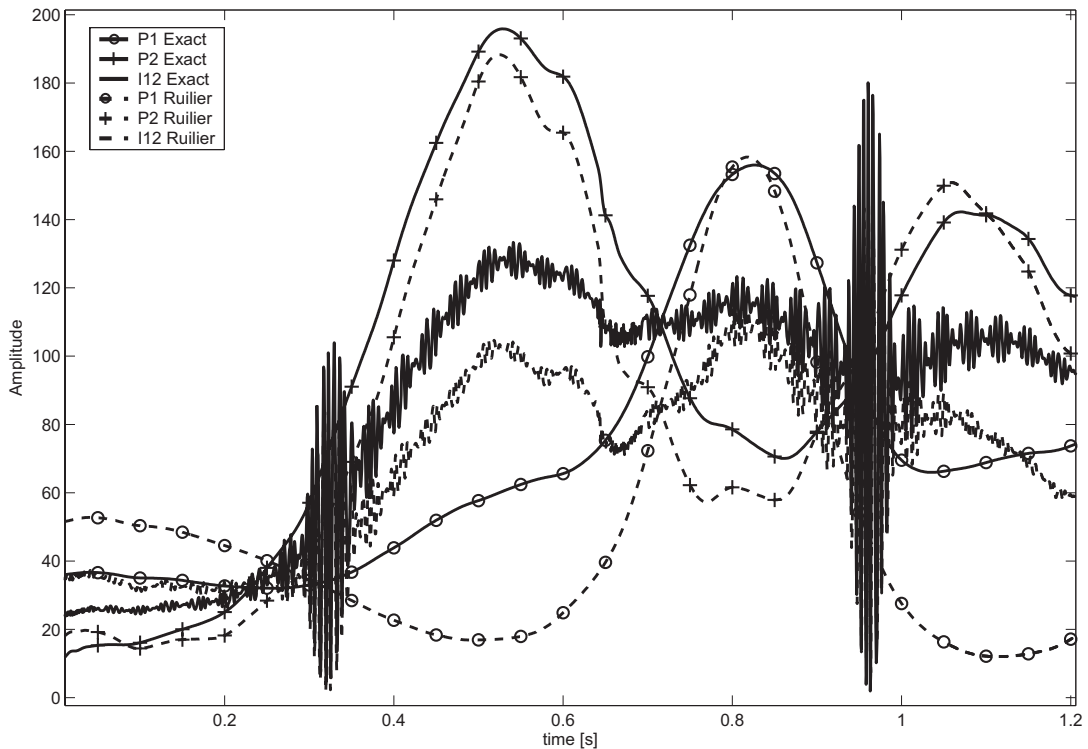


Figure 5.17: Example for the time-history of the VINCI output: intensities of the two interferometer arms P1, P2 and the interferometric fringe intensity I12 due to atmospheric turbulence.



# 6 Conclusion and outlook

## 6.1 Conclusion for this work

Future large astronomical telescopes will be highly complex systems incorporating key technologies as active and adaptive optics, huge probably actively damped lightweight structures or high precision measurement systems providing the data to steer various actuators in closed loop control. A comprehensive integrated model computing the time-dependent signal flows between the components and subsystems is a required tool for the multidisciplinary system engineering.

This is true for all phases of a telescope project, since, for example, in the planing phase the evaluation of feasibility and functionality of different concepts need a suitable model. For a final design the performance can only be predicted reliably if major crosstalk and interaction between all different dynamical subsystems is considered.

In this work a concept was shown to provide a suitable model of the telescope structure to be used in an integrated model. In addition to that an efficient approach for integrated modeling of astronomical telescopes was developed and its application to the Very Large Telescope Interferometer (VLTI) tested.

After an overview over a ground based astronomical telescope system with the major components optics, mechanics and control was given, their mathematical description was shortly explained. Moreover the different sources disturbing a ground-base telescope – especially atmospheric turbulence and wind load – are discussed. While local effects are out of the scope of the integrated models, possibilities for appropriately modeling the relevant global and large scale effects were given.

For describing the mechanical structure the governing equations were explained and a standardized state-space format was given allowing both force and acceleration inputs as well as displacement and velocity outputs. For telescope structures linear state-space models can be generated from the modal data of a finite element analysis. Only for special components like friction drive systems non-linear models have to be added. A standardized format for inputs and outputs was developed allowing to define fixed interfaces towards an FE-model.

Different techniques for model reduction were explained and their meaning was discussed. Balanced model reduction was identified as the most appropriated condensation method as the modal state-space systems keep the computational effort small.

Using selected applications to telescope structures the meaning of an appropriate scaling of inputs and outputs was explained and the effects onto the reduced models was demonstrated. Using selected applications to telescope structures the meaning of an appropriate scaling of inputs and outputs was explained and the effects onto the reduced models demonstrated.

The two special cases of scattering material parameters and the structure-soil interaction in modeling telescope structures were discussed in more detail. For scattering material parameters an approach for performing a monte carlo simulation was developed, which gives much more precise information than a worst case simulation and also allows the non-trivial identification of a worst case configuration. Especially cluster PCs allow performing such an analysis quickly and at low cost.

For modeling the interaction between telescope structure, the foundation and the soil a concept was explained using Finite Element modeling. Analyzing the preliminary design of the Overwhelmingly Large Telescope (OWL) of ESO the dynamic effects of the ground were showed to be not critical. However, this was true only for this extremely light weight construction, which distributes the telescope mass onto a large area of ground, and for the considered range of soil properties, as the influence of the ground increases with decreasing stiffness modulus of the soil.

For integrated modeling of an astronomical telescope a modular approach was developed and applied to the European Southern Observatory's VLTI. The VLTI comprises many different configurations and components which are generated consistently using a single configuration file for the computation of the linear optical models and the dynamical creation of the complete system. The VLTI Integrated Model approved the coupling between the optical modeling tool BeamWarrior and a Matlab-based integrated Simulink model to be well suited for such a complex system. The chosen degree of detail allows simulations in acceptable computational time.

With selected examples the plausibility of the sensitivity matrices was demonstrated and the distributions of the individual disturbance sources to the total wavefront error at the VLTI exit pupil was shown. While for lower order wavefront errors both the wind load and the atmospheric turbulence give significant distributions, for higher order errors the atmospheric turbulence is dominant.

For a wide field of applications a Fourier-optical method can be used which allows to compute the image of extended (arbitrary distributed) sources due to the convolution of the image of a point source and the visibility function and also easily spectral broad band effects.

A necessary requirement is linearity and isoplanatism (space-invariance), which is, e.g., violated by a single-mode wave guide (e.g. on optical fiber), since a change in the location of the point source causes a change in the amplitude of the intensity pattern and not of the location at the output of the optical fiber. Such a modal filter is used

at the VLTI for the instrument VINCI, for which a simplified model was included into the VLTI Integrated Model.

Direct modeling of each source pixel involves a high computational cost and is leading to unacceptable long simulation time. Therefore as an approximation the Ruilier method was applied. It was shown that this method gives efficiently valid results for small wavefront errors, but leads to wrong results, if the disturbance level exceeds a certain level.

When developing an integrated model, at the beginning the purpose of the model must be clearly defined. Only dependent on the desired objectives, a design with the right degree of integration, coupling and detail can be built. A final model will always be a compromise between the effort of building and handling it, the model accuracy and level of detail represented by the model as well as the computational cost for performing simulations. Therefore the right balance is very important and is mostly influence in the early design phase of the model.

## 6.2 Outlook towards modeling Extremely Large Telescopes

For future Extremely Large Telescopes (ELTs) the presented approach for building a reduced structural state-space model can fully be applied. The major differences for the telescope structure are lower natural frequencies although the design is a sophisticated lightweight construction with much higher stiffness compared to a scaled model of an existing 10m-class telescope. The larger dimensions and lower natural frequencies lead to larger influence of the wind load on the telescope performance. Force spectra will act on the individual mirror segments, which are different and partially correlated. To reliably verify the alignment system the time-dependent loads on each segment as well as the actuators and the supporting telescope structure must be represented correctly. Consequently a structural model of, e.g., OWL has to include the 10000 actuators of the segmented mirrors, but also the telescope deformations with sufficient spatial resolution. Truncating too many modes will result in an artificial increase of stiffness. To verify the model accuracy a comparison between the DC-gain of the dynamic model and results of a FE analysis can be used. The proposed balanced model reduction technique is still appropriate, especially as it can efficiently be applied to modal state-space systems.

Besides the effects onto the structural model the high degree of segmentation will also have a large impact onto the optical model and the control loops. For studying the optical effects on the VLTI UT, the ray tracing was performed with a  $[101 \times 101]$  ray grid. Using only a grid of  $[31 \times 31]$  for one segment of OWL will result in a 300 times larger number of rays. Considering six rigid body motions for each segment of

M1 and M2 nearly 20 000 singular disturbances exist increasing the sensitivity matrices accordingly. Moreover the linear optical models for the deformable mirrors of the adaptive optics have to be generated. Hence for the optics the concept is valid. However, the major challenge is the large number of segments and the grand increase of degrees of freedom, which can lead to long computation times and large memory requirements. Considering the development of more powerful computers with an increase of available memory the optical models should be computed within acceptable times.

Both the lower natural frequencies of the mechanical structure and the high number of segments complicate the telescope control. The lowest telescope modes limit either the bandwidth of the controller or a large effort is necessary to include a structural model into the controller while guaranteeing robustness. For aligning the 3250 segments for M1 and M2 of OWL 20000 sensor outputs must be connected to 10000 actuator inputs. A possible solution providing a high bandwidth are local controllers. However, although using high precision sensors the small amounts of signal noise can add up in the long chain coupled with the structure and the sensors. Moreover this coupling can cause additional dynamics and instability for the complete system forcing to reduce the controller gain and limit the bandwidth.

For modeling the full system within an integrated model an extremely large number of states is required to represent the mechanical structure, the inertia of the segments and the control loops with sensors, controllers and actuator dynamics. To keep simulation times on a tolerable level a large effort has to be put into the implementation of the complete system. A possible option could be parallel computing on a PC-Cluster, but classical simulation environments like Simulink do not support this at present.

# Bibliography

- [1] Bely, Pierre Y., "The Design and Construction of Large Optical Telescopes", Springer-Verlag, New York Berlin Heidelberg, 2002.
- [2] Andersen, Torben; Ardenberg, Arne; and Ower-Petersen, Mette, "Euro50 - Design Study of a 50 m Adaptive Optics Telescope", Lund University, Lund, Sweden, 2003.
- [3] Lawson, Peter R., "Principles of Long Baseline Stellar Interferometry," 1999. Course notes from the 1999 Michelson Summer School.
- [4] Wilson, Raymond N., "Reflecting Telescope Optics I", Springer-Verlag, Berlin Heidelberg, 1996.
- [5] Wilhelm, Rainer, "Novel numerical model for dynamic simulation of optical stellar interferometers," dissertation, Berlin, 2000.
- [6] Grogan, Robert L., Laskin, Robert A., "On Modeling Of The Space Interferometry Mission," *1*, 1995.
- [7] Redding, David, et al., "Next Generation Space Telescope Integrated Performance Modeling," *Bulletin of the American Astronomical Society* **28**(4), 1997.
- [8] Milman, Mark, Levine, Marie, "Integrated Modeling Tools for Precision Multidisciplinary Systems," <http://techreports.jpl.nasa.gov/1997/97-0283.pdf>, 1997.
- [9] Shaklan, S., Yu, J., Briggs, H.C., "Integrated Structural and Optical Modeling of the Orbiting Stellar Interferometer," *Proceedings of SPIE* **1945**, 1993.
- [10] Basdogan, Ipek, Dekens, Frank, Neat, Gregory W., "On Modeling Of The Space Interferometry Mission," *IEEE Aerospace Conference* **4**, 1999.
- [11] Lieber, Mike, "Development of the Ball Integrated Telescope Model (ITM)," *Integrated Modeling of Telescopes, SPIE* **4757**, 2002.
- [12] Roberts, Scott, et al., "Integrated modeling of the Canadian Very Large Optical Telescope," *2nd Baekaskog Workshop on Extremely Large Telescopes, Proceedings of SPIE to be published*, 2003.

- [13] Angeli, George, et al., "Integrated modeling of the Canadian Very Large Optical Telescope," *2nd Backaskog Workshop on ELTS, Proceedings of SPIE to be published*, 2003.
- [14] Angeli, George, et al., "Integrated modeling tools for large ground based optical telescopes," *Proceedings of SPIE* **5178**, 2003.
- [15] Miller, David W., de Weck, Oliver L., et al., "Integrated Dynamics and Controls Modeling for the Space Interferometry Mission (SIM)," *Proceedings of the 2001 IEEE Aerospace Conference*, 2001.
- [16] Miller, David W., de Weck, Oliver L., Mosier, Gary E., "DOCS Framework," *Integrated Modeling of Telescopes, Proceedings of SPIE* **4757**, 2002.
- [17] Bourgault, Frederic, Miller, David W., "Model Uncertainty and Performance Analysis for Precision Controlled Space Structures," masterthesis, Massachusetts Institute of Technology, 2000.
- [18] Weck, Olivier L. de, "Integrated Modeling and Dynamics Simulation for the Next Generation Space Telescope," *SPIE International Symposium on Astronomical Telescopes and Instrumentation 2000* **4013**, 2000.
- [19] Zernike F., "," *Physica* **1**, 1934.
- [20] Glindemann, Andreas, "Beating the seeing limit—adaptive optics on large telescopes". Habilitationsschrift, Ruprecht-Karls-Universität Heidelberg, Heidelberg, Germany, 1997.
- [21] Goodman, J. W., "Introduction to Fourier Optics", McGraw-Hill, 1996.
- [22] Schneermann, M., Marchiori, G., Dimichino, F., "The VLT enclosure - design and construction," *Proceedings of SPIE* **4004**, 1996.
- [23] Koehler, B., Koch, F., "Analysis of the structural deformation of the VLT Unit Telescope under dynamic wind load, microseismic noise, and vibration of equipment," Tech. Rep. VLT-TRE-ESO-11000-0480, European Southern Observatory, Garching, Germany, September 1995.
- [24] J.-M. Conan; R. Gérard; and P.-Y. Madec, "Modeling the imaging process in optical stellar interferometers," *J. Opt. Soc. Am. A* **12**, pp. 1559–1570, 1995.
- [25] Nightingale, N.S., Buscher, D.F., "Interferometric seeing measurements at the La Palma Observatory," *Monthly Notices of the Royal Astronomical Society* **251**, pp. 155–166, 1991.
- [26] Tyler, Glenn A., "Bandwidth considerations for tracking through turbulence," *Journal of the Optical Society of America A: Optics, Image Science, and Vision* **11**(1), pp. 358–367, 1994.

- [27] Quirrenbach, Andreas, "Observing Through the Turbulent Atmosphere," *Principles of Long Baseline Stellar Interferometry - Course notes from the 1999 Michelson Summer School*, pp. 71–85, 1999.
- [28] Pfeiffer, Friedrich, "Einführung in die Dynamik", B.G. Teubner, Stuttgart, 2 ed., 1992.
- [29] Locatelli, Guido, "Piezo-actuated adaptive structures for vibration damping and shape control - modeling and testing", VDI Verlag, Düsseldorf, VDI Fortschritt-Berichte ed., 2001.
- [30] "ANSYS manual Version 6.1, Structural Guide, 4.10 Modal superposition," 2002.
- [31] P. Clough, Ray W., "Dynamics of structures", McGraw-Hill International Editions, New York, Paris, Singapore, ed., 1993.
- [32] Moore, Bruce C., "Principal Component Analysis in Linear Systems: Controllability, Observability, and Model Reduction," *IEEE Transactions on Automatic Control* **26**(1), pp. 17–32, 1981.
- [33] Glover, Keith, "All optimal Hankel-norm approximations of linear multivariable systems and their L-infinity error bounds," *International Journal of Control* **39**(6), pp. 1115–1193, 1984.
- [34] Laub, Alan J., "Computation of System Balancing Transformations and Other Applications os Simultaneous Diagonalization Algorithms," *IEEE Transactions on Automatic Control* **32**(2), pp. 115–122, 1987.
- [35] Gawronski, Wodek K., "Dynamics and Control of Structure, A Modal Approach", Springer-Verlag, New York Berlin Heidelberg, 1998.
- [36] Gregory, C.Z., "Reduction of Large Flexible Spacecraft Models Using Internal Balancing Theory," *Journal of Guidance, Control and Dynamics* **7**(6), pp. 724–732, 1984.
- [37] B. Craig, R.R., "Coupling of Substructures for Dynamic Analysis," *AIAA Journal* **6**(7), pp. 1313–1319, 1968.
- [38] T. Spanos, John T., "Selection of Component Modes for Flexible Multibody Simulation," *Journal of Guidance and Control* **14**(2), pp. 278–286, 1991.
- [39] Raupp, H., Scheulen, D., Sippel, R., "Design and Analyses for the LOTHAR Reflector," Tech. Rep. ADM-DSS-TN-4500-01, Astrium, Friedrichshafen, Germany, July 2001.
- [40] Astrium, "Technical Proposal PLANCK-Reflectors," Tech. Rep. Astrium-Proposal NO. A. 2001-0134-0-1, Astrium, Friedrichshafen, Germany, May 2001.

- [41] G. Keller, Joseph B., "Exact Non-reflecting Boundary Conditions," *Journal of Computational Physics* **82**, pp. 172–192, 1989.
- [42] Appelö, Daniel, "Non-reflecting Boundary Conditions for Wave Propagation Problems". Licentiate's Thesis, Royal Institute of Technology, Stockholm, 2003.
- [43] K. Grote, Marcus J., "Exact nonreflecting boundary conditions for the time dependent wave equation," *SIAM Journal of Applied Mathematics* **55**, pp. 280–297, 1995.
- [44] Kim, Jae K., Koh, Hyun M., Kwon, Ki J., Yi, Jang S., "A three-dimensional transmitting boundary formulated in Cartesian co-ordinate system for the dynamics of non-axisymmetric foundations," *Earthquake engineering and structural dynamics* **29**, pp. 1527–1546, 2000.
- [45] T. Komatitsch, Dimitri, "A perfectly matched absorbing boundary condition for the second-order seismic wave equation," *Geophysical Journal International* **154**, pp. 146–153, 2003.
- [46] "LS-DYNA Theoretical Manual, 20.2 Transmitting Boundaries," 1998.
- [47] Ewins, D. J., "Modal Testing: Theory, Practice and Application", Research Studies Press Ltd, Hertfordshire, 2 ed., 1999.
- [48] Wilhelm, Rainer, "Comparing geometrical and wave optical algorithms of a novel propagation code applied to the VLTI," **4436**, pp. 89–100, 2001.
- [49] M. Schoeller; R. Wilhelm; and B. Koehler, "Modeling the imaging process in optical stellar interferometers," *Astron. & Astrophys. Suppl. Ser.* **144**, pp. 541–552, 2000.
- [50] Glindemann, Andreas, "VLTI technical advances (present and future)," in *New Frontiers in Stellar Interferometry*, W. A. Traub, ed., *Proc. SPIE* **5491**, 2004.
- [51] P. Kervella, "VINCI, the VLTI Commissioning Instrument: status after one year of operations at Paranal," **4838**, 2002.
- [52] C. Ruilier and F. Cassaing, "Coupling of large telescopes and single-mode waveguides: application to stellar interferometers," **18**, 2001.
- [53] C. Ruilier, "A study of degraded light coupling into single-mode fibers," **3350**, pp. 319–329, 1998.
- [54] Hughes, Peter C., "Space structure vibration modes: How many exist? Which ones are important?," *Control Systems Magazine, IEEE* **7**(1), pp. 22–28, 1987.
- [55] Lunze, Jan, "Regelungstechnik 1", Springer-Verlag, Berlin Heidelberg New York, 1996.
- [56] Lunze, Jan, "Regelungstechnik 2", Springer-Verlag, Berlin Heidelberg New York, 1997.



- 
- [57] Spanos, John T., Tsuha, Walter S., "Selection of component modes for flexible multibody simulation," *AIAA journal* **14**(2), pp. 278–286, 1990.
- [58] Nowacki, Witold, "Dynamic of elastic systems", Chapman & Hall LTD., London, ed., 1963.
- [59] Graff, Karl F., "Wave motion in elastic solids", Clarendon Press, Oxford, ed., 1975.
- [60] Welch, P.D., "The Use of Fast Fourier Transform for the Estimation of Power Spectra: A Method Based on Time Averaging Over Short, Modified Periodograms," *IEEE Transactions Audio Electroacoustics* **15**, pp. 70–73, 1967.

# List of Figures

1.1	Comparison of the telescope structure of OWL and of the VLT . . . .	8
2.1	Scheme of a telescope system . . . . .	13
2.2	Focussing of a plane wavefront by an optical system. . . . .	15
2.3	Zernike polynomials . . . . .	16
2.4	Diffraction pattern of a point source . . . . .	17
2.5	Simple model of an interferometer . . . . .	20
2.6	Frequency dependence and order of wavefront errors caused by different disturbances. (according to [1, p. 312]) . . . . .	24
2.7	Aerodynamic attenuation factor . . . . .	28
2.8	PSD of the wind velocity for the Von Karman turbulence model. For high frequencies the PSD decreases $\propto f^{-5/3}$ . . . . .	29
2.9	Wind load (in y-direction) onto mirror M1 of the UT of VLT . . . . .	30
2.10	Typical seismic event at Paranal. This type of event occurs three times per night in mean. . . . .	31
3.1	Coordinate systems and notations . . . . .	46
3.2	Model reduction of a simple system . . . . .	53
3.3	Grouping of the states according to their controllability and observability. . . . .	53
3.4	Scheme of the architecture of SMI. . . . .	64
3.5	SMI architecture and components . . . . .	65
3.6	SMI provided tools for model reduction. . . . .	66
3.7	Finite element model of a Unit Telescope of the VLT. . . . .	67
3.8	TF of the OPL due to wind load on M1 . . . . .	68
3.9	PSDs of the OPL due to wind load on M1 . . . . .	70
3.10	FE model of the OWL and major structural components. . . . .	70
3.11	Transfer functions of wind load on OWL to the motions of mirror M2 in y-direction. . . . .	71
3.12	Transfer functions of the altitude drive to the differential displacement of altitude bogie #10 . . . . .	72
3.13	Transfer functions of the altitude drive of OWL to the motions of mirror M2 in x-direction and y-direction. . . . .	73
4.1	Finite Element Model of the LOTHAR reflector . . . . .	76

4.2	Analysis setup for the LOTHAR-reflector FEM analysis. . . . .	77
4.3	Approach for analyses with random $V_f$ distributions . . . . .	79
4.4	Examples for the sensitivity of the surface error distribution . . . . .	79
4.5	Due to the nominal CTE of $6.1e-7$ 1/K cooling the reflector down to operational temperature causes a large surface error (left). After fitting the reflector the residual RMS is negligible (right). . . . .	81
4.6	Worst case fiber volume distributions . . . . .	82
4.7	Histograms of the frequency of a certain RMS error . . . . .	82
4.8	Surface error due to varying $V_f$ for the operational load case <i>OP</i> . . . . .	83
4.9	FE-model of the OWL with foundation and ground . . . . .	87
4.10	y-displacement of mirrors M1 (left) and M2 (right) due to static wind load . . . . .	89
4.11	Eigenfrequency of the first ground mode . . . . .	89
4.12	Types of mode shapes . . . . .	90
4.13	Comparison of the mode shapes . . . . .	91
4.14	MAC, MSF and normalized $ MPF^* $ . . . . .	92
4.15	Comparison of the transfer functions between y-displacement due to wind load . . . . .	93
4.16	Effects of the soil stiffness onto the transfer functions between y-displacement of mirrors M1 (left) respectively M2 (right) due to wind load. . . . .	94
4.17	Effects of the transmitting boundary condition onto the transfer function. . . . .	95
5.1	BeamWarrior models of the three types of VLTI telescopes . . . . .	99
5.2	Amplitude (left) and phase (right) of the electric field distribution in the nominal exit pupil . . . . .	100
5.3	Top-level architecture of the VLTI Integrated Model . . . . .	103
5.4	Sensor (FSU) and controller (OPDC) of the fringe tracking control loop	104
5.5	Schematic drawing of the signal flow for one arm and one band in the Integrated Model. . . . .	106
5.6	Subsystem model of a single interferometer arm (UT) with the main control loops . . . . .	107
5.7	Exact simulation of the modal filtering process . . . . .	109
5.8	Ruilier method for simulating the modal filtering process. . . . .	110
5.9	Contributions of the mirrors M1 M2 M3 of the UT to the PSD errors for piston, tilt, lateral pupil shift and defocus due to wind load. . . . .	112
5.10	Contribution of the four load cases M1, M3, TU and TR of the UT to the low order PSD errors due to wind load. . . . .	113
5.11	Contribution of wind load, seismic excitation and atmospheric turbulence to the low order errors . . . . .	114
5.12	Contribution of wind load, seismic excitation and atmospheric turbulence to the higher wavefront errors showed by mean of astigmatism and coma. . . . .	114

---

5.13	Time-history effect of the Fringe Tracking Control loop and the Fast Tip/Tilt Control loop onto the OPD and the tilt of the wavefront in the exit pupil. . . . .	115
5.14	Disturbance rejection of the Fringe Tracking Control loop and the Fast Tip/Tilt Control loop in the frequency domain. . . . .	115
5.15	Intensity loss and phase shift due to simple phase aberrations. . . . .	121
5.16	Example for the time-history of the VINCI output due to wind load . . . . .	122
5.17	Example for the time-history of the VINCI output due to atmospheric turbulence. . . . .	122

# List of Tables

1.1	Comparison: VLT and OWL . . . . .	9
2.1	Scaling laws for structures. (Typical dimension $L$ , density $\rho$ , Youngs modulus $E$ , velocity $U$ . . . . .	24
2.2	Design specification for the VLT of ESO on Paranal [22] . . . . .	27
3.1	Absolute and relative rms error for the computed PSDs of the OPD between the full state model (exact) and the three reduced models. . . . .	69
4.1	List of parameters used for studying the effects of different soil properties.	87
4.2	Telescope mass, mass of the modelled soil and mass of the soil to be removed due to the telescope foundation for a light soil ( $\rho = 1300kg/m^3$ ) . . . . .	88
4.3	Influence of the soil onto the static stiffness. The values give the relative change (without sign) of displacement with respect to the quasi infinite stiff soil. . . . .	88
4.5	List of eigenfrequency, MAC and MSF for the modes of model <i>Owl-GroundVar1</i> , that are similar to the first telescope mode. . . . .	92
4.4	List of eigenfrequencies (in Hz) for the first 4 modes ( $E = 2000MPa$ , $\rho = 1620kg/m^3$ ). . . . .	93
5.2	Open loop and closed loop rms errors for OPD and tilt computed for a wavelength of $2.2\mu m$ for different exposure times. . . . .	116
5.1	Sensitivity matrix of the rigid body motions of primary mirror M1, secondary mirror M2 and tertiary mirror M3 of the Unit Telescope (UT) of VLT. . . . .	119
5.3	Accuracy of the Ruilier approximation . . . . .	120
5.4	Relative error between exact computation and Ruilier approximation for time simulations. . . . .	120

# Appendix

## A Relationship between time-series, PSDs and RMS-values

The time-series can be converted into Power Spectral Densities (PSDs) and a realization of a possible time-history with a given PSD can be generated using random numbers:

The PSD is the amount of power per unit (density) of frequency (spectral) as a function of the frequency and describes how the power (or variance) of a time series is distributed with frequency. Mathematically, it is defined as the Fourier Transform of the autocorrelation sequence of the time series.

$$PSD = \frac{S_{xx}(f)}{f_s} = \frac{1}{f_s} \sum_{m=-\infty}^{\infty} R_{xx}(m) e^{-2\pi f m / f_s} \quad (\text{A.1})$$

An equivalent definition of PSD is the squared modulus of the Fourier transform of the time series, scaled by a proper constant term.

For continuous signals the autocorrelation is defined as

$$R_{xx}(t) = E(x(t - \tau)x(\tau)) = \langle x(t - \tau)x(\tau) \rangle = \int_{-\infty}^{\infty} x(t - \tau)x(\tau) d\tau. \quad (\text{A.2})$$

For a discrete time series it is given as

$$R_{xx}(m) = E(x_{n+m}x_n), \quad (\text{A.3})$$

where  $E()$  denotes the expected value and can be computed approximately to

$$R_{xx}(m) \approx \sum_{n=0}^{N-M-1} x_{n+m}x_n \text{ for } m \geq 0; \quad R_{xx}(m) = R_{xx}^H(-m) \text{ for } m < 0; \quad (\text{A.4})$$

Using the discrete-time Fourier transformation (sampling frequency  $f_s = L * \Delta f$ )

$$\begin{aligned} X_L(f) &= X_L((k-1)\Delta f) = X_L[k] = \sum_{n=1}^L x_L[n] e^{-2\pi i f(n-1)/f_s} \\ &= \sum_{n=1}^L x_L[n] e^{-2\pi i (k-1)(n-1)/L}, \quad 1 \leq k \leq L \end{aligned} \quad (\text{A.5})$$

and the inverse discrete Fourier transformation

$$\begin{aligned} x_L(t) &= x_L((n-1)\Delta t) = x_L(n) \\ &= \frac{1}{N} \sum_{k=1}^L X_L(k) e^{2\pi i(k-1)(n-1)/L}, \quad 1 \leq n \leq L \end{aligned} \quad (\text{A.6})$$

allows to compute an estimation of the two-sided PSD:

$$P_{xx}(f) = \frac{|X_L(f)|^2}{f_s L} \quad (\text{A.7})$$

(e.g. in Matlab: *periodogram.m*)

The one-sided PSD is given by:

$$P_{xx,one-sided}(f) = \begin{cases} P_{xx}(f) & |f = 0 \\ 2P_{xx}(f) & |f = [f_s : f_s : \frac{N}{2}f_s] \end{cases} \quad (\text{A.8})$$

Applying a window (e.g.: Hanning window, Hamming window, ...) reduces the spectral leakage effects. A modification is Welch's method ([60]), which divides the time series into (possibly overlapping) segments to compute a spectrum for each segment and uses in the end the average spectrum as the PSD estimate.

To generate a realization of a time-series with a given one-sided PSD is possible by inverting the PSD computation. The total time covered by the spectrum is  $T = \frac{1}{\Delta f}$ . Usually a signal with zero mean value is generated and thus  $\text{PSD}[1] = \text{PSD}(f=0)$  is set to 0. The maximum frequency in the spectrum defines the time-spacing according to the Nyquist-Theorem  $\Delta t = 1/f_a = \frac{2}{\Delta f}$ . To change the time-spacing (without changing the frequency content) the spectrum can be artificially be filled up with zeros, call *zero-padding*. The total length  $L$  of the time-signal and of the complex spectrum is two times the length of the one-sided PSD. After generating a random vector *randomVec* (with values between 0 and 1) the complex spectrum can be computed using the random phase vector  $\phi = 2\pi \text{randomVec}$ :

$$X_L(f) = \sqrt{\frac{1}{2} f_s L P_{xx,one-sided}(f)} e^{-i\phi} \quad (\text{A.9})$$

and applying the inverse (discrete) Fourier transformation the time-series is given to:

$$x_L((n-1)\Delta t) = x_L[n] \quad (\text{A.10})$$

To characterize the variation of a signal with a single scalar quantity often the rms-value is used. The total rms-value of a signal  $x(t)$  is

$$rms = \left( \frac{1}{t_e - t_0} \int_{t_0}^{t_e} x^2(t) dt \right)^{\frac{1}{2}} \quad (\text{A.11})$$

or expressed in terms of the PSD

$$rms = \left( \int_0^{f_{max}} P_{xx,one-sided}(f) df \right)^{\frac{1}{2}} . \quad (\text{A.12})$$

Both is numerically computed as a sum over the sampling values.

Including a limited exposure time, the PSD has to be multiplied by a filter function:

$$rms_{\tau} = \left( \int_0^{f_{max}} P_{xx,one-sided}(f) (1 - (\text{sinc}(\tau f))^2) df \right)^{\frac{1}{2}} , \quad (\text{A.13})$$

where the *sinc*-function is defined as

$$\text{sinc}(x) = \begin{cases} \frac{\sin(\pi x)}{\pi x} & |x \neq 0 \\ 1 & |x = 0 \end{cases} \quad (\text{A.14})$$

## B Zernike polynomials used within BeamWarrior

For the Zernike polynomials different definitions are common. Here the definition used within BeamWarrior and the VLTI Integrated Model are listed:

Index	Zernike polynomial $\psi_m$	Name
1	1	Piston
2	$r \cos(\theta)$	Tilt around Y
3	$r \sin(\theta)$	Tilt around X
4	$2r^2 - 1$	Defocus
5	$r^2 \cos(2\theta)$	Astigmatism (Y)
6	$r^2 \sin(2\theta)$	Astigmatism (X)
7	$(3r^2 - 2)r \cos(\theta)$	Coma (Y)
8	$(3r^2 - 2)r \sin(\theta)$	Coma (X)
9	$6r^4 - 6r^2 + 1$	Spherical aberration
10	$r^3 \cos(3\theta)$	
11	$r^3 \sin(3\theta)$	
12	$(4r^2 - 3)r^2 \cos(2\theta)$	
13	$(4r^2 - 3)r^2 \sin(2\theta)$	
14	$(10r^4 - 12r^2 + 3)r \cos(\theta)$	



Index	Zernike polynomial $\psi_m$	Name
15	$(10r^4 - 12r^2 + 3)r \sin(\theta)$	
16	$20r^6 - 30r^4 + 12r^2 - 1$	
17	$r^4 \cos(4\theta)$	
18	$r^4 \sin(4\theta)$	
19	$(5r^2 - 4)r^3 \cos(3\theta)$	
20	$(5r^2 - 4)r^3 \sin(3\theta)$	
21	$(15r^4 - 20r^2 + 6)r^2 \cos(2\theta)$	
22	$(15r^4 - 20r^2 + 6)r^2 \sin(2\theta)$	
23	$(35r^6 - 60r^4 + 30r^2 - 4)r \cos(\theta)$	
24	$(35r^6 - 60r^4 + 30r^2 - 4)r \sin(\theta)$	
25	$70r^8 - 140r^6 + 90r^4 - 20r^2 + 1$	
26	$r^5 \cos(5\theta)$	
27	$r^5 \sin(5\theta)$	
28	$(6r^2 - 5)r^4 \cos(4\theta)$	
29	$(6r^2 - 5)r^4 \sin(4\theta)$	
30	$(21r^4 - 30r^2 + 10)r^3 \cos(3\theta)$	
31	$(21r^4 - 30r^2 + 10)r^3 \sin(3\theta)$	
32	$(56r^6 - 105r^4 + 60r^2 - 10)r^2 \cos(2\theta)$	
33	$(56r^6 - 105r^4 + 60r^2 - 10)r^2 \sin(2\theta)$	
34	$(126r^8 - 280r^6 + 210r^4 - 60r^2 + 5)r \cos(\theta)$	
35	$(126r^8 - 280r^6 + 210r^4 - 60r^2 + 5)r \sin(\theta)$	
36	$252r^{10} - 630r^8 + 560r^6 - 210r^4 + 30r^2 - 1$	
37	$924r^{12} - 2772r^{10} + 3150r^8 - 1680r^6 + 420r^4 - 42r^2 + 1$	

## C Gramians as the solution of the Lyapunov equation and meaning

Gramians are defined with the integral formula in equation (3.54) or equivalently with the Lyapunov equation:

$$\begin{aligned}
\mathbf{W}_C &= \int_0^\infty \underbrace{e^{\mathbf{A}t} \mathbf{B}}_{u'} \underbrace{\mathbf{B}^H e^{\mathbf{A}^H t}}_v dt = \underbrace{[\mathbf{A}^{-1} e^{\mathbf{A}t} \mathbf{B} \mathbf{B}^H e^{\mathbf{A}^H t}]_0^\infty}_{[uv]} - \int_0^\infty \underbrace{\mathbf{A}^{-1} e^{\mathbf{A}t} \mathbf{B} \mathbf{B}^H e^{\mathbf{A}^H t} \mathbf{A}^H}_{uw'} dt \\
\Rightarrow \mathbf{W}_C &= -\mathbf{A}^{-1} \mathbf{B} \mathbf{B}^H - \mathbf{A}^{-1} \underbrace{\int_0^\infty e^{\mathbf{A}t} \mathbf{B} \mathbf{B}^H e^{\mathbf{A}^H t} dt}_{\mathbf{W}_C} \mathbf{A}^H \\
&\Rightarrow \mathbf{A} \mathbf{W}_C + \mathbf{W}_C \mathbf{A}^H + \mathbf{B} \mathbf{B}^H = 0 \\
\text{analog: } &\mathbf{A}^H \mathbf{W}_O + \mathbf{W}_O \mathbf{A} + \mathbf{C}^H \mathbf{C} = 0
\end{aligned} \tag{C.15}$$

Gramians define the least energy input to reach a certain state. Using the relation between state and input for a state-space model

$$\mathbf{x}(t) = e^{\mathbf{A}(t-t_0)} \mathbf{x}_0 + \int_{t_0}^t e^{\mathbf{A}(t-\tau)} \mathbf{B} \mathbf{u}(\tau) d\tau, \tag{C.16}$$

the state  $\mathbf{x}_e = \mathbf{x}(t = t_e)$  can be reached starting at  $\mathbf{x}_0 = \mathbf{x}(t = t_0)$  with a certain input  $\mathbf{u}(t)$  with least required energy  $J = \int_{t_0}^{t_e} \mathbf{u}^H(\tau) \mathbf{u}(\tau) d\tau$ . To compute this  $\mathbf{u}(t)$  an variation problem is solved using the Lagrange function  $\mathbf{L} = \mathbf{J} + \lambda^H (\mathbf{x}_e - e^{\mathbf{A}(t_e-t_0)} \mathbf{x}_0 - \int_{t_0}^{t_e} e^{\mathbf{A}(t_e-\tau)} \mathbf{B} \mathbf{u}(\tau) d\tau)$ :

$$\begin{aligned}
L(\mathbf{u}, \lambda) &= \int_{t_0}^{t_e} \mathbf{u}^H(\tau) \mathbf{u}(\tau) d\tau + \lambda^H \left( \mathbf{x}_e - e^{\mathbf{A}(t_e-t_0)} \mathbf{x}_0 - \int_{t_0}^{t_e} e^{\mathbf{A}(t_e-\tau)} \mathbf{B} \mathbf{u}(\tau) d\tau \right) = \min! \\
\delta L(\mathbf{u}, \lambda) &= 2 \int_{t_0}^{t_e} \mathbf{u}^H(\tau) \delta \mathbf{u} d\tau + \lambda^H \left( - \int_{t_0}^{t_e} e^{\mathbf{A}(t_e-\tau)} \mathbf{B} \delta \mathbf{u} d\tau \right) + \\
&\quad \left( \mathbf{x}_e - e^{\mathbf{A}(t_e-t_0)} \mathbf{x}_0 - \int_{t_0}^{t_e} e^{\mathbf{A}(t_e-\tau)} \mathbf{B} \mathbf{u}(\tau) d\tau \right)^H \delta \lambda \stackrel{!}{=} 0 \\
\mathbf{u}(t) &= \frac{1}{2} \mathbf{B}^H e^{\mathbf{A}^H(t_e-\tau)} \lambda \\
0 &= \mathbf{x}_e - e^{\mathbf{A}(t_e-t_0)} \mathbf{x}_0 - \int_{t_0}^{t_e} e^{\mathbf{A}(t_e-\tau)} \mathbf{B} \frac{1}{2} \mathbf{B}^H e^{\mathbf{A}^H(t_e-\tau)} d\tau \lambda = \mathbf{x}_e - e^{\mathbf{A}(t_e-t_0)} \mathbf{x}_0 - \frac{1}{2} \mathbf{W}_s \lambda \\
\rightarrow \lambda &= 2 \mathbf{W}_s^{-1} (\mathbf{x}_e - e^{\mathbf{A}(t_e-t_0)} \mathbf{x}_0) \\
\rightarrow \mathbf{u}(t) &= \mathbf{B}^H e^{\mathbf{A}^H(t_e-\tau)} \mathbf{W}_s^{-1} (\mathbf{x}_e - e^{\mathbf{A}(t_e-t_0)} \mathbf{x}_0)
\end{aligned} \tag{C.17}$$

Considering now the time from  $t_0 = -\infty$  to  $t_e = 0$ ,  $\mathbf{W}_s$  becomes the controllability Gramian (substituting the variable in the integral  $t = t_e - \tau$ ):

$$\begin{aligned}
\mathbf{W}_s(t_0 = -\infty, t_e = 0) &= \int_{-\infty}^0 e^{\mathbf{A}(t_e-\tau)} \mathbf{B} \mathbf{B}^H e^{\mathbf{A}^H(t_e-\tau)} d\tau \\
&= \int_0^\infty e^{\mathbf{A}t} \mathbf{B} \mathbf{B}^H e^{\mathbf{A}^H t} d\tau = \mathbf{W}_C
\end{aligned} \tag{C.18}$$

Hence, the controllability Gramian is directly connected with the least energy input to reach a certain state  $\mathbf{x}_0$ .

## D Visibility function and brightness distribution

An extended source with center  $\mathbf{s}_0$  is described by the intensity distribution  $F(\Delta\mathbf{s})$  on the sky. The delay lines are adjusted for  $\delta = OPD_{tot}$  for the direction  $\mathbf{s}_0$ ; thus the point in  $\mathbf{s} = \mathbf{s}_0 + \Delta\mathbf{s}$  has an OPD of  $\Delta\mathbf{s} \circ \mathbf{B} + \delta$ . The total power collected from this source can be derived by incoherent superposition of the monochromatic case over the source surface, where  $A(\Delta\mathbf{s})$  is the aperture area and  $F(\Delta\mathbf{s})$  is in units of incident power per area:

$$\begin{aligned} P(\mathbf{s}_0, \mathbf{B}, \delta) &= \int A(\Delta\mathbf{s})F(\Delta\mathbf{s})(1 + \cos(k(\Delta\mathbf{s} \circ \mathbf{B} + \delta)))d\Omega \\ &= \int A(\Delta\mathbf{s})F(\Delta\mathbf{s})d\Omega \\ &\quad + \cos k\delta \int A(\Delta\mathbf{s})F(\Delta\mathbf{s}) \cos k\Delta\mathbf{s} \circ \mathbf{B}d\Omega \\ &\quad - \sin k\delta \int A(\Delta\mathbf{s})F(\Delta\mathbf{s}) \sin k\Delta\mathbf{s} \circ \mathbf{B}d\Omega \end{aligned} \quad (\text{D.19})$$

Introducing the constant aperture-integrated power  $P_0 = \int A(\Delta\mathbf{s})F(\Delta\mathbf{s})d\Omega$  and the complex visibility function  $V(k, B)$  for the brightness distribution  $F$  dependent on the wave number  $k$  and the baseline vector  $\mathbf{B}$ :

$$V(k, \mathbf{B}) = \int A(\Delta\mathbf{s})F(\Delta\mathbf{s})e^{ik\mathbf{s} \circ \mathbf{B}} d\Omega, \quad (\text{D.20})$$

allows to write the detected power as

$$P(\mathbf{s}_0, \mathbf{B}, \delta) = P_0 + \Re(V) \cos k\delta + \Im(V) \sin k\delta = P_0 + \Re(Ve^{ik\delta}) \quad (\text{D.21})$$

Writing  $\mathbf{s} \circ \mathbf{B} = \alpha B_x + \beta B_y$  in suitable coordinates  $(x, y)$  and  $(\alpha, \beta)$  and introducing the spatial frequencies  $u = B_x/\lambda = B_x k/2\pi$  and  $v = B_y k/2\pi$  gives  $V$  as a two-dimensional Fourier-transformation:

$$V(u, v) = \int \int A(\alpha, \beta)F(\alpha, \beta)e^{-2\pi i(\alpha u + \beta v)} d\alpha d\beta \quad (\text{D.22})$$

and due to the invertibility of the Fourier-transformation:

$$F(\alpha, \beta) = \left( \int \int V(u, v)e^{2\pi i(\alpha u + \beta v)} dudv \right) / A(\alpha, \beta) \quad (\text{D.23})$$

Therefore, to reconstruct an extended source requires the measurement of  $V(u, v)$ , i.e. a variation of the baseline in both the absolute aperture distance and the direction with respect to the source.

## E Rigid body motions and coordinate transformations

The position of the point P on the undeformed structure is:

$$\mathbf{r}_{OP} = \mathbf{r}_{OV} + \mathbf{r}_{VP} \quad (\text{E.24})$$

After the translation of the vertex V by  $\mathbf{r}_{VV'}$  and rotation by  $\theta$  the position of P is ( $P \rightarrow P'$ ):

$$\mathbf{r}_{OP'} = \mathbf{r}_{OV} + \mathbf{r}_{VV'} + \mathbf{r}_{V'P'} \quad (\text{E.25})$$

Using the I-system as a reference the equation become:

$${}_I\mathbf{r}_{OP'} = {}_I\mathbf{r}_{OV} + {}_I\mathbf{r}_{VV'} + {}_I\mathbf{r}_{V'P'} = {}_I\mathbf{r}_{OV} + {}_I\mathbf{r}_{VV'} + A_{IM} {}_M\mathbf{r}_{V'P'} \quad (\text{E.26})$$

with  $A_{IM}$  being the transformation matrix from system M to system I.

For small rotations  $\theta$ , the term  $A_{IM} {}_M\mathbf{r}_{V'P'}$  can be simplified:

The complete rotation is done in three steps: Firstly by  $\alpha$  along the  $x$ -axis ( $I \curvearrowright K' : (x_I, y_I, z_I) \curvearrowright (x', y', z')$ ). Secondly by  $\beta$  along the new  $y'$ -axis ( $K' \curvearrowright K'' : (x', y', z') \curvearrowright (x'', y'', z'')$ ). Finally by  $\gamma$  along the new  $z''$ -axis ( $K'' \curvearrowright K : (x'', y'', z'') \curvearrowright (x_K, y_K, z_K)$ ). The individual transformation matrices read:

$$A_{IK'} = \begin{pmatrix} 1 & 0 & 0 \\ 0 & \cos(\alpha) & -\sin(\alpha) \\ 0 & \sin(\alpha) & \cos(\alpha) \end{pmatrix}$$

$$A_{K'K''} = \begin{pmatrix} \cos(\alpha) & 0 & \sin(\alpha) \\ 0 & 1 & 0 \\ -\sin(\alpha) & 0 & \cos(\alpha) \end{pmatrix}$$

$$A_{K''K} = \begin{pmatrix} \cos(\alpha) & -\sin(\alpha) & 0 \\ \sin(\alpha) & \cos(\alpha) & 0 \\ 0 & 0 & 1 \end{pmatrix}$$

The complete transformation from the K-system back to the I-system is:

$$A_{IK} = \begin{pmatrix} \cos(\gamma) \cos(\beta) & -\sin(\gamma) \cos(\beta) & \cos(\beta) \\ \sin(\alpha) \sin(\beta) \cos(\gamma) + \sin(\gamma) \cos(\alpha) & -\sin(\gamma) \sin(\beta) \sin(\alpha) + \cos(\gamma) \cos(\alpha) & -\cos(\beta) \sin(\alpha) \\ -\cos(\alpha) \sin(\beta) \cos(\gamma) + \sin(\gamma) \sin(\alpha) & \sin(\gamma) \sin(\beta) \cos(\alpha) + \cos(\gamma) \sin(\alpha) & \cos(\beta) \cos(\alpha) \end{pmatrix}$$

$$A_{IM} {}_M\mathbf{r}_{V'P'} \approx {}_I\mathbf{r}_{VP} + \theta \times {}_I\mathbf{r}_{VP} = {}_I\mathbf{r}_{VP} - {}_I\mathbf{r}_{VP} \times \theta \quad (\text{E.27})$$

The displacement of point P is herewith and with E.24

$$\begin{aligned} {}_I\mathbf{r}_{PP'} &= {}_I\mathbf{r}_{OP'} - {}_I\mathbf{r}_{OP} \\ &= {}_I\mathbf{r}_{OV} + {}_I\mathbf{r}_{VV'} + {}_I\mathbf{r}_{VP} - {}_I\mathbf{r}_{VP} \times \theta - {}_I\mathbf{r}_{OV} - {}_I\mathbf{r}_{VP} \end{aligned} \quad (\text{E.28})$$

and so the final equation

$${}_I \mathbf{r}_{PP'} = {}_I \mathbf{r}_{VV'} - {}_I \mathbf{r}_{VP} \times \theta \quad (\text{E.29})$$



## **Dank**

Die vorliegende Dissertation entstand während meiner Tätigkeit als wissenschaftlicher Assistent am Lehrstuhl für Leichtbau der Technischen Universität München in enger Zusammenarbeit mit dem European Southern Observatory.

Beim Leiter des Lehrstuhls für Leichtbau Prof. Dr.-Ing. Horst Baier möchte ich mich bedanken für die Betreuung und die Ermöglichung meiner Arbeit in einem so interessanten und faszinierenden Forschungsbereich.

Ein besonderer Dank gilt der freundlichen und hilfsbereiten Unterstützung durch Herrn Dr. Bertrand Koehler und Herrn Franz Koch von ESO, durch deren Simulationsdaten und Modelle meine Arbeit erst ermöglicht wurde. Die engste Zusammenarbeit hatte ich mit Herrn Dr. Rainer Wilhelm, der mir sehr vieles erklärt hat und durch Ideen meine Arbeit geprägt hat. Für das freundschaftliche Verhältnis und die kritische Durchsicht meines Manuskriptes möchte ich herzlich danken.

Dank gilt auch allen Kollegen am Lehrstuhl für Leichtbau, aber insbesondere Herrn Jesko Klammer, mit dem ich während der Jahre ein Zimmer geteilt habe, und Herrn Harald Langer, der mir in Diskussionen geholfen hat, Probleme zu analysieren.

Schliesslich möchte ich mich besonders bei meiner Verlobten Anita Kopp bedanken, die mein Leben während der Zeit am Lehrstuhl für Leichtbau begleitet und geprägt hat.

